SINTERED BENTONITE CERAMICS FOR THE IMMOBILIZATION OF CESIUM- AND STRONTIUM-BEARING RADIOACTIVE WASTE

A Dissertation

by

LUIS HUMBERTO ORTEGA

Submitted to the Office of Graduate Studies of
Texas A&M University
in partial fulfillment of the requirements for the degree of

DOCTOR OF PHILOSOPHY

December 2009

Major Subject: Materials Science and Engineering

SINTERED BENTONITE CERAMICS FOR THE IMMOBILIZATION OF CESIUM- AND STRONTIUM-BEARING RADIOACTIVE WASTE

A Dissertation

by

LUIS HUMBERTO ORTEGA

Submitted to the Office of Graduate Studies of
Texas A&M University
in partial fulfillment of the requirements for the degree of

DOCTOR OF PHILOSOPHY

Approved by:

Chair of Committee,	Sean M. McDeavitt
Committee Members,	Bill Batchelor
	Michael D. Kaminski
	Lin Shao
	Karen Vierow
Intercollegiate Faculty Chair,	Tahir Cagin

December 2009

Major Subject: Materials Science and Engineering

ABSTRACT

Sintered Bentonite Ceramics for the Immobilization of Cesium- and
Strontium-bearing Radioactive Waste. (December 2009)
Luis Humberto Ortega, B.S., New Mexico State University;
M.S., Purdue University
Chair of Advisory Committee: Dr. Sean M. McDeavitt

The Advanced Fuel Cycle Initiative (AFCI) is a Department of Energy (DOE) program, that has been investigating technologies to improve fuel cycle sustainability and proliferation resistance. One of the program's goals is to reduce the amount of radioactive waste requiring repository disposal.

Cesium and strontium are two primary heat sources during the first 300 years of spent nuclear fuel's decay, specifically isotopes Cs-137 and Sr-90. Removal of these isotopes from spent nuclear fuel will reduce the activity of the bulk spent fuel, reducing the heat given off by the waste. Once the cesium and strontium are separated from the bulk of the spent nuclear fuel, the isotopes must be immobilized.

This study is focused on a method to immobilize a cesium- and strontium-bearing radioactive liquid waste stream. While there are various schemes to remove these isotopes from spent fuel, this study has focused on a nitric acid based liquid waste. The waste liquid was mixed with the bentonite, dried then sintered. To be effective sintering temperatures from 1100 to 1200°C were required, and waste concentrations must be at least 25 wt%. The product is a leach resistant ceramic solid with the waste elements embedded within alumino-silicates and a silicon rich phase. The cesium is primarily incorporated into pollucite and the strontium into a monoclinic feldspar.

The simulated waste was prepared from nitrate salts of stable ions. These ions were limited to cesium, strontium, barium and rubidium. Barium and rubidium will be co-extracted during separation due to similar chemical properties to cesium and strontium. The waste liquid was added to the bentonite clay incrementally with drying steps between each addition. The dry powder was pressed and then sintered at various temperatures. The maximum loading tested is 32 wt. percent waste, which refers to 13.9 wt. percent cesium, 12.2 wt. percent barium, 4.1 wt. percent strontium, and 2.0 wt. percent rubidium. Lower loadings of waste were also tested. The final solid product was a hard dense ceramic with a density that varied from 2.12 g/cm^3 for a 19% waste loading with a 1200°C sintering temperature to 3.03 g/cm^3 with a 29% waste loading and sintered at 1100°C.

Differential Scanning Calorimetry and Thermal Gravimetric Analysis (DSC-TGA) of the loaded bentonite displayed mass loss steps which were consistent with water losses in pure bentonite. Water losses were complete after dehydroxylation at ~650°C. No mass losses were evident beyond the dehydroxylation. The ceramic melts at temperatures greater than 1300°C.

Light flash analysis found heat capacities of the ceramic to be comparable to those of strontium and barium feldspars as well as pollucite. Thermal conductivity improved with higher sintering temperatures, attributed to lower porosity. Porosity was minimized in 1200°C sinterings. Ceramics with waste loadings less than 25 wt% displayed slump, the lowest waste loading, 15 wt% bloated at a 1200°C sintering. Waste loading above 25 wt% produced smooth uniform ceramics when sintered >1100°C.

Sintered bentonite may provide a simple alternative to vitrification and other engineered radioactive waste-forms.

I am very fortunate to have a loving family and friends who gave their unwavering support, my sister and her husband Mary Helen and Terry Ormseth, my mother and father Maria Elena and James Resley, and my uncle Guillermo Ortega; my close friends Andy Walter, Red Knaak, Frank Williams, Matt Murawski, Flint Taylor, Michael Robbins, Mike Aussem, Sarah Harcum, Barry Goode, Matt Hartman, Rob Cruz, Edith Cassell and Karie Badgley. I would also like to thank God for everything.

ACKNOWLEDGMENTS

I would like to thank my adviser, Sean McDeavitt, for his patience and support throughout this process. Without his experience and suggestions, this would have not been possible. I would also like to thank my committee for their time and attention to detail, Bill Batchelor, Karen Vierow, Lin Shao and especially Michael Kaminski whose guidance has been immeasurable.

I thank the researchers whose individual expertise helped collect the data before you: Ray Guillemette for his work with the electron microprobe, Latha Vasudevan for neutron activation analysis, Nattamai Bhuvanesh for x-ray powder diffraction, Yefen Tsai and Robert Taylor for inductively coupled plasma mass spectroscopy.

For their assistance in the lab I would like to thank Carol Mertz for her help finding materials and equipment, Grant Helmreich for running the light flash analyzer, Julie Borgmeyer for her help with the toxicity leach procedure and assisting Dr. Guillemette, and Daren Malik and Jeff Hausaman for their help with the differential scanning calorimeter.

I would like to thank Kevin Hogan for his help making the data presentable. I would like to thank Aaron Totemeier for his LaTeX work as well as his friendship and overall support in this entire process. This work required the assistance of dozens of other people to complete, I am grateful to all of them.

This work has been funded by the Advanced Fuel Cycle Initiative (AFCI) and the Nuclear Energy Research Initiative (NERI) Award No. DE-FC07-06ID14737 Project No. 06-058, under the United States Department of Energy Office of Nuclear Energy.

NOMENCLATURE

AFCI	Advanced Fuel Cycle Initiative
BSE	Backscattered Electron Image
CTE	Coefficient of Thermal Expansion
DOE	Department of Energy
DSC	Differential Scanning Calorimetry
EDS	Energy Dispersive Spectroscopy
FPEX	Fission Product Extraction Process
ICP-MS	Inductively Coupled Plasma Mass Spectroscopy
LFA	Light Flash Analysis
NAA	Neutron Activation Analysis
NERI	Nuclear Energy Research Initiative
SEM	Scanning Electron Microscopy
TCLP	Toxicity Characteristic Leach Procedure
UREX	uranium extraction process
WDS	Wave Dispersive Spectroscopy
XRD	X-Ray Powder Diffraction

TABLE OF CONTENTS

Page

Page

LIST OF TABLES

LIST OF FIGURES

FIGURE Page

FIGURE Page

1. INTRODUCTION

The United States' long term strategy for the fate of commercial spent nuclear fuel is undetermined. Currently most spent fuel remains at the site where the power was generated. A repository has been started in Nevada's Yucca Mountain but legislative issues have left the entire project in question. When this study was initiated the problems associated opening Yucca Mountain were already evident. The prospect of exhausting the space to store spent fuel, leading to a second repository motivated the search for methods to limit waste volume. The DOE's Advanced Fuel Cycle Initiative was investigating methods to reuse isotopes with energy content, transmute long-lived nuclides into isotopes with shorter half-lives, and find ways to reduce volume as well [1]. the waste packing is limited by the heat generated by the radioactive decay. If the total heat load can be reduced, space can be saved. The removal of cesium and strontium could reduce repository size to <20% of current estimates [2]. The cesium and strontium will require immobilization once separated from the bulk of the spent nuclear fuel.

Once removed the cesium and strontium require treatment. The focus of this work investigates the immobilization of this potential waste stream with sintered clays. In addition to the cesium and strontium, barium and rubidium are also in the waste stream due to similar chemical properties. A simulated waste stream was prepared by dissolving nitrate salts of each metal in a dilute nitric acid solution. Our simulated waste solution was mixed with the natural mineral bentonite, a smectite clay. Bentonite clay consists primarily of montmorillonite with small amounts of quartz. Montmorillonite has a layered aluminosilicate structure composed of alternating sheets of alumina and silica. An alumina octahedral sheet resides between two silica tetrahedral sheets. Between these repeating silica-alumina-silica layers are metal cations

This dissertation follows the style of *International Journal of Heat and Mass Transfer.*

water, and within the silica and alumina there are hydroxyl groups (Figure 1.1). A typical formula unit may be as follows: $(Na,Ca)_{0.33}(Al,Mg)_2(Si_4O_{10})(OH)_2nH_2O$ where the cation species and concentrations vary from source to source.

The clay was loaded with waste ions in concentrations ranging from approximately 16 mass percent to 32 mass percent total waste ions. The theoretical maximum was based on the mineral pollucite $(Cs,Na)_2Al_2Si_4O_{12}(H_2O)$. Pollucite is an aluminosilicate with the same alumina-to-silica ratio as montmorillonite, and cesium constitutes ~30 mass percent or ~32 mass percent when sodium is replaced by cesium. In this document clay loadings are occasionally referred to as a percentage of the theoretical maximum, where 100% refers to a target of 30 mass percent waste ions. The liquid simulated waste was added to the clay to the desired concentration, then the liquid waste-clay slurry was dried to a powder. The powder was then pressed into a pellet and sintered. Sintering temperatures were varied from 700 to 1400 °C, while the waste concentrations varied from approximately 50% to 100% of the theoretical maximum.

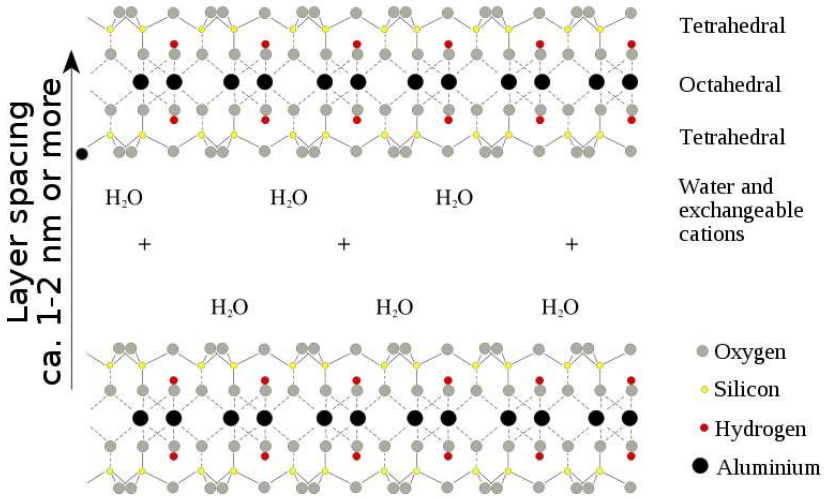

Fig. 1.1. Montmorillonite clay structure.

1.1 Objective

The potential waste stream from the FPEX process is a highly radioactive acidic liquid. How to stabilize this liquid is a problem that can be solved in various ways. The considerations required to make an efficient and economical solution are several. The primary criteria is the immobilization of the ions. These metals must be bound tightly in the final matrix due to their radiotoxicity as well as their chemical hazards; *i.e.* water soluble barium compounds are poisonous. The resulting matrix may be exposed to moisture which may be acidic or alkaline. The radioactivity creates multiple problems. The heat given off during the decay process, if great enough, can melt the material if the geometry and loading are not carefully thought out. The radiation can damage the structure as well, which can impact the properties of the waste form. The isotopes themselves change chemically as they undergo decay. Other considerations are economic, logistic, as well as processing safety. High temperatures require energy that comes at cost, similarly with processes requiring high pressures. Processes with intermediate steps, especially those involving powders create safety issues. The simpler the process the more economical. Each step with a highly radioactive material requires automation; fewer steps reduce cost considerably.

An ideal waste form will be mechanically and chemically stable, will withstand radiation damage, be dense and sufficiently thermally conductive. Processing should have minimal steps, and if there are powders involved they should be continuously consolidated to avoid a large holdup of an easily dispersible hazardous substance. Although daunting, these issues are manageable.

Due to the nature of this waste solution, containing only the alkali metals and alkaline earth metals, the reactants can be chosen to target a specific outcome. Using natural aluminosilicate minerals as examples of stable compounds, we chose these forms as prospective hosts for the waste ions. Bentonite clay primarily consists of silica and alumina, and for this reason bentonite clay was chosen as a reactant. The silica and alumina become the building blocks for the objective minerals.

Alumino-silicates have been produced from clay before. Sorrell found strontium, barium and lead sulfates could be heated with kaolin clays to produce feldspars [3]. Spitsyn looked at roasting bentonite specifically for the immobilization of strontium [4]. Investigations by Strachan and Shultz done on pollucite, a cesium bearing alumino-silicate, for radioactive waste storage found good leach rates, low solubility and thermal stability. They conceded uncertainties in pollucite's radiation stability and transmutation effects [5]. They proposed the use of pollucite for cesium-137 immobilization derived from CsCl, or $CsCO_3$ reacted with montmorillonite at 970 K [6]. Vance used high pressures and temperatures to convert a sol to pollucite for use as a Cs-137 immobilization matrix also [7]. Cs-137 doped pollucite was synthesized from a colloidal silica solution with stoichiometric amounts of cesium and aluminum nitrates, which were stirred and dried, then calcined at 793–813 K, followed by grinding, and compaction at 250 Pa, and finally sintering. The pollucite was observed for β^- radiation effects on the long-range and local structure [8]. The study was not able to observe the γ effects due to small sample size but found swelling and distortion of the lattice. Cs-137 is transformed by β^- decay into Ba-137:

$$Cs^{+} \xrightarrow{\beta^-} Ba^{2+}$$

The resulting Ba-137^m is meta-stable and will quickly transform($T_{1/2}$= 2.6 min) to a stable configuration by giving off a 662 keV gamma-ray. Cs-137, Cs-135, and Cs-133 will not be separated during reprocessing due to their near identical chemical behavior. Cs-135 gives off a 0.21 MeV β^- which decays to Ba-135 with $T_{1/2}= 2.3 \times 10^6$ years, and Cs-133 is stable.

Sr-90 is a pure beta emitter, with a half life of 28.8 years. Sr-90 decays with a 0.546 MeV β^- yielding an Y-90 atom, which also β^- decays with a half life of 64 hours, giving off a 2.28 MeV β^- leaving a stable Zr-90 atom. Thus:

$$Sr^{+2} \xrightarrow{\beta^-} Y^{+3} \xrightarrow{\beta^-} Zr^{+4}$$

The goal of the present study is to produce mineral compounds embedded with ions of cesium, strontium, barium and rubidium. Concentration of the total waste will be varied, but the ratios of individual ions will be kept the same. Sintering temperatures will be varied from 700 to 1400 °C. These products will be characterized and a preliminary assessment of their properties will then be made. This baseline study can lead to further research into their potential as radioactive waste forms.

2. BACKGROUND AND MOTIVATION

The fate of used nuclear fuel in the United States is uncertain due to the current status of the proposed geological repository at Yucca Mountain Nevada [9]. At the time this thesis was written, the Yucca Mountain project has been effectivly stalled with expectation that project will be cancelled soon. There have been many proposed methods to sequester used nuclear fuel. Deep geologic burial in basalt, salt, and tuff have all been extensively investigated. Due to the difficulty in approval of a geologic site, dry storage in casks with or without a retrievable option are currently being investigated as well. An option that has potential to recycle isotopes with energy content as well as reduce the amount high level radioactive waste is reprocessing.

The Department of Energy (DOE) has been funding the Advanced Fuel Cycle Initiative, and various researchers are currently investigating methods to treat spent nuclear fuel in a sustainable manner [1]. The policy in the USA had been to take entire fuel bundles after sufficient cooling and ship them to Yucca Mountain in Nevada for deep geologic burial. The repository is not yet open, and the future of the project is uncertain. If the United States continues to produce nuclear power and it builds new nuclear power plants, a fuel cycle with separation, transmutation and recycle is an alternative worthy of analysis. An advanced fuel cycle will reduce waste volume and transmute long lived isotopes to ones with shorter half lives, as well as provide burnable fuel for future power generation.

2.1 Advanced Fuel Cycle Initiative

Chemical separations are the foundation of reprocessing, and the extent and exact methods to be used to accomplish these separations are currently under investigation. To begin, the ultimate fate of each isotope or group of isotopes with similar properties must be determined.

Nuclear fuel at 33,000 MWD/MT and 10 years of cooling contains ~95.6 mass% depleted uranium. The next largest fraction consists of stable isotopes and the short-lived fission products at ~3.3 mass%. Once these are separated they are not a radiation hazard but may still be chemically toxic. The next fraction includes plutonium and the long-lived fission products at ~0.95 mass%. These can be incorporated into new mixed oxide fuel or transmuted to isotopes with shorter half-lives. Minor actinides and other long-lived fission products ~0.15 mass% can also be transmuted. Each of these portions of spent fuel can be treated separately. The end result is less volume for high-level waste disposal, shorter half-lives after transmutation, and recycled energy producing fuel [10]. Of the long-lived isotopes, some will not be suitable for transmutation due to half-lives that are not long enough to justify the process. Two primary examples are ^{137}Cs and ^{90}Sr at approximately 30 years [2].

The radioactivity of the high level waste is of primary concern during repository design. The activity of the waste will determine the heat generation and resulting temperature. Water exists as moisture in the soil. In a cold repository design temperature limits are set to keep water flowing through the repository, preventing a hold up of water above the repository from flooding the repository as it cools [11]. Lowering the overall activity will allow more waste into the repository without exceeding these temperature limits.

To maintain low temperatures inside the repository, active cooling with fans has been proposed [11]. Eventually the fans will be turned off after the decay heat decreases to a level where the active cooling is no longer necessary. The removal of cesium and strontium will make a substantial reduction in the activity during the initial years of operation.

The AFCI aqueous reprocessing methods being developed for the UREX+ family of separation processes separate used nuclear fuel into different waste streams [12]. These streams are then treated according to the nature of the particular isotopes they contain. A general overview of the AFCI is shown in Figure 2.1. The three primary

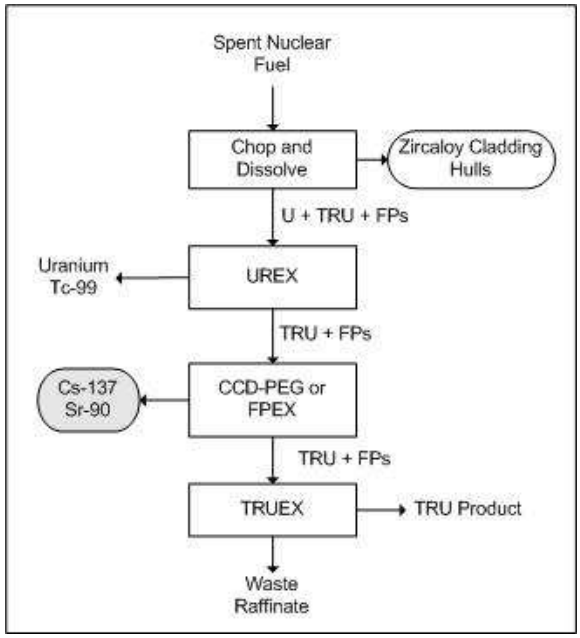

Fig. 2.1. Advanced Fuel Cycle Initiative

steps, Uranium Extraction (UREX), Chlorinated Cobalt Dicarbollide/Polyethylene glycol (CCD-PEG) or FPEX, and Transuranic Extraction (TRUEX) are briefly outlined below.

In the UREX process, high purity uranium and technetium are recovered in three steps. In the first step uranium and technetium are extracted with a 30 vol% tributyl phosphate in n-dodecane solvent. In the next step technetium is extracted from the loaded solvent. The third step strips the uranium from the technectium strip solvent [13]. The remaining transuranics and fission products then go on to either the CCD-PEG or FPEX processes.

2.2 Cesium and Strontium Separation

The FPEX (Fission Product Extraction) process has been developed specifically for the removal of cesium and strontium from the UREX process. There are several

cesium and strontium fission products in spent fuel (Table 2.1) which will also be extractd with the Cs^{137} and the Sr^{90}, along with barium and rubidium. The solvent proposed to remove strontium is 4',4',(5')-di-(t-butyldicyclo-hexano)-18-crown-6, and to remove cesium calix[4]arene-bis-(tert-octylbenzo-crown-6) is proposed. Once the elements are in the solvent the solvent will be washed with dilute nitric acid. The dilute nitric acid with dissolved cesium and strontium will require subsequent treatment [14]. Another method to remove cesium and strontium from the UREX raffinate, is called the CCD/PEG (chlorinated cobalt dicarbollide/polyethylene glycol) process, where the CCD is employed for the removal of cesium, and PEG for strontium [15]. For further separation techniques involving cesium and strontium see [16]. Once the elements are in the solvent, the solution will be washed with guanidine carbonate/ diethylenetriamine pentaacetic acid (DTPA). This process creates a highly radioactive liquid waste. Transportation requirements and repository facility restrictions will only accept solid forms. Therefore at the minimum the solvents must be dried. Once dried the result may be a powder or reactive metals, both requiring additional treatment or specialized containers for transport.

An ideal waste form for these waste streams will be durable as well as chemically inert while resistant to radiation effects. Transmutation during radioactive decay transforms cesium with a $^{+}1$ oxidation state to barium at $^{+}2$. Strontium decays from an oxidation state of $^{+}2$ to zirconium at $^{+}4$. These chemical changes will alter the waste composition by changing the bonding symmetry due to different ionic radii, and ionic charge.

Table 2.1
Cesium and strontium fission products [17]

		In discharge fuel 10^6 Ci/yr	
Radionuclide	$T_{1/2}$	150-day decay	10-yr decay
^{134}Cs	2.046 yr	5.83	0.228
^{135}Cs	3.0×10^6 yr	7.79×10^{-6}	7.79×10^{-6}
^{136}Cs	13.7 days	5.42×10^{-4}	0
^{137}Cs	30.0 yr	2.92	2.33
^{89}Sr	52.7 days	2.65	0
^{90}Sr	27.7 yr	2.09	1.65

Uranium-fueled 1000-MWe PWR, 3-year fuel life.

3. RADIOACTIVE WASTE MANAGEMENT

The following is review of nuclear waste technologies in use and under development. Sintered bentonite will produce a alumino-silicate ceramic, therefore alumino-silicate waste forms will be covered first, and in more detail.

3.1 Alumino-Silicates

Bentonite has been proposed as a waste immobilization matrix as early as 1953 [18]; Hatch cited several of bentonite's benefits, such as cation exchange capacity (~1 meq per gram of clay), and a structure that, when sintered to 1000 °C, becomes inert and no longer able to exchange cations. Other characteristics are the stability of the material, its abundance, its ability to be formed into any desired shape and withstand high temperatures. Barney reported the use of several clays for radioactive waste immobilization by hydrothermal reactions at mild temperatures (up to 100 °C) [19]. Surrounding waste canisters with bentonite to retard the migration of radionuclides in the groundwater was proposed more recently [20, 21]. A novel use for bentonite was proposed by Papachristodoulou *et al* in the decontamination of ruminants [22].

While effective as a generic radioactive waste immobilization matrix, bentonite appears ideally suited for wastes containing alkali and alkaline earth metals when combined with sintering. The bentonite contains the necessary molecular building blocks for pollucite, as well as strontium feldspar. Rubidium and barium both have very similar chemistry to their chemical group counterparts, cesium and strontium respectively and so will have similar reaction products forming rubidium substituted pollucite and barium feldspars.

Natural pollucite and these feldspars survive over geologic time scales, as strontium feldspars are used as geologic chronometers [23]. For this reason synthetic analogs of these aluminosilicate minerals have been studied extensively for radioactive waste treatment. A few methods to produce pollucite include hydrothermal

synthesis [24], using an arc melter [25], high temperature treament of high alumina containing cement mixed with silica fume [26], heating of electrorefiner salt with glass frit to produce a high cesium content glass bonded ceramic [27], and from sintering expanded natural perlite [28]. Konovalov and others used high temperature synthesis, where a highly exothermic metal-to-oxide transformation fuels the mineral synthesis. These reactions are Fe_2O_3 + Al to incorporate cesium into pollucite, and Ti + MoO_3 for strontium into sphene ($CaTiSiO_5$) [29]. Pereira synthesized pollucite from CsCl and chabazite by melting at 700°C for waste chloride immobilization [30].

Vasil'eva *et al* were able to produce both pollucite and strontium feldspar products via solid state crystallization at 700-900 °C of coal fly ash cenospheres [31], as well as Mimura and Akiba by calcination of Cs-mordenite Sr-zeolite [32], Bogdanova and others achieved the similar products with zeolite containing rocks [33]. Zimmer and others treated a complex waste simulant with numerous chemical species with a sol-gel technique where pollucite, as well as barium and strontium feldspars were in the final matrix [34]. Each of these has similarities to this study, the use of alumino silicates to immobilize cesium and strontium, but none incorporated a FPEX waste solution, neither did they use bentonite specifically. This study simulated an acidic waste solution with barium and rubidium as well as the cesium and strontium. Only one of the previous studies had these species incorporated in their waste, but all were in low levels in conjunction with several other elements [34]. The addition of the wastes to the immobilizing matrix in these aforementioned studies is of greatest difference to our study, most employed contacting the solutions with the absorbing zeolite, whereas the solutions examined here were dried off the waste solution with heat. The reason this was done, was to mimic a process close to an engineering solution. Heating the clay waste solution in this way, the effect of a highly concentrated acid has on the bentonite during processing can be observed, as well as an opportunity to document any gross volitization of cesium that may be occurring during the boiling off of the water. When contacting the absorber with the waste

solution the loading is limited to the cation exchange capacity of the particular zeolite, cenosphere etc. The greatest benefit to drying the solution onto the bentonite, is that the loading concentration is not limited by the cation exchange capacity. Our limit will have to be determined by experiment to determine at what concentration leachability becomes unacceptably high.

The work mentioned above and throughout this document, which has focused on pollucite for Cs-137 immobilization has been motivated by the low leachability of pollucite. Pollucite has been shown to have leach rates from 3×10^{-4} to 2.2×10^{-6} $g/m^2 \cdot d$ [35]. Anchell found the low leach rates were due to self diffusion rates to be ~0 [36]. Anchell noted findings by Barrer and Rees which showed that when pollucite (Cs-analcite) is finely crushed and dispersed in a NaCl solution the cation exchange rate is 1.74×10^{-17} cm^2/sec (at 25°C self diffusion of Na^+ in glass is 10^{-17} cm^2/sec) [37]. Although low, he recommended minimizing the surface area of these waste forms to counter this issue. Hess found β^- damage to stoichiometric ^{137}Cs doped pollucite structure slightly increased the volume from 0.5 - 1 % [8]. A study performed by Argonne and Pacific Northwest National Labs interrogated ^{137}Cs pollucite sources for transmutation effects on the pollucite structure [38]. They found minimal damage even in a sample that had decayed 20 years, corresponding to a decay of 16% of the ^{137}Cs transmuting to ^{137}Ba. However the initial ^{137}Cs mass fraction was 0.0375 which is relatively low.

The thermodynamic properties of pollucite and the feldspars of strontium and barium will aid understanding reaction rates, such as the minerals with lower heats of formation may form quickly. Heat capacities are necessary for thermal conductivity determination of the final waste form. The known heat capacities of the minerals will be compared the sintered bentonite heat capacity. Thermodynamic properties of pollucite and the feldspars of Sr and Ba were calculated by two methods. Natural pollucite data was calculated by Ogorodova and others [39], the feldspars were synthesized by Chernyshova and his colleagues [40]. The heat capacities cited here

were plotted on a mass basis along with our results for comparison (Figures 5.9, 5.10, 5.11) Heats of formation and Gibb's free energies are listed in Table 3.1. Heat capacity for the natural pollucite:

$Cs_{0.84}Na_{0.11}Al_{0.88}Si_{2.10}O_6{\cdot}0.17H_2O$

$$C^{\circ}_{p,m} = 131.37 + 181.97 \times 10^{-3}T - 11.84 \times 10^{5}T^{-2}JK^{-1}mol^{-1}(\pm 0.36\%) \tag{3.1}$$

at 298.15610K [39].

Heat capacity for the sythetic Sr and Ba feldspars:

$SrAl_2Si_2O_8$

$$C_p = 269.59 + 5.784 \times 10^{-2}T - 5.833 \times 10^{6}T^{-2}JK^{-1}mol^{-1} \tag{3.2}$$

at 250-1000K [40].

$BaAl_2Si_2O_8$

$$C_p = 261.05 + 6.640 \times 10^{-2}T - 5.2568 \times 10^{6}T^{-2}JK^{-1}mol^{-1} \tag{3.3}$$

at 250-1000K [40].

Table 3.1

Thermodynamic properties of natural pollucite, and synthetic Sr-feldspar, and Ba-feldspar at T = 298.15 K

Mineral	$-\Delta_f H^{\circ}_m$ (kJ mol^{-1})	$-\Delta_f G^{\circ}_m$ (kJ mol^{-1})	Reference
Pollucite I$^{\clubsuit}$	3104 ± 13	2921	[39]
Pollucite II$^{\heartsuit}$	3090 ± 14	2911	[39]
Sr-Feldspar ($SrAl_2Si_2O_8$)	4248	4023.75	[40]
Ba-Feldspar ($BaAl_2Si_2O_8$)	4244.30	4021.87	[40]

$^{\clubsuit}Cs_{0.77}Na_{0.14}Rb_{0.04}Al_{0.91}Si_{2.08}O_6{\cdot}0.34H_2O$ (molar mass = 294.15 × 10^{-3} kg mol^{-1})

$^{\heartsuit}Cs_{0.84}Na_{0.11}Al_{0.88}Si_{2.10}O_6{\cdot}0.17H_2O$ (molar mass = 295.88 × 10^{-3} kg mol^{-1})

These minerals display low Coefficients of Thermal Expansion (CTE). Yanse reported the thermal expansion coefficient for pollucite $1.3 \times 10^{-6}/°C$ (23-1000 °C) [41]. Barbeeri reported the CTE for Ba-feldspar to be $2.29 \times 10^{-6}/°C$ from 20-1000°C (CTE for borosilicate glass 0.75×10^{-4} 300-500°C [42]) , and melting points of 1760 and 1650°C for Ba-feldspar and Sr-feldspar, respectively. Beall found that the barium and strontium feldspars are thermally stable above 1400°C with a melting point just below 1700°C. He also determined that these feldspars could have their coefficients of thermal expansion adjusted by 30-50 $\times 10^{-7}/°C$ with the addition of accessory phases: for example The CTE could be lowered by the addition silica glass [43]. Adding glass requires heating to the liquidous temperature, which for borosilicate glass is 1050°C [44].

3.2 Other Waste Forms

Spent fuel and radioactive waste must be isolated from the environment. In the following sections a brief review of engineered barriers that will be employed in conjunction with sequestration. Sequestration may be in an above ground cask or tomb, as well as natural barriers such as deep sea burial, or in an underground repository. An underground repository's geology may consist of salt beds or salt domes, volcanic tuff, basalt, or granite. Yucca Mountain is an example of volcanic tuff, while the Waste Isolation Pilot Plant (WIPP) is a salt bed repository (WIPP accepted its first waste shipment in 1999 and continues to operate [45]).

The spent fuel from a nuclear reactor is primarily UO_2 which is inherently unstable in aqueous systems [46]. Inside a nuclear reactor the pelletized uranium oxide is encased in a zirconium cladding which keeps water from reacting with the fuel. During fission the fuel swells and gases are generated which add strain and stress to the fuel and cladding [47]. These stresses lead to break up of the UO_2 pellet, and with time increase the likelihood of a cladding breach [48]. This is usually manageable in the 24 months residence in a reactor [45], but for long term stability secondary

measures must be employed to assure immobilization of the spent fuel. The current Yucca Mountain proposal has engineered special canisters for the long term containment of the spent fuel. These multiple barrier containers will contain entire fuel bundles for thousands of years. The purpose of these waste canisters include physical containment for shipping and handling, radiation shielding, and to isolate the waste from the natural barriers [49].

3.2.1 Vitrification

Radioactive waste immobilization via vitrification has an extensive history and worldwide usage [50] and testing [51]. During vitrification glass frit is mixed with the waste to be treated and heated until it becomes a liquid. The liquid glass is transferred to a container, where it forms the final shape and cools. Various types of nuclear waste have been vitrified, one example is high level tank waste from Hanford. Hanford waste was vitrified at 1150°C for 2.5 h to produce a borosilicate glass. Once the waste glass has been manufactured it is transferred to a repository. High level radioactive waste glass shipments have been accepted at the WIPP for long term isolation [52, 53].

The high temperatures required for vitrification may volatilize low melting point waste constituents, such as cesium and technetium. The volatility of cesium, and the various mitigation methods in vitrification systems have been investigated by Kamizono [54]. One technique employed to aid retaining the volatiles is to cover the melt surface with a cold cap [55]. A slurry is fed to the top of the melter forming a crust on the surface of the melt pool, this crust or cold cap reduces the amount of volatiles that escape the melt [56]. Other methods to reduce or eliminate volatility include absorbing the waste in a media, such as a zeolite [57], ion exchange resin [58], or crystalline silicotitanate [59], and then vitrify the resulting compound. These treatments report reductions in the volitization of cesium during the vitrification process.

3.2.2 Grout, Concrete and Geopolymers

The use of grout and concrete are usually limited to low level waste and intermediate level waste. They are favored for their low cost and simple application [60]. A drawback when applied to the immobilization of cesium-containing waste is the tendency for the cesium to stay in the aqueous region within the cementitious media [61]. To incorporate the cesium into the mineral phase, methods similar to what has been done to improve vitrification are applied. The use of zeolites or resins to first absorb the cesium before mixing with the concrete or grout improved leachability characteristics [62]. Geopolymers are primarily amorphous solids produced by mixing alumino-silicates with concentrated alkali solutions. Their application to the immobilization of radioactive waste has been tested by Perera and others [63, 64]. By mixing fly ash or metakaolinite with alkali solutions and polymerizing at 90 °C they found 1 wt% cesium and strontium could be effectively immobilized.

3.2.3 Zeolites and Ion Exchange Materials

Zeolites and ion exchange materials can be used to remove the radionuclides from a solution and trap them in the exchange medium. The sorption of radioactive liquid wastes has been studied with the zeolite clinoptilolite to remove Cs and Sr isotopes [65]. Researchers recommend concentrations below 3×10^{-9} mg/L and pH should be kept ~ 8. Kaolinite powders have also been investigated to reduce Cs and Sr emissions from high temperature processes [66]. This work displayed possible improvements to incineration and vitrification processes due to the kaolinite powder's ability to scavenge these metals from a vertical combustor.

In 1997 Pacific Northwest National Laboratory under the Department of Energy was contracted to investigate radionuclide uptake of a number of different engineered inorganic ion exchange materials from 105-KE Basin water. The study concluded that KCoHex (potassium cobalt hexacyanoferrate) and SZ-72 (modified zirconate)

removed over 99% of the ^{137}Cs. In the same study they found ^{90}Sr was most effectively removed with pharmacosiderite and sodium nonatitanate with an ability to absorb greater than 99% of the strontium from the basin water [67]. The stability against leaching of these ion exchange materials, or absorbers, can be improved with the addition of a sintering step [68]. Similar improvements can be made by mixing the material with another binding agent, *i.e.* cement [61]. Mimura and Akiba were able to produce cesium and strontium loaded ceramic solids from zeolites. To have a consistent particle size in their feed, they first pulverized and sieved mordenite and Zeolite A. The mordenite was saturated with cesium, and the zeolite A was saturated with strontium as well as both cesium and strontium. The ions were dissolved in 1 M nitrate solutions. These were filtered and dried at 250 °C then cold isostaticly pressed at 78 MPa followed by calcination at 1200 °C. The final products consisted of pollucite ($CsAlSi_2O_6$) and strontium feldspar ($SrAl_2Si_2O_8$) [32].

3.2.4 SYNROC

SYNROC or synthetic rock is a durable robust method to treat waste steams. The method was developed at the Australian National University, and first described in 1978 [69]. As the name implies, SYNROC is a synthetic rock, composed of titanium mineral assemblages to mimic natural rocks. The minerals are tailored to the type of waste being treated, such as perovskite for strontium, and hollandite for cesium immmobilization. The mineral oxide precursors are intimately mixed then slurried with the waste calcined, then hot pressed into the final waste form. These waste forms are resistant to leaching even at elevated temperatures and can hold virtually all types of high level waste. SYNROC is considered second to vitrification, but has displayed superior mechanical behavior, was found to be more stable thermally, and can support higher loadings of certain types of waste as opposed to vitrification [70].

The immobilization of cesium in hollandite melts was investigated by Carter and others [71]. They prepared samples via an alkoxide route, where molar quantities of

the required alkoxides are dissolved in water with the necessary nitrates. The solution was then dried and calcined in air at 750 °C for two hours. These were melted in Pt crucibles in air at 1450-1550 °C. They found ~7.5 wt % Cs_2O could be prepared with Cr^{3+}, Ni^{2+}, Zn^{2+} or Co^{2+} resulting in hollandite ceramics with PCT-B normalized Cs leachate concentrations <0.2 g/L. The PCT-B leach procedure requires sample powders to be within 75-150μm, which are then ultrasonically washed prior to testing. The leach test requires holding 1 g of powder in 10 ml of de-ionized water for 7 days at 90°C, the resulting leachate solution is analyzed for suspended ion concentrations. Their work continued with a hot isostatic pressing (HIP) route which reduced the processing temperatures. Instead of melting in air, the powders were heated to 1275 °C at 30 MPa for an hour. These experiments also incorporated strontium with cesium resulting in a 12 wt % loadings. A SYNROC rich in the mineral rutile was also tested for the immobilization of Tc [72].

A report by Tripp and Maio [73] concluded Synroc would be an effective cesium and strontium immobilization method, but would not rule out steam reforming as an alternative. The drawbacks of the SYNROC process are complex preprocessing, the stoichiometry must be tailored to produce the desired final minerals, and the sintering is done at high temperatures and pressures.

3.2.5 Steam Reforming

Steam reforming is a waste treatment method where a liquid waste is injected into a fluidized bed along with the necessary co-reactants at an elevated temperature. [Steam is added or is part of the feed stream.] Typical co-reactants are different types of clay which provide silica and alumina, and carbon sources to facilitate organic and/or nitrate destruction. The products are solid alumino-silicates [74].

Steam reforming of various types of radioactive waste, including tank wastes [75, 76], radioactive graphite [77], and low level mixed wastes [78], have been tested among others. Radioactive waste treatment with steam reforming has been applied

to cesium and strontium bearing separation product solutions as well. Tripp *et al* found strip solutions from several cesium and strontium separation methods could be converted to solids forms, without volatization of cesium while destroying the organics and nitrates in the process. The final product was a leach resistant aluminosilicate. The product does have a water soluble fraction of cesium and strontium, the quantity depends on which process feed was used. The peak concentrations of unmineralized product, or water soluble solids were 22% for cesium and 10% for strontium. Another issue of concern is the production $<\mu$m particles [79].

3.2.6 Calcination

Calcination refers to the treatment of liquid radioactive wastes by heating to oxide. This method has been applied to various liquid wastes in different ways. A few examples are fluidized-bed calcination, pot calcination, radiant heat-spray calcination, rotary ball-kiln calcination, and calcination in molten sulfur [45]. These are effective techniques to remove liquids and reduce volume. The waste produced by these processes is usually a powder or granular form. Once dry, the waste must be containerized in a method adequate to avoid dispersal into the environment. A container may also be needed to keep water from dissolving or moving the waste if no fixation is applied.

A method to immobilize calcine from low level sodium- aluminum- and zirconium-bearing waste, involved mixing the calcine with Portland cement, blast furnace slag, and fly ash, researchers found the product reduced volume and met leach requirements [80]. Another method found to improve leachability and performance is the addition of metakaolin and a NaOH solution to the calcine followed by mild curing, which produced a durable solid [81]. This waste form is known as hydroceramic.

4. EXPERIMENTAL METHOD AND ANALYSES

Simulated waste was prepared from stable isotopes of cesium, strontium, barium and rubidium. Nitrates of each metal were dissolved in dilute nitric acid. Then this solution was added to bentonite clay. Bentonite clay was used as received (American Colloid Company of Belle Fourche, SD provided Volclay HPM-20, 425 mesh) The composition reported by American Colloid was SiO_2 = 69.56%, Al_2O_3 = 20.69%, MgO = 2.70%, Fe_2O_3 = 4.85%, CaO = 1.30%, Na_2O = 2.43%, K_2O = 0.30%. The loss-on-ignition was 4.80%. The specific gravity was 2.6 and the pH of a 2% solid suspension was 8.5-10.5 [82]. Laboratory-supplied deionized water was used for all experiments, except for TCLP where purchased deionized water was used instead.

4.1 Sample Preparation

The first step was to create a simulated waste liquid. The waste liquid was then added to the bentonite clay. The bentonite clay and waste solution were dried to a powder, the powder was then pressed into pellets to be sintered. Pellets were sintered at various temperatures and waste concentrations.

4.1.1 Simulated Waste

The FPEX process stream will produce a strip solution of dilute nitric acid containing cesium, strontium, barium and rubidium ions. Cesium and strontium are the primary targets of immobilization, while the rubidium and barium are co-extracted due to their similar chemistry. The quantities of waste ions in the proposed waste stream are relatively dilute. Ion ratios of Cs:Rb of 3340:537 and Sr:Ba of 1180:3100 were used in the simulated waste. The ion quantities were 2:1 Cs to Sr by mass in the solution. These were provided by ORIGEN simulations of the UREX process raffinate developed by Argonne National Laboratory (personal communication with

Table 4.1
Simulated waste solution composition

Component	Qty	MW	moles/L
HNO_3 70%	103.97 ml	63.01	1.64
$Ba(NO_3)_2$	14.183 g	261.34	0.054
$CsNO_3$	11.90 g	194.91	0.061
$RbNO_3$	2.27 g	147.47	0.014
$Sr(NO_3)_2$	6.88 g	211.63	0.033

Candido Pereira, 2005). Nitrates of the required ions were chosen for the waste simulant. The nitrates were dissolved into a dilute nitric acid solution. The ion concentrations of these metal ions were increased to the point of saturation in order reduce the volume of liquid required to process (Table 4.1). To completely dissolve the nitrates the salts were stirred with a magnetic bar for ~24.

4.1.2 Bentonite Waste Loading

The concentrated waste solution was added to the clay then stirred, the water was driven off by placing the beacker in an oil bath at approximately 110°C. The process was repeated until the desired concentration metal ions was reached. The clay was mixed as the waste solution heated to dryness to prevent hot spots and to homogenize the powder.

The clay waste concentrations were based on the mineral pollucite. Pollucite is a natural source of cesium, which contains silicon and aluminum oxides. This mineral has had extensive study as cesium immobilization compound [5–7,35]. In addition to cesium, natural pollucite also contains sodium; if we assume sodium can be replaced by cesium the potential cesium content is approximately 42 mass %. 30 % was

chosen as a theoretical maximum loading for the clay based on the amount of alumina available to produce pollucite and feldspars from the cesium, rubidium, barium, and strontium. Various percentages of the pollucite based theoretical maximum were chosen as loadings for comparison.

After reaching the desired waste content, the dried clay powder was ground by mortar and pestle. A small amount of loaded unsintered clay was allotted for differential scanning calorimetry and thermal gravometric analysis, as well as a reserve. The powder was then axially pressed to 2000 lbs in a 5/8" die (~6500 psi) to create a green puck. The pucks were then sintered.

4.1.3 Sintering

The sintering temperatures were varied from 700°C to 1400°C. The ramp rates were held constant at 5° per minute for all sinterings. Once reaching the desired temperature, samples were soaked for 12 hours. Cooling was initially controlled to 5°C per minute but eventually the cooling rate decreased to a much slower natural rate.

4.2 Analyses

After samples were prepared a series of analyses were performed to characterize the material properties.

4.2.1 Bulk Properties

Masses and dimensions of the pucks before and after sintering were collected for comparison. The true volume was calculated with a Quantachrome helium pycnometer. A sample was placed in a known volume and pressurized, a working gas enters the empty space including the open porosity, in this case helium up to ~0.117 MPa.

Next a valve is opened allowing the gas to be shared with another known volume. With the initial pressure and the final pressure the sample volume can be calculated using an expression of Boyle's law (4.1)

$$V_p = V_c - V_r \times ((P_1/P_2) - 1) \tag{4.1}$$

where V_p is the sample volume, V_c is the sample cell volume, V_r is the reference cell volume, P_1 is the pressure in the sample cell and sample, and P_2 is the pressure after opening the connecting valve between the sample cell and the reference cell. With the volume of the sample, and its meaured mass the true density can be determined. By comparing the true density to the bulk density, the porosity is calculated(4.2).

$$Porosity\ \% = (1 - (bulk\ density/true\ density) \times 100 \tag{4.2}$$

Bulk density was calculated by measuring the sample dimensions. The color and changes in shape, such as slump and cracking were also noted.

4.2.2 Differential Scanning Calorimetry and Thermal Gravimetric Analysis

Unsintered bentonite clay samples were subjected to a controlled heating rate in a Netzsch STA 409 PC *Luxx* simultaneous thermal analysis instrument, with Proteus Software. The instrument performs a thermal gravimetric analysis (TGA), as well as differential scanning calorimetry (DSC) on each sample in tandem over a specified heating profile. The sample is loaded into an alumina crucible of know mass, which then is set on a sensitive balance. The balance resolution is 2μg, while the error in mass changes in our process is ~40μg. Along with the sample an empty, but identical alumina crucible of known mass was loaded as a reference. Heat flux is measured with a pair of thermocouples attached to bottom of each of the crucible mounting points. The reference signal is subtracted from the sample to obtain endothermic and exothermic rates and transitions.

The heating rate was 5° per minute from room temperature to 1400°C. Argon flowed at 50 ml/min to act as a cover gas. Before analysing the samples, the heating

program was run with empty crucibles to create a baseline signal. The baseline signal contained the weight and thermal behaviour due to the crucible as well as any buoyancy effects resulting from the flow of the cover gas. The baseline was then subtracted from the data acquired from the samples. This step corrects for instrument trends, leaving only data due to the samples. Each sample was 20–50 mg.

4.2.3 Light Flash Analysis

Thermal diffusivity and specific heat were measured with a Netzsch Light Flash Analyzer (LFA) 447 *NanoFlash* instrument. Disc samples were first cut and ground to 2 mm ±0.06 mm thick and 12.7 ±0.14 mm in diameter for 800–1000°C; 700°C specimens were prepared identically except they were 15.4 mm square. The instrument used a short light pulse from a xenon lamp to heat the the bottom side of the sample. An infra-red sensor measured the temperature change on the opposing side as a function of time. Thermal diffusivity is determined using the half-time method (4.3) [83].

$$\alpha = 0.1388 \times d^2/t_{1/2} \tag{4.3}$$

Where α is the thermal diffusivity, d is the sample thickness, and $t_{1/2}$ is the time to reach half the maximum temperature. The system applies mathematical regression routines to adjust for radial and facial heat losses, as well as finite pulse effects. The specific heat C_p is simultaneously measured on the same specimen. With the known density ρ the thermal conductivity λ can be calculated (4.4).

$$\lambda(T) = \alpha(T) \times C_p(T) \times \rho(T) \tag{4.4}$$

4.2.4 X-ray Powder Diffraction

The x-ray powder diffraction (XRD) was done by the Texas A&M University Chemistry Department's X-ray Diffraction Laboratory. The instrument used was a Bruker-AXS Advanced Bragg-Brentano X-Ray Powder Diffractometer. Specifications and operating parameters are listed in Table 4.2.

Table 4.2
XRD instrument specifications. Bruker-AXS D8 Advanced Bragg-Brentano X-Ray Powder Diffractometer

Specifications	
D8 Goniometer	
Lynxeye Position Sensitive Detector	
Copper X-ray Radiation	
Software: EVA, Bruker AXS Inc.	
Database: PDF-2, International Center for Diffraction Data (ICDD)	
Operating parameters	
Power	40 kV, 40 ma
Step size	0.015 degree 2θ
Scan Speed	0.1 seconds per step

Samples were prepared for XRD by pulverizing briefly (≤1 minute) in a WIG-L-BUG (Model 3110B) grinding mill with a steel ball bearing. Powders were checked with a Hirox optical microscope (Model KH 1300) to assure particles were in the 5-10 μm range.

4.2.5 Scanning Electron Microscopy and Wave Dispersive Spectrometry

The electron microprobe is an instrument very similar to a standard scanning electron microscope (SEM), but instead of focusing on the imaging of samples, the microprobe is designed primarily for chemical analysis. The electron microprobe has an electron column that consists of an electron source, typically a tungsten filament (but also lanthanum hexaboride is used), and focusing magnetic lenses and apertures. The column is held at a vacuum of 1×10^{-4} to 1×10^{-5} Pa. An electron beam is focused on the sample with a spot size of 0.1 to 1 μm. Electron energies can be adjusted from 5-50 keV. The sintered bentonite samples were run at 15 keV and 20 nA to obtain elemental data, while most of the backscattered electron images we acquired at 15 keV and 3 nA. When electrons strike the sample a series of electron interactions occur and secondary, backscattered, and auger electrons are emitted. Some electrons are absorbed, and they create heat, visible light and also x-rays. These x-rays can be created by two mechanisms. The bombarding electron may be decelerated when interacting with the nucleus of the atoms in the sample or the electrons surrounding the nucleus. The energy lost results in the emission of an x-ray of a continuous energy range up to the accelerating potential of electron beam. The beam electron may also interact with an inner shell electron transferring its energy to the inner shell electron ejecting it from the atom, or raising the electron to a higher energy shell. This last type of interaction results in the energized electron falling back into the vacant inner shell, resulting in either another electron being ejected with energy related to electon transition, or the emission of an x-ray photon with the energy equal to the difference between the electron shells. These characteristic x-rays are useful for elemental determination, and are responsible for energy dispersive spectroscopy (EDS) and wave dispersive spectroscopy (WDS).

Most electron microscopes have an energy dispersive spectrometers, but the electron microprobe also has a series of wave dispersive spectrometers. These spectrometers consist of a rotatable, oriented diffraction crystal coupled with a proportional

gas-filled ionization detector. These two are arranged in a geometric relationship according to Bragg's Law (4.5)

$$n\lambda = 2d\sin\theta \tag{4.5}$$

where n is the order of diffraction, λ is the wavelength of the characteristic x-ray (Å), d is the atomic spacing of the diffracting crystal (Å), and θ is the angle of incidence. Depending on the angle of incidence the x-rays will combine constructively or destructively. The choice of crystal, the arrangement of the crystal, and detector is determined by the element of concern's characteristic x-ray wavelength. X-ray detectors are usually Li-drifted silicon or a high-purity germanium.

This system allows for the resolution of peaks about an order of magnitude better than EDS, and an improved peak/background ratio by an order of magnitude.

WDS system is also capable of quantitative analysis. A series of detectors are set to count for separate elements during a scan of a sample, providing ratios of each element found. There are several issues that will affect accuracy and precision of the instrument that must be considered, such as interferences between various characteristic x-rays that need to be accounted. For a full description, see the source reference [84].

WDS Sample Preparation

Samples were mounted in epoxy (Buehler Ltd), from resin and hardener (Epo-Kwick). Mounts were allowed to set over night. Polishing was done with sandpaper up to 1200 grit for low sintering temperatures 700 - 1000°C. Samples sintered from 1100 to 1200°C were also polished with 3μm diamond spray followed by 1/4 μm spray, then ultrasonically cleaned in 100% ethanol. The mounted samples were sputter coated with ~15nm of carbon.

Acquisition Settings

The accelerating voltage was set at 15kV and 20nA to produces an electron spot size of approximately 0.5μm. The electrons excite a tear drop shaped area $\sim 1\mu m$ in diameter and $\sim 1.25\mu m$ deep from which characteristic x-rays are produced. The x-ray detectors were arranged at a distance multiple of the wavelength of the characteristic x-ray of the elements of concern. The crystals were chosen depending on the particular x-ray of interest (Table 4.3).

Table 4.3
WDS crystal types and associated elements. (TAP: thallium acid phthalate, PET: pentaerythritol, LIF: lithium fluoride)

Element	Line	Crystal	Standard
Na	K-α	TAP	albite
Rb	L-α	TAP	RbI
Mg	K-α	TAP	hornblende
Al	K-α	TAP	albite
Si	K-α	PET	hornblende
Ca	K-α	PET	hornblende
Sr	L-α	PET	$SrTiO_3$
Fe	K-α	LIF	hornblende
Cs	L-α	LIF	CsBr
Ba	L-α	LIF	$BaSO_4$

4.2.6 Neutron Activation Analysis

Neutron Activation Analysis (NAA) was done at the Texas A&M Triga Mark I research reactor. The reactor is pool-type, with sample port tubes for sample

irradiation. Samples were exposed to 10.0×10^{13} neutrons/cm^{2}s at 100 kW. Known quantities of representative standards were run under identical conditions, then compared to unknown samples and quantified using the ratio method. Analysis was done with Genie 2000 software (Canberra Inc.).

Due to the presence of cesium, in our samples short exposures (60 seconds) and long exposures (1 hour) were required. Cesium's very high activation rate hid any signal due to strontium over long exposures. Short exposures were necessary to detect the strontium signal. For short runs samples are pneumatically inserted and pneumatically removed allowing samples to be removed from the neutron flux quickly. Samples were then counted after being removed from the reactor.

4.2.7 Toxicity Characteristic Leach Procedure

The Toxicity Characteristic Leach Procedure (TCLP) is a protocal that is defined very specifically under the Resource Conservation and Recovery Act [85]. Samples under analysis are exposed to an acetic acid solution for a predetermined amount of time while mixed. The liquid is then analyzed to quantify the concentration of various listed substances. If the concentration of any listed toxin is above guideline limits the waste is considered hazardous. If the waste fails the TCLP it must be disposed in a hazardous waste facility.

A simplified TCLP, taken from personal communication with Michael Kaminski 2009, was performed on the sintered clay samples as a baseline leachability test. This is not a definitive leach resistance test, but only used to compare between the different sinterings and loadings of these particular samples.

TCLP Reagent and Sample Preparation

Each sample of sintered bentonite clay was ground to a powder by mortar and pestle and sifted through # 100 sieve to $\leq 150\mu$m. The simplified TCLP required 5

grams of powder added to 96.5 mL DIW in a 500 mL beaker. The simplified TCLP differs from the regulatory procedure and is only for comparison of our samples to each other, passing the simplified TCLP has no legal consequence.

Steps of Simplified TCLP

1. Place 5 grams of sample powder in a 500 mL beaker, add 96.5 mL DIW, cover with a watch glass, stir vigorously on a magnetic stirrer for 5 minutes. Measure and record the solution's pH.

2. For pH <5 got to step #3. For pH >5, go to step #4.

3. Prepare fluid #1: Add 5.7 mL glacial acetic acid to 500 mL DIW, add 64.3 mL of 1 N NaOH, then dilute to a volume of 1 L. The resulting pH should be 4.93 ± 0.05. Procede to step #6.

4. For pH >5, add 3.5 mL of 1 N HCl, slurry briefly, cover with a watch glass, heat to 50°C and hold at 50°C for 10 minutes. Allow the solution to cool to room temperature and record pH. If pH is <5, proceed to step #3. If pH is >5, proceed to step #5.

5. Prepare fluid #2: Dilute 5.7 mL glacial acetic acid with DIW to a volume of 1 L. The resulting pH should be 2.88 ± 0.05. Proceed to step #6.

6. Transfer 50 grams fo powder (100 mesh) into 2.2 L polyethylene bottle, add 1000 grams of fluid specified above and seal bottle tightly with teflon tape.

7. Agitate bottle at 30 ± 2 rpm for 18 ± 2 hours.

8. Filter leachate thruogh 0.7 μm filter.

9. Add 20 mL of extract to each of two labeled sample vials. Measure the pH of the two vials.

10. Add 100 mL of the extract to another two labeled vials for cation analysis. Add 1 mL of concentrated HNO_3 to each vial to ensure a pH <2.

11. Save additional leachate for analyses if needed.

Leachate solutions were anayzed with iductively coupled plasma mass spectroscopy (ICP-MS) either at Texas A&M Trace Element Laboratory for samples sintered at 700, 800 and 1000°C, or Argonne National Laboratory for samples sintered at 1100 and 1200°C.

4.3 Waste Form Heat Generation Model

Calculations with experimental data collected in this study were input to a model described by Kaminski [86]. The model will determine waste form radius, assuming a right cylinder with an input maximum centerline temperature. The model accounted for the different isotopes and only required the wt% of cesium and strontium, thermal conductivity, density, and a maximum center-line temperature. The model assumes passive cooling with air at 90°C with natural convection. The waste form was assumed to be inside a stainless steel canister 0.02 m thick. The spent fuel was assumed to be 4.25 enriched uranium, with burn-up at 50GWD/ton, and 20 years of cooling. The isotopic composition of the spent fuel was determined from ORIGEN simulations by J. Stillman (ANL).

5. RESULTS

Upon sintering at higher temperatures the clay color transformed from a reddish brown at 700°C to a pale yellow at 1200°C (5.3). The samples at lower sinterings were brittle and pulverized easily, while those sintered at ≤1000°C became very hard and were much more difficult to pulverize.

5.1 Bulk Properties

Sinterings ranged from 700°C to 1400°C, but at 1400°C the samples melted completely. The lowest waste loading, ~15 wt% waste, became bloated when sintered at 1200°C resulting in a pumice-like porous mass. When the waste loading was increased to 18 and 21% wt% the samples distorted less severly, swelling and cracking slightly, loadings above 21 wt% had a smooth texture and uniform coloration (Figure 5.1).

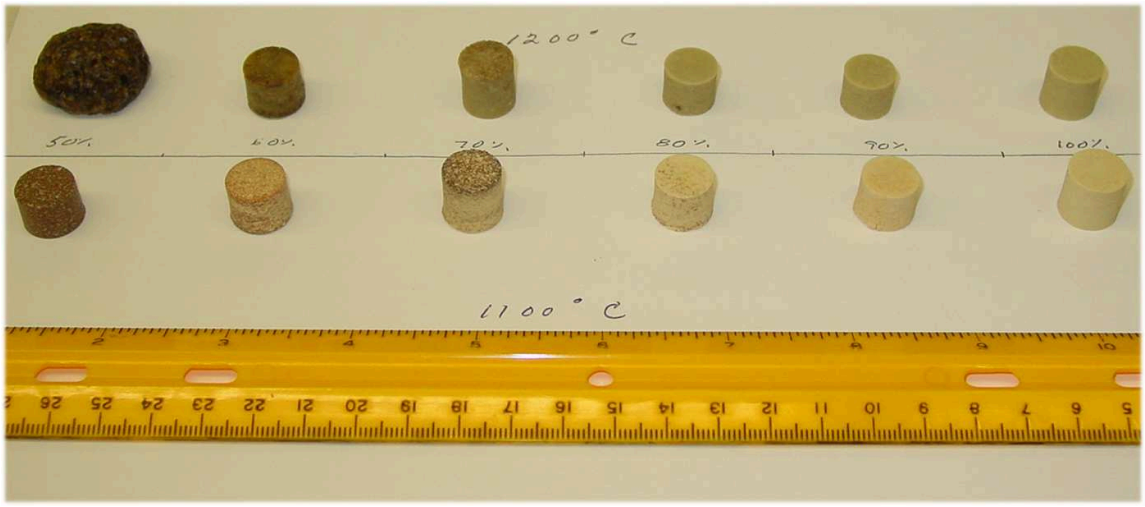

Fig. 5.1. 1100°C and 1200°C sintered bentonite clay various loadings.

At sintering temperatures ≤1000°C the color transformed from a reddish brown at the lowest sintering temperatures to a pale yellow at the highest. The color of the samples sintered at temperatures 800 through 1000°C resulted mottled combinations. Lower loadings at 700, 800, and 1000°C sintering temperatures displayed darker coloration than the 100% loaded samples (Figure 5.2), the ceramics had the lightest coloration at 1100°C at loadings >80% and the 1200°C became darker (Figure 5.3). The bentonite tranformed from a brick colored, rough texture 700°C to a pale yellow, hard glassy ceramic at 1200°C (Figure 5.3).

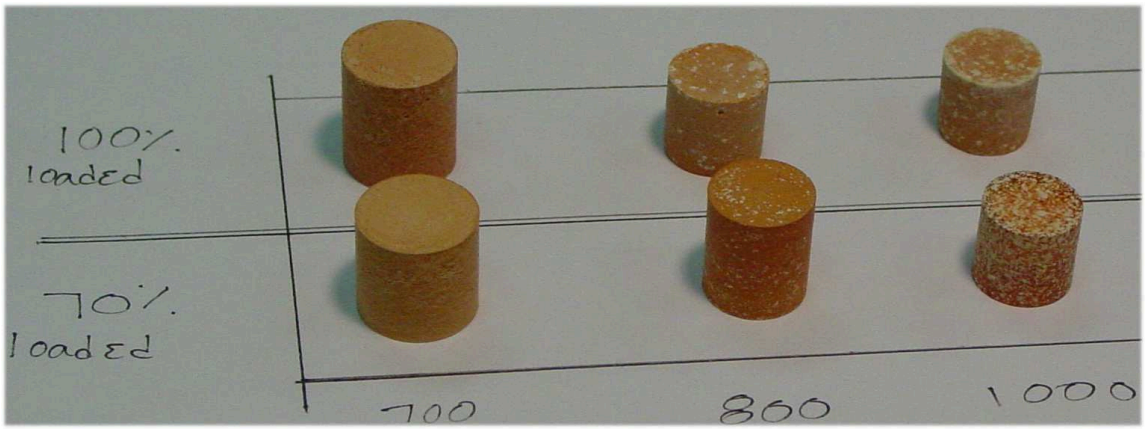

Fig. 5.2. 700, 800, and 1000°C sintered bentonite with 24%-32% waste loadings.

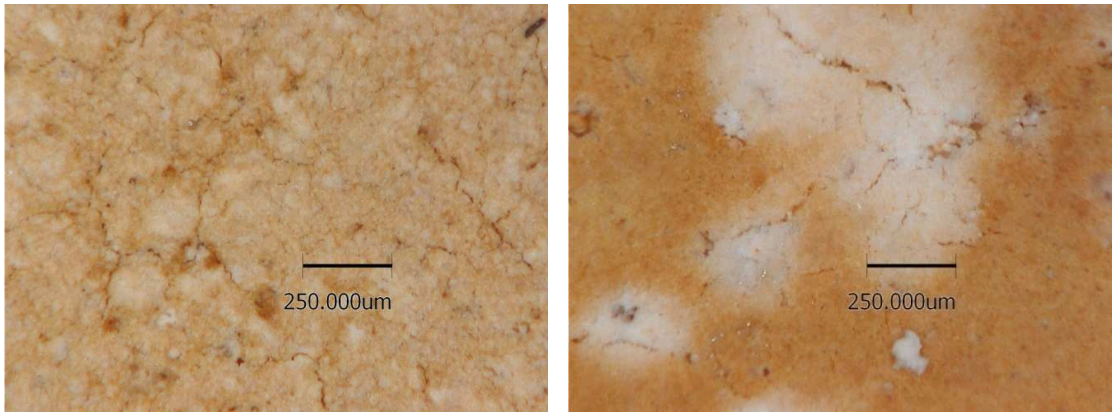

(a) 700°C 32wt% waste

(b) 800°C 24wt% waste

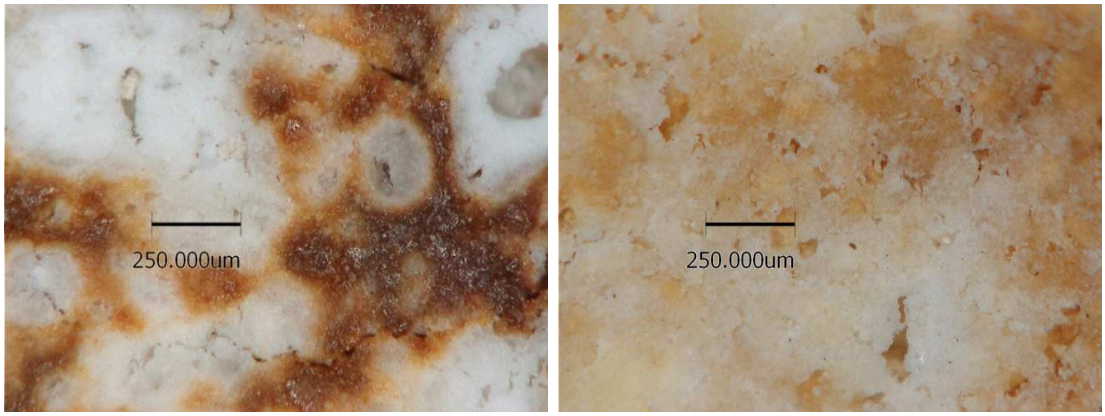

(c) 1000°C 26 wt% waste.

(d) 1000°C 31wt% waste.

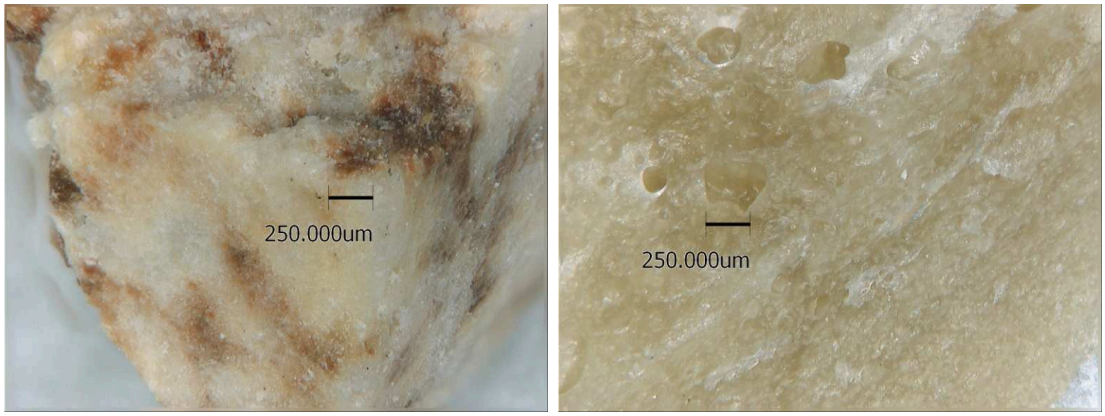

(e) 1100°C 21wt% waste

(f) 1200°C 21wt% waste

Fig. 5.3. Bentonite clay sintered at 700, 800, 1000, 1100, and 1200°C with various waste concentrations

5.1.1 Density

The bulk density trends were variable, generally increasing with loading and sintering temperature. At 700, 1000, and 1100°C there was a drop in bulk density at the highest loadings (Table 5.1).

Table 5.1
Bulk densities of sintered bentonite. Density as a function of maximum theoretical loading and sintering temperature.

Bulk density g/cm^3					
	Sintering Temperature°C				
Loading (% of max)	700	800	1000	1100	1200
100	1.21	1.78	1.84	2.18	2.53
90				3.03	2.51
80				2.95	2.55
70	1.24	1.76	2.02	2.94	2.41
60				2.89	2.12
50				2.73	

5.1.2 Porosity

The porosity of the samples was reduced with increasing sintering temperature. The lowest porosity was at the highest sintering temperature of 1200°C at 100% loading with 4.7%. The porosity 1100°C was higher than at 1000°C at 70% loadings of the theoretical maximum. The lowest sintering temperature of 700°C resulted in ceramics with greater than 50% porosity (Table 5.2).

The porosity of the clay varied substantially from sintering to sintering. When plotted with thermal conductivity on the Y-axis and porosity on the X-axis (Figure

5.4) we have the relationship predicted by Coble and Kingery [87]. The higher density at the higher sintering temperatures will produce a higher thermal conductivity.

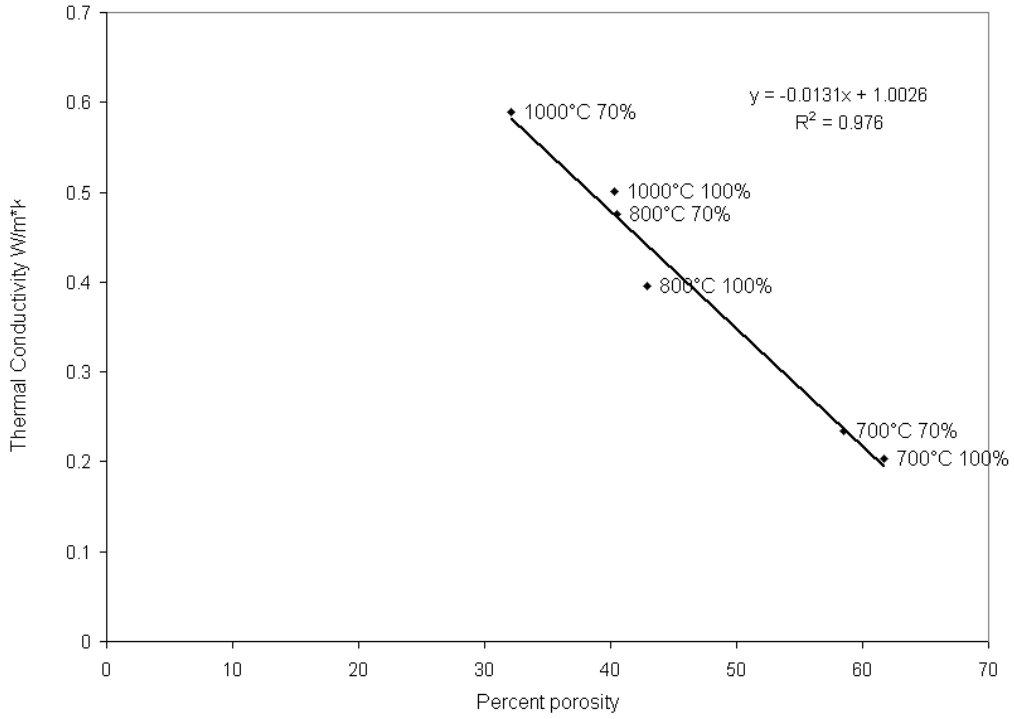

Fig. 5.4. Porosity effects on thermal conductivity of bentonite sintered at 700, 800, and 1000°C waste loadings at 70 and 100% of theoretical maximum.

Table 5.2
Open porosity of sintered bentonite loaded with metal ions.

Open porosity %			
	Loading (% of max)		
Sintering Temperature°C	70%	90%	100%
1200	14.4		4.7
1100	33.6	32.7	
1000	32.1		40.3
800	40.5		43.0
700	58.5		61.7

5.2 Differential Scanning Calorimetry and Thermal Gravimetric Analysis

Thermal Gravimetric Analysis (TGA) records the mass changes under heating. Differential Scanning Calorimetry (DSC) measures the thermodynamic heat flux as a function of temperature. In these plots exothermic heat flux is positive, and endothermic heat flow is negative. DSC-TGA was applied simultaneously to the various unsintered bentonite clay loadings. The results are qualitative only showing trends and onset temperatures. A sample of pure bentonite clay was analyzed as well to document the baseline clay behavior. The pure bentonite has an exothermic bloating reaction accompanied by a small mass loss at 950°C (Figure 5.5). This bloating is attributed to the release of oxygen during the reduction of various oxides in the clay [88]. A similar exotherm occurs >1200°C when the 16% loaded bentonite bloats, but without a detectable mass loss (top left Figure 5.1, and 5.6).

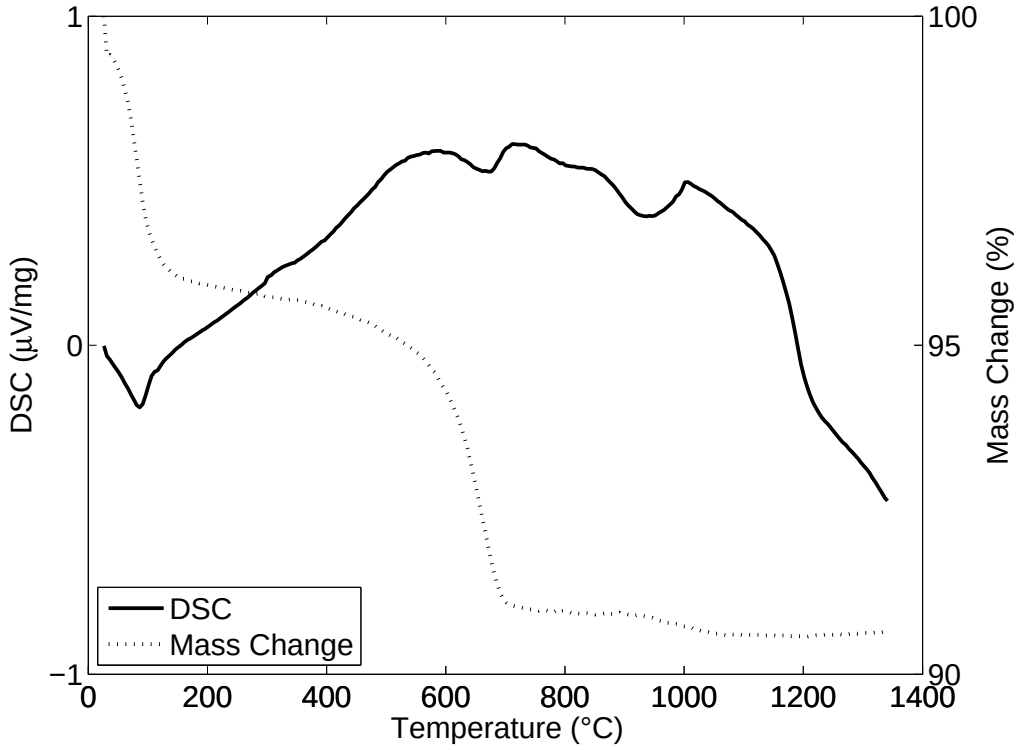

Fig. 5.5. Pure bentonite combined differential calorimetry and thermal gravometry displaying high temperature bloating effects

Each of the loaded bentonite clay samples started with a sharp drop in mass upon initial heating with one exception, the 16 mass percent waste loaded sample (Figure 5.6). This sample was stored in a dessicator prior to analysis and during this time the powder lost most of the loosely bound water.

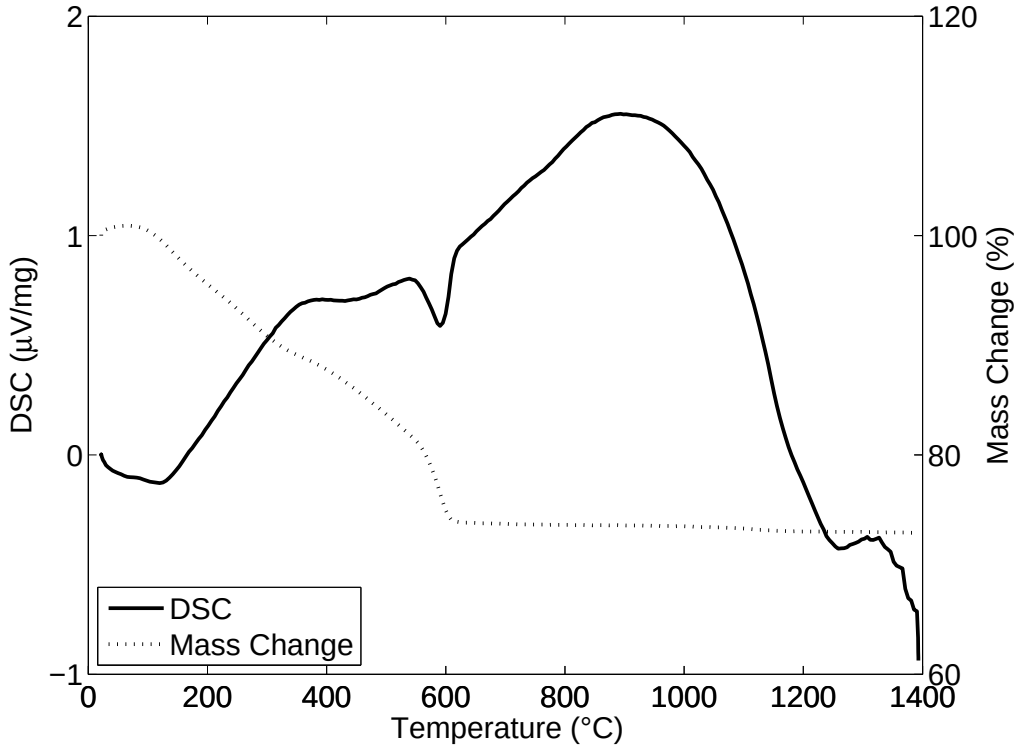

Fig. 5.6. 16 mass percent waste loaded bentonite combined differential calorimetry and thermal gravometry

The dehydration process in montmorillonite has been documented by Onal and Sarikaya [89]. The mass loss rates due to water release coincide with how tightly bound the water is to the clay. Once the heating begins the early steep mass loss is due to the drying of interparticle water. This water comes off quickly then concludes at ≤200°C (Figures 5.5, 5.7). This mass loss has an associated endotherm visible as a negative slope ~150°C.

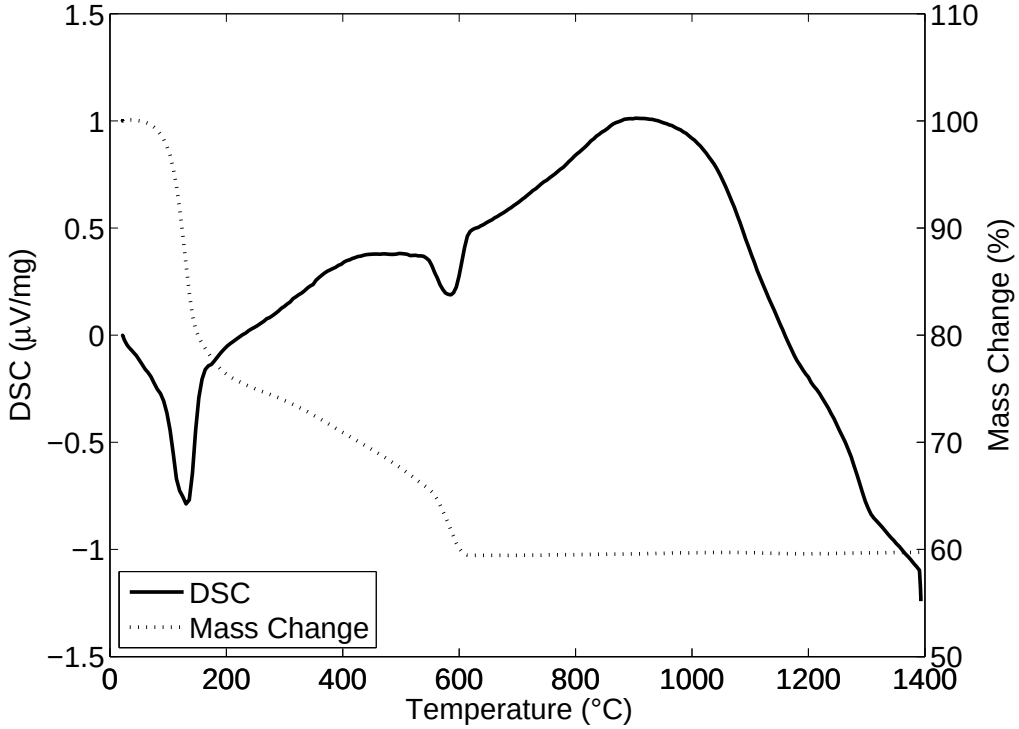

Fig. 5.7. 22 mass percent waste loaded bentonite combined differential scanning calorimetry and thermal gravometry plot

The second mass loss step, with a gentler slope becomes evident once the interparticle water is exhausted. This mass loss is due to adsorbed water and interlayer water. The heat flux is exothermic during this process, seen as a upward trend from 150–200°C concluding at 400–500°C with a plateau (Figures 5.6, 5.7). The interlayer water is held much more tightly than the interparticle water due to cations that also occupy spaces between the clay layers. The cations and the water create partial bonds amongst themselves and with the oxygen attached to the silica tetrahedrals. As the heating continues the mass loss rate transitions to another rapid decline. This final dehydration step is due to dehydroxylation water losses which set in ~500°C in the clay loaded with waste ions, the mass loss concludes ~600°C (Figures 5.6, 5.7) which differs from the pure bentonite at 700°C (Figure 5.5). Onal [89] and Grim [90]

found dehydroxylation mass loss concluded ~800°C. Balek observed when bentonite was saturated with different cations dehydroxylation concluded at 700°C [91].

The heat flux which was flat during the interparticle water drying, becomes sharply endothermic during dehydroxylation reaching an inflection at ~575°C (Figures 5.7, 5.6). The dehydroxylation water release in bentonite clay requires the highest temperature. This is due to hydroxyl groups being molecularly bound within the clay structure. When hydroxylation occurs the lattice of the clay becomes porous and amorphous. This structural damage concludes from 600 to 650°C. Each of these stages is visible in the 16 and 22 mass percent waste loaded bentonite (Figures 5.6, 5.7) as well as the pure bentonite (Figure 5.5). The heat flux returns to an increasing exothermic trend peaking at ~900°C, then becoming endothermic. This endotherm continues until pure bentonite and 50% loadings bloat (Figures 5.5, 5.6), at 1000 and 1200°C respectively. Higher loading ceramics eventually melt at >1300°C. This is known from a glass-like coating on the bottom of the DSC-TGA crucibles.

The onset temperatures for each of mass loss steps are consistent across the samples (Figure 5.8). The first dehydration step is dependent on the amount of initial water in sample which can vary substantially from sample to sample, the ion saturated bentonite is very hygroscopic. All samples lost water continuously until the completion of dehydroxylation step. During this dehydroxylation phase, ~600°C, is also where nitrates are exhausted as reported by Kaminski *et al* [82].

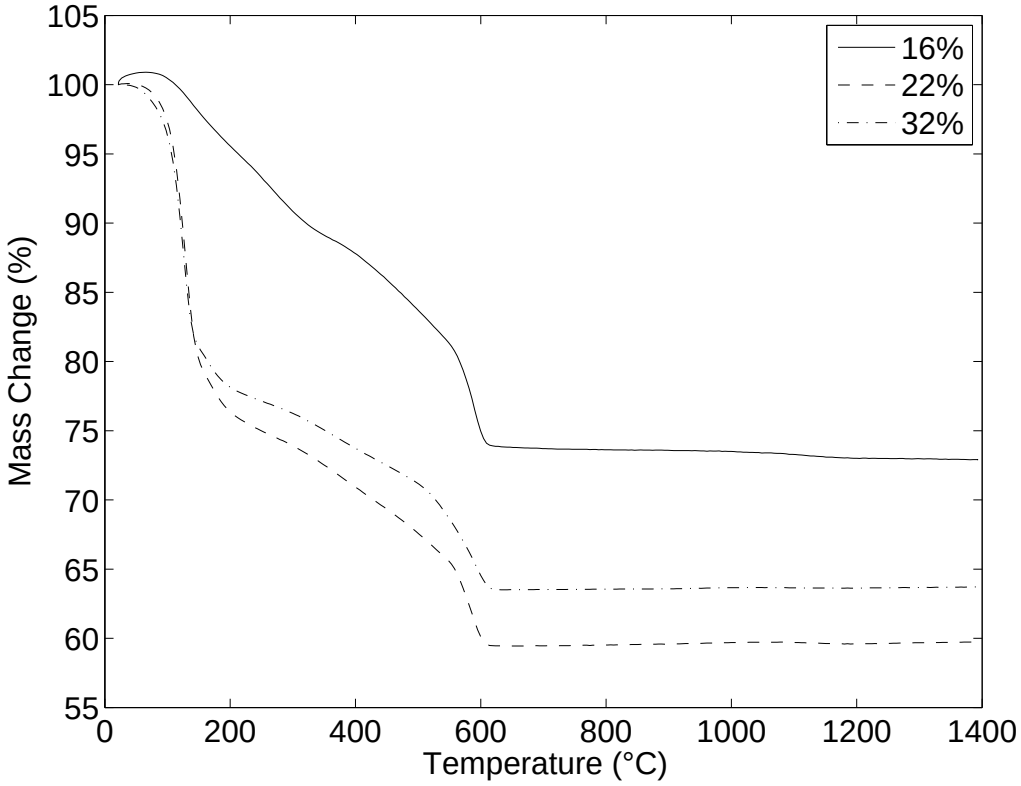

Fig. 5.8. Mass changes upon heating of bentonite clay at various concentrations of waste.

5.3 Light Flash Analysis

Samples sintered at 700°C had the lowest thermal diffusivities that do not exceed 0.24 mm^2/s, with the higher loading slightly higher than the lower 70% waste loading. The specific heat was higher for the lower loading with a maximum at 1.06 J/g·K at 300 K (Figure 5.9). The 700°C 100% loaded bentonite specific heat falls between that of pollucite and Sr-feldspar, but the lower loading exceeds that of both minerals at temperatures >125°C.

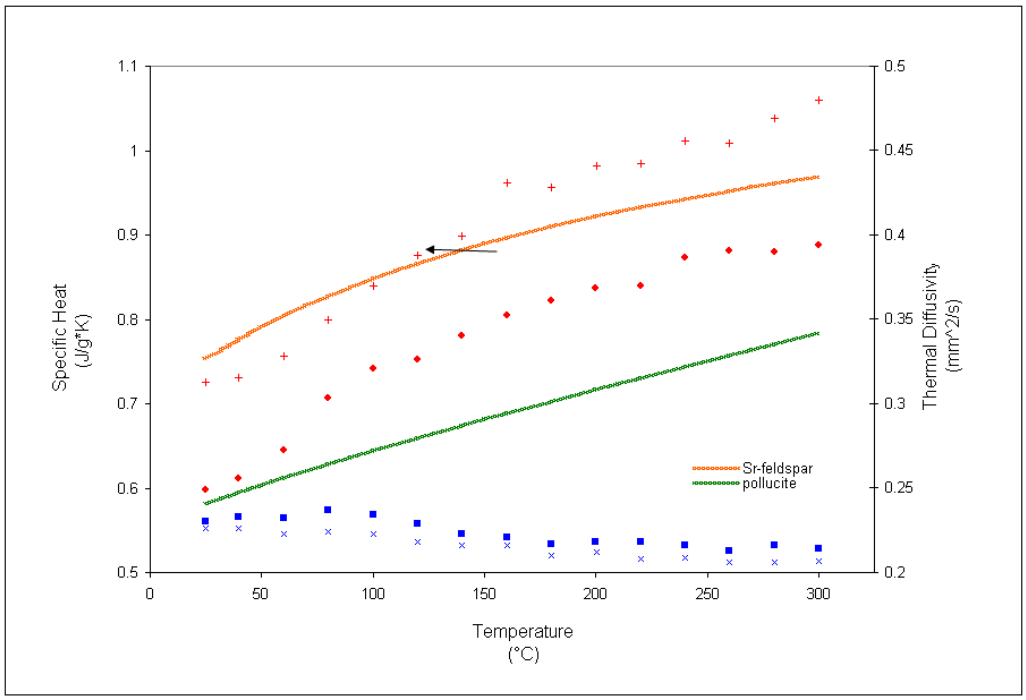

Fig. 5.9. Thermal properties of 700°C sintered bentonite. × refers to thermal diffusivity of 70% loaded bentonite; and ▪ refers to the thermal diffusivity of 100% loaded bentonite; + refers to the specific heat of 70% loaded bentonite; • refers to the specific heat of 100% loaded bentonite; green line is the specific heat of pollucite *Ogorodova, 2003*; and the orange line is the specific heat of Sr-feldspar *Chernyshova, 1991.*

At 800°C sinterings the thermal diffusivities continued to increase from 0.33 at to 0.38 from room temperature to 300°C also with higher thermal diffusivities for higher loadings. Specific heat on the other hand was higher for the lower waste loading reaching a maximum at 0.99 J/g·K at 300°C. The higher loading's specific heat coincides with that of pollucite at temperatures >125°C, the lower 70% loading specific heat was closer to that of Sr-felspar at temperatures >200°C (Figure 5.10).

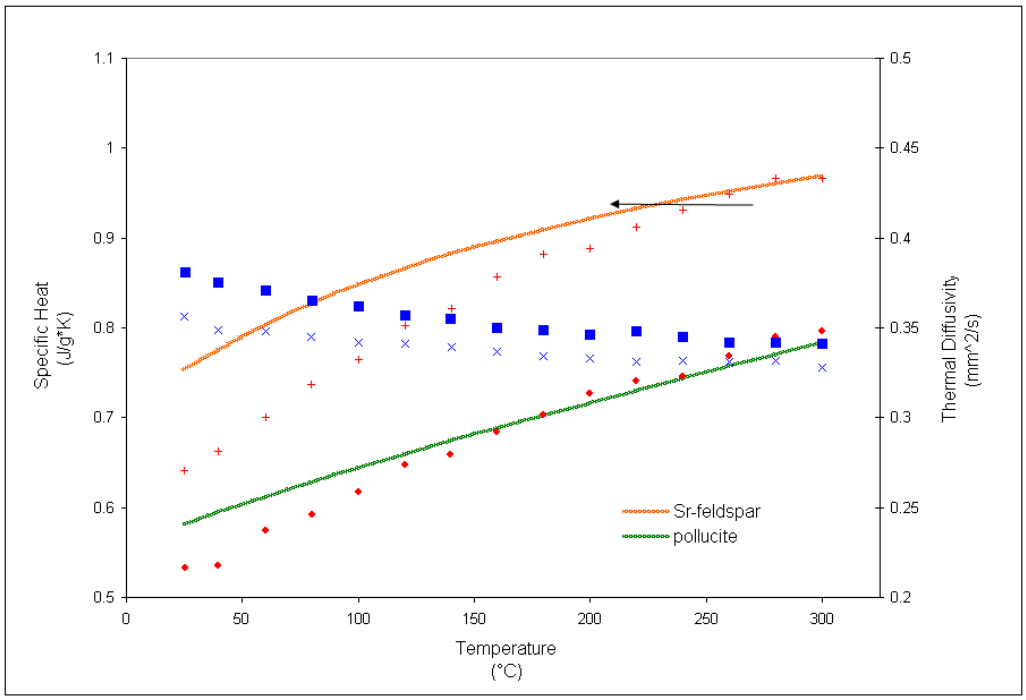

Fig. 5.10. Thermal properties of 800°C sintered bentonite. × refers to thermal diffusivity of 70% loaded bentonite; and ▪ refers to the thermal diffusivity of 100% loaded bentonite; + refers to the specific heat of 70% loaded bentonite; • refers to the specific heat of 100% loaded bentonite; green line is the specific heat of pollucite *Ogorodova, 2003*; and the orange line is the specific heat of Sr-feldspar *Chernyshova, 1991.*

At 1000°C sinterings the thermal diffusivity increased to a maximum of 0.50 mm^2/s at room temperature for the 70% theoretical maximum waste loading. For this case the lower loading had a higher thermal diffusivity than the higher loading. Specific heat was higher for the lower loading but the difference was relatively small with 0.83 J/g·K for a 70 % loading and 0.77 J/g·K at the 90% loading, both values coincide well with the specific heat of Sr-feldspar (Figure 5.11). The specific heat of the loaded bentonite was higher for samples with lower waste concentrations at each temperature tested (Figures 5.9, 5.10, and 5.11). Overall thermal diffusivity increased with sintering temperature. As thermal diffusivity increases, the ceramic can

change temperature more quickly, thus improving thermal conductivity. Sintering at 700 and 800°C higher waste loading resulted in higher thermal diffusivities (Figures 5.9 and 5.10). Sintering at 1000°C the thermal diffusivity for the lower loading was higher than the theoretical maximum loading (Figure 5.11).

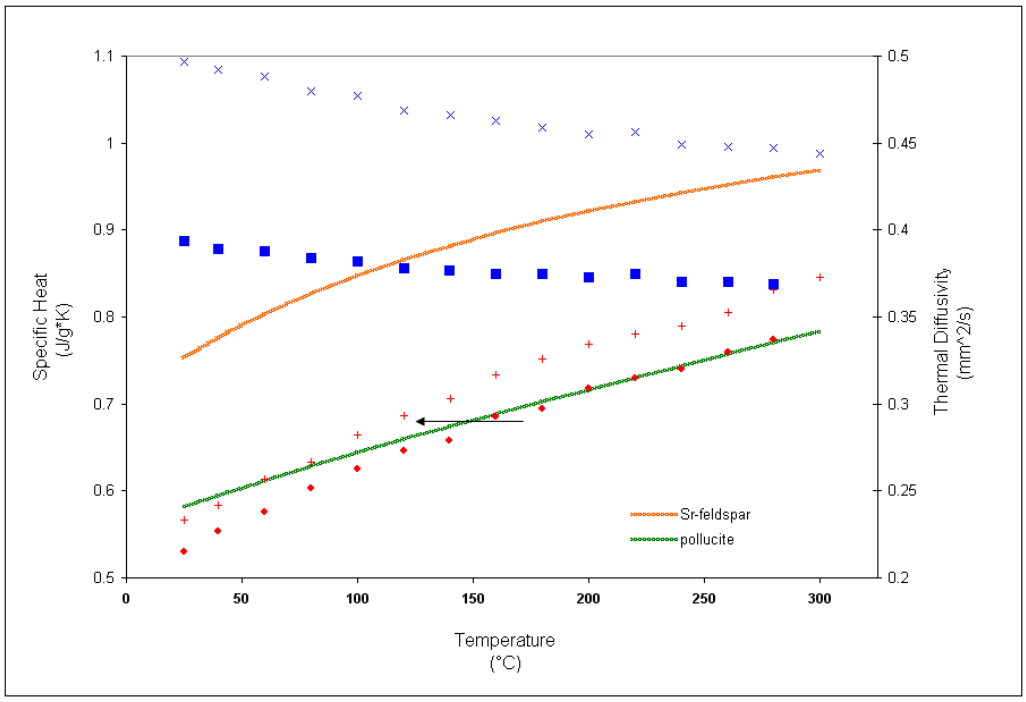

Fig. 5.11. Thermal properties of 1000°C sintered bentonite. × refers to thermal diffusivity of 70% loaded bentonite; and ▪ refers to the thermal diffusivity of 100% loaded bentonite; + refers to the specific heat of 70% loaded bentonite; • refers to the specific heat of 100% loaded bentonite; green line is the specific heat of pollucite *Ogorodova, 2003*; and the orange line is the specific heat of Sr-feldspar *Chernyshova, 1991.*

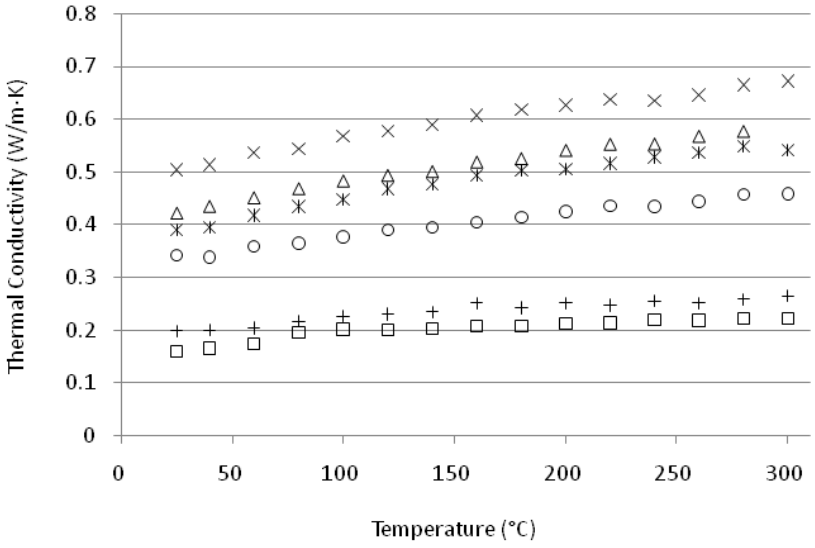

Fig. 5.12. Thermal conductivity of sintered bentonite loaded with ions. + refers to 70% loaded bentonite sintered at 700°C; □ refers to 100% loaded bentonite also sintered at 700°C; ⋆ refers to 70% loaded bentonite sintered at 800°C; ∘ refers to 100% loaded bentonite sintered at 800°C; × refers to 70% loaded bentonite sintered at 1000°C; and ▽ refers to 100% loaded bentonite sintered at 1000°C. Measured in air.

Thermal conductivity was calculated from the bulk density (Figure 5.1), thermal diffusivity, and specific heat (measured in air). The higher sintering temperatures resulted in higher thermal conductivities and the lower waste loadings had higher thermal conductivities at each sintering temperature. The highest thermal conductivity was for 70% theoretical maximum loaded bentonite, or 26 mass percent waste ions sintered at 1000°C at 0.68 W/m·K at 275°C (Figure 5.12).

When compared to porosity data, the lower thermal conductivities for the higher loadings coincide with the higher porosity in these samples.

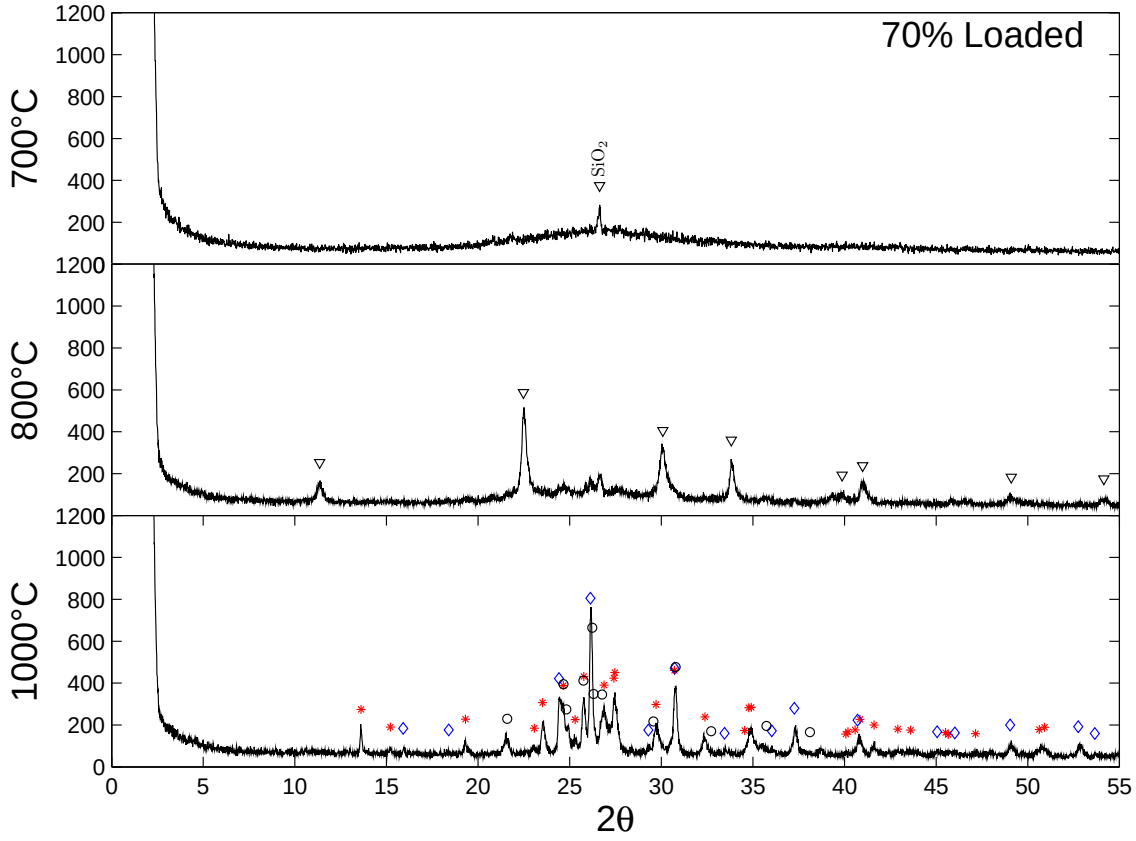

Fig. 5.13. XRD of 70% theoretical waste loaded bentonite. ▽ barium aluminum silicate $Ba(Al_2Si_2Si_2O_8)$ PDF 1-088-1048; ◊ refers to cesium aluminum silicate (pollucite) $CsAlSiO_4$ PDF 47-0471; ∗ refers to barium strontium aluminum silicate $Ba_{0.5}Sr_{0.5}Al_2Si_2O_8$ PDF 38-1452; ∘ cesium aluminum silicate $Cs_4Al_4Si_{20}O_{48}$ PDF 41-0569.

Bentonite clay loaded with ions to 70% of the theoretical maximum, approximately 25 mass percent waste, sintered at 700°C displayed an amorphous hump, and a low intensity peak due to quartz which is present in bentonite as an impurity (top of Figure 5.13). The quartz peak at 26.6 2θ (Figure A.11) remains as crystals up

to 10μm unitl 1000°C sinterings (Figures 5.27, 5.28). ty XRD peak is visible up to 800°C (5.13, 5.14).

As the sintering temperature was increased to 800°C a barium aluminosilicate structure appears, $Ba(Al_2Si_2Si_2O_8)$. At the 1000°C three phases become apparent; cesium aluminum silicate (pollucite) $CsAlSiO_4$, a 50:50 barium strontium aluminum silicate $Ba_{0.5}Sr_{0.5}Al_2Si_2O_8$, and a high silica content cesium aluminum silicate $Cs_4Al_4Si_{20}O_{48}$.

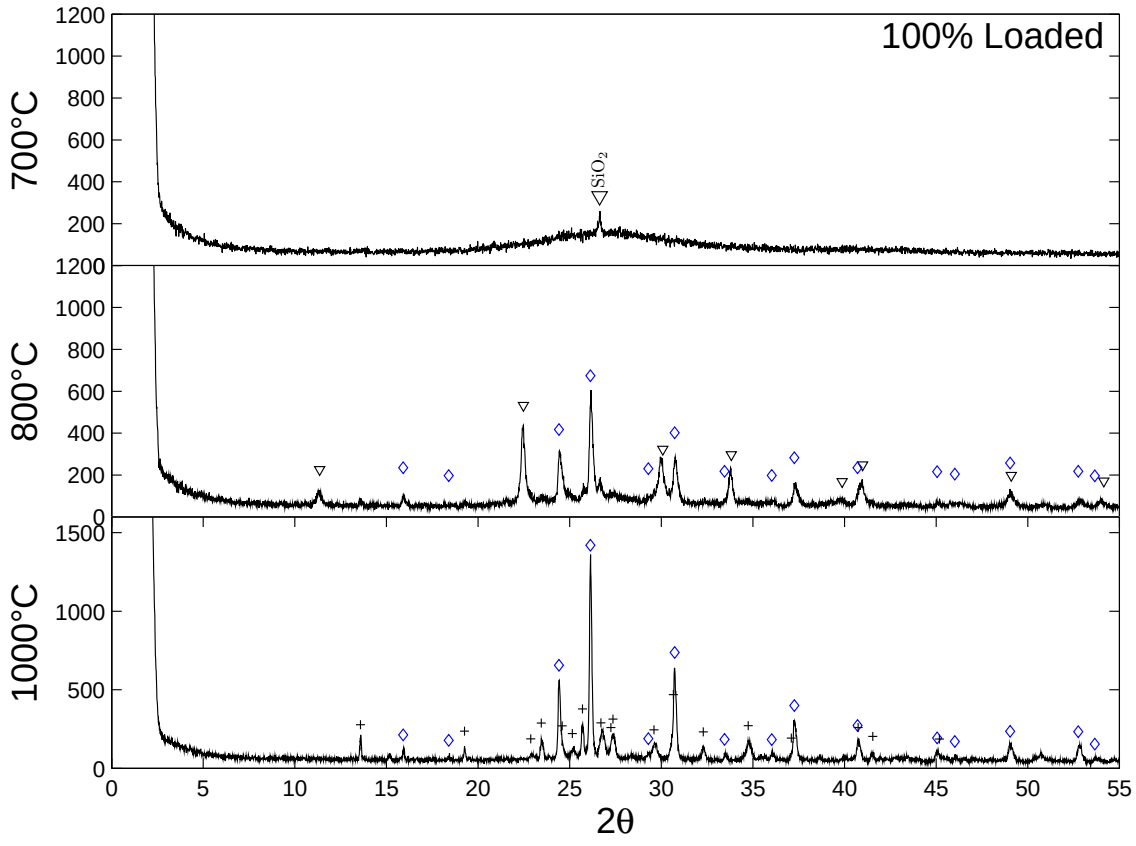

Fig. 5.14. XRD of 100% theoretical waste loaded bentonite. ▽ barium aluminum silicate $Ba(Al_2Si_2O_8)$ PDF 1-088-1048; ◊ refers to cesium aluminum silicate (pollucite) $CsAlSiO_4$ PDF 47-0471; + refers to barium strontium aluminum silicate $Ba_{.75}Sr_{.25}Al_2Si_2O_8$ PDF 38-1451.

At approximately 32 mass percent waste ions, or 100% loaded bentonite the 700°C sintering resulted in the a very similar situation observed with the lower loading, only a quartz peak and a amorphous hump was visible in the XRD scan. Sintering at 800°C also displays the same barium alumino silicate as before $Ba(Al_2Si_2O_8)$, but also pollucite appears, cesium aluminum silicate $CsAlSiO_4$. At 1000°C we see two phases. These are pollucite $CsAlSiO_4$ and a 75:25 barium strontium aluminosilicate $Ba_{.75}Sr_{.25}Al_2Si_2O_8$ (Figure 5.14).

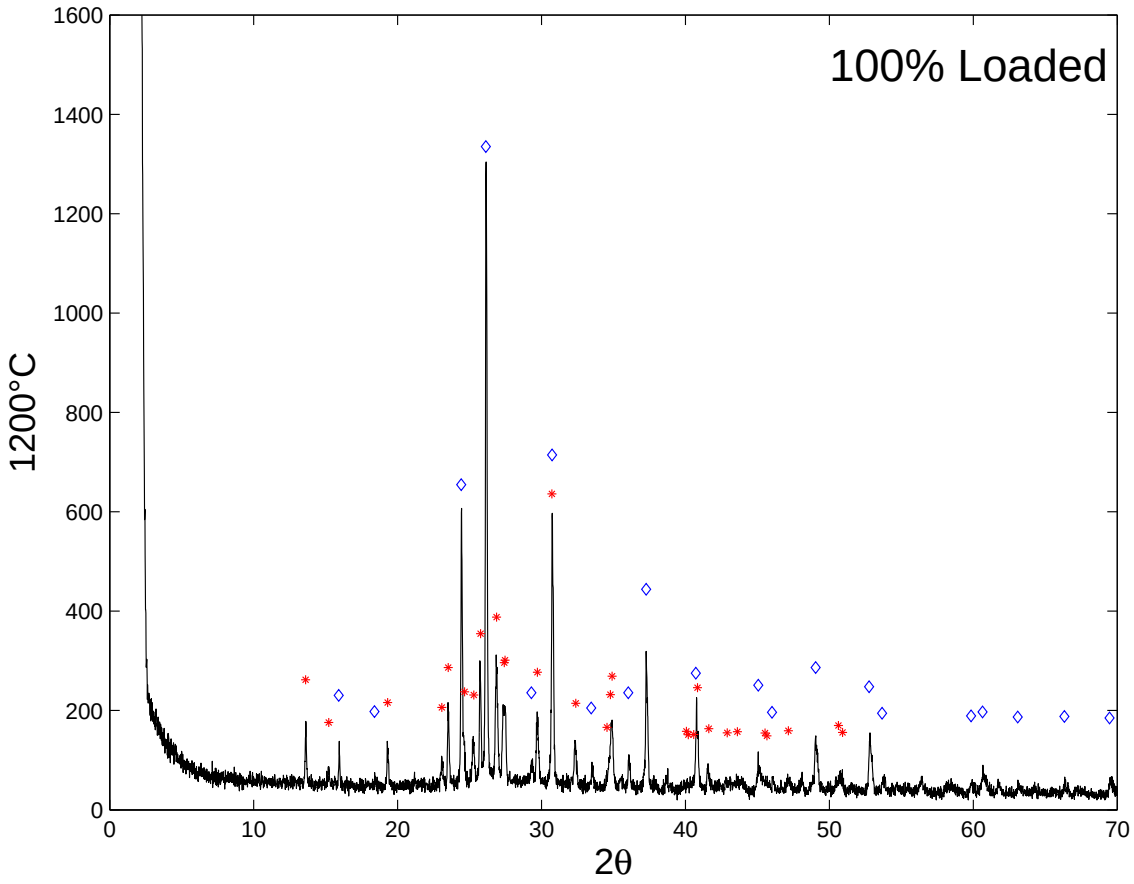

Fig. 5.15. XRD of 100% theoretical waste loaded bentonite sintered at 1200°C. ◊ refers to cesium aluminum silicate (pollucite) $CsAlSiO_4$ PDF 47-0471; * refers to barium strontium aluminum silicate $Ba_{0.5}Sr_{0.5}Al_2Si_2O_8$ PDF 38-1452.

Sintering the maximum loading at 1200°C resulted in two apparent phases. The pollucite is still prominent and displays very sharp high peaks, the other is the 50:50 barium aluminosilicate Figure 5.15.

5.5 Scanning Electron Microscopy and Wave Dispersive Spectroscopy

Samples sintered at 700, 800, 1000, 1100, and 1200°C were analyzed and elemental maps were produced. In addition to the elemental maps backscattered electron images of the selected areas were also created to reference the location and topography of the mapped areas. The elemental map images are gray scale where lighter areas refer to higher concentrations of a particular element. The concentrations are not transferable from image to image or element to element. The overall concentration of each component was determined with neutron activation analysis, and most images are only qualitative. Quantitative analysis was reserved for the sample sintered 1200°C. The relative intensity of the signal is only relevant within each individual image. For clarity contrast and brightness may have been modified. Bright white areas are only a local high concentrations and should not be considered absolute maximums, or that no other elements are present. The location of each of the mappings was chosen primarily for its lack of porosity, to focus on the mineral phases present, flat areas were chosen over cracks and voids.

The lowest sintering temperature of 700°C produced a very course texture. Strontium in the higher loading appears to be concentrated in small areas, and the cesium in the lower loading is concentrated in some regions more than others. But overall the four elements Cs, Sr, Ba, and Rb are distributed homogeneously (Figures 5.16, 5.17). The central dark region in the lower loading (70% theoretical) is void of the four elements in this figure is probably quartz that has not dissolved during sintering. The region has a high silicon concentration (Appendix D).

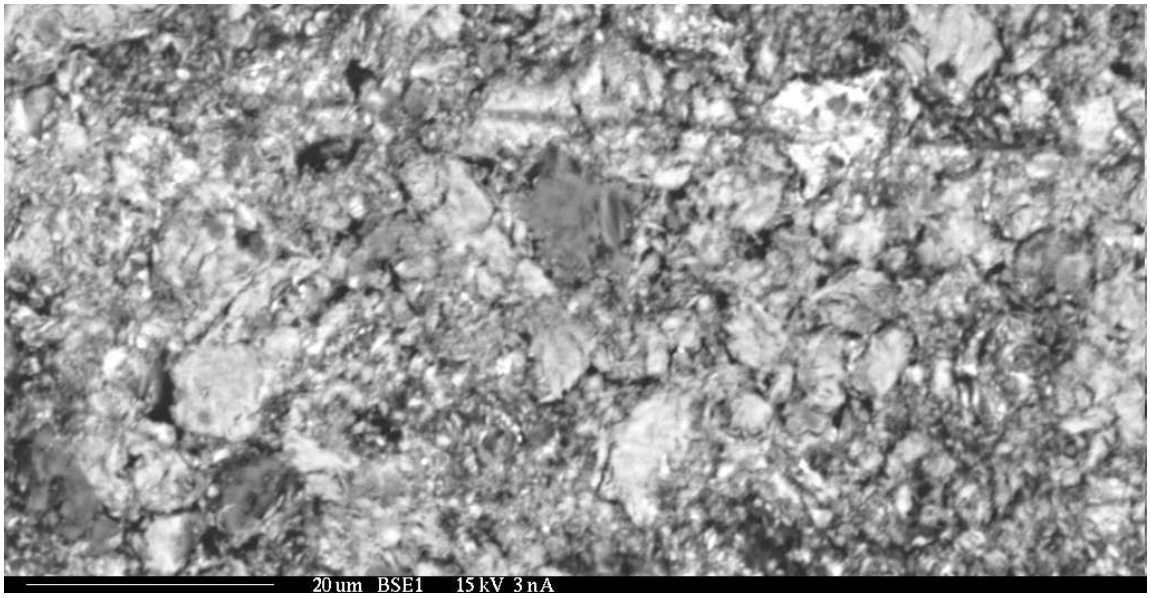

(a) Backscattered image at 1000X of 700°C sintered bentonite 25% waste metals

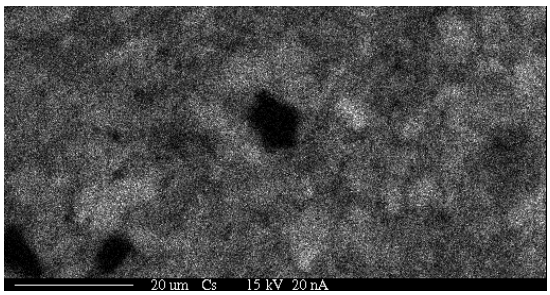

(b) Cs relative concentration

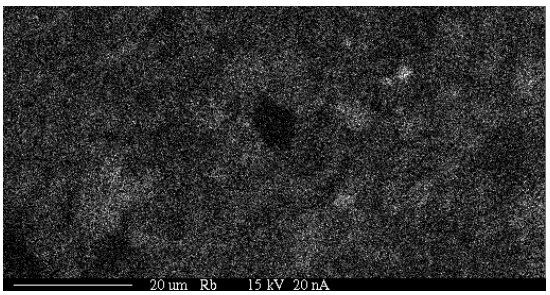

(c) Rb relative concentration

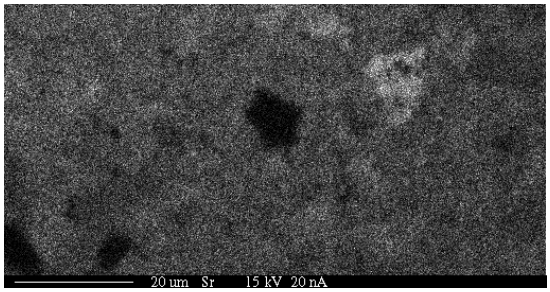

(d) Sr relative concentration

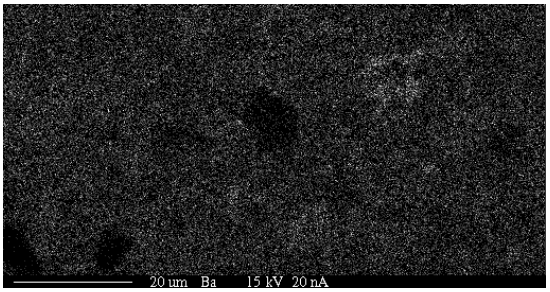

(e) Ba relative concentration

Fig. 5.16. BSE, and WDS of 700°C sintered bentonite, 25 mass pct. waste ions. Backscattered image (top) and element maps where light areas refer to higher concentration (bottom).

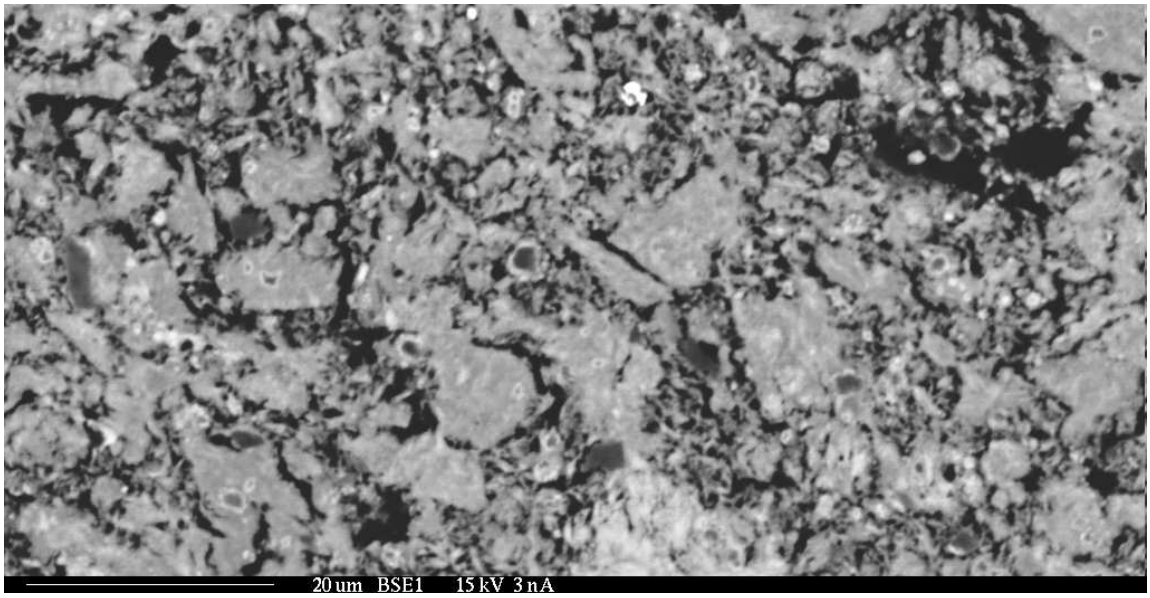

(a) Backscattered image at 1000X of 700°C sintered bentonite 32% waste metals

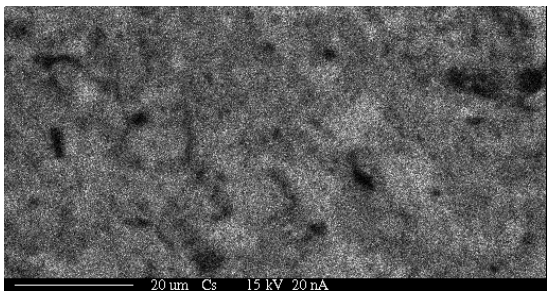

(b) Cs relative concentration

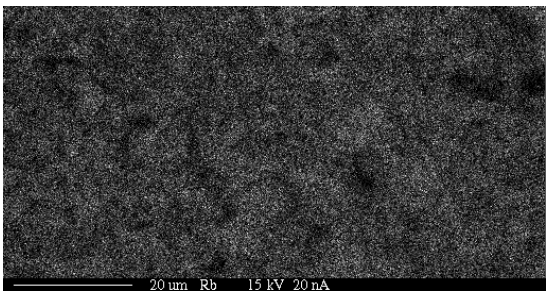

(c) Rb relative concentration

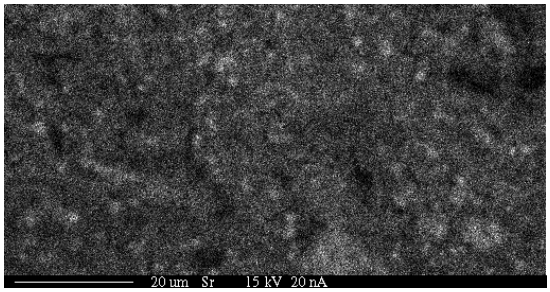

(d) Sr relative concentration

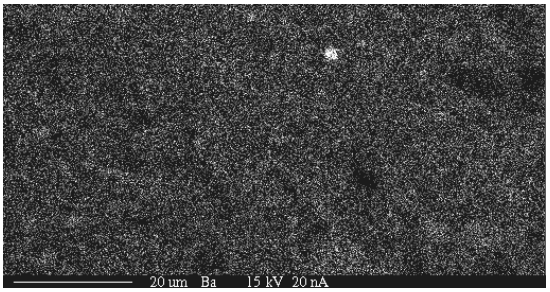

(e) Ba relative concentration

Fig. 5.17. BSE and WDS of 700°C sintered bentonite, 32 mass pct. waste ions. Backscattered image (top) and element maps where light areas refer to higher concentration (bottom).

At 800°C sintering the surfaces are smoother, with larger continuous flat areas. The elements cesium and strontium have areas of high concentration similar to the 700°C sintering. Rubidium and barium in the higher waste loaded bentonite also display small regions of high concentration (Figures 5.18, 5.19).

In bentonite sintered at 1000°C and loaded to 70% of the theoretical maximum (~26 mass percent) the waste ions are distributed in a similar manner to the 800°C sinterings, with areas of higher concentration (Figure 5.20). Bentonite loaded to 100% (~31 mass percent) at 1000°C displays a transition from lower temperature sinterings, and the 70% loading (Figure 5.21). Up to this point the surfaces have been rough and porous. In the backscattered image of the 1000°C 100%loading three distinct regions are visible, a very rough dark area, and a flat region with bright spots and a slightly darker grey area. Within the elemental maps a very clear segregation is evident. The cesium and strontium have become concentrated in much smaller areas within the sample, and the barium and rubidium also have become concentrated to separate regions in the sample. The cesium and rubidium are occuping the same areas, while the barium is in the opposing regions. The strontium has become very concentrated in isolated small spots. The silicon has become homogenously distributed, and no longer in small high concentration clumps (Appendix D).

The backscattered image of bentonite sintered at 1100°C shows are very large flat area with interdispersed dark holes. Within the flat area three different regions are visible. There is a grey matrix that encompasses two brighter phases, a very bright region and a light grey area. The elemental maps show that the bright area is high in cesium as well as rubidium. The grey area is rich in barium and strontium (Figure 5.22).

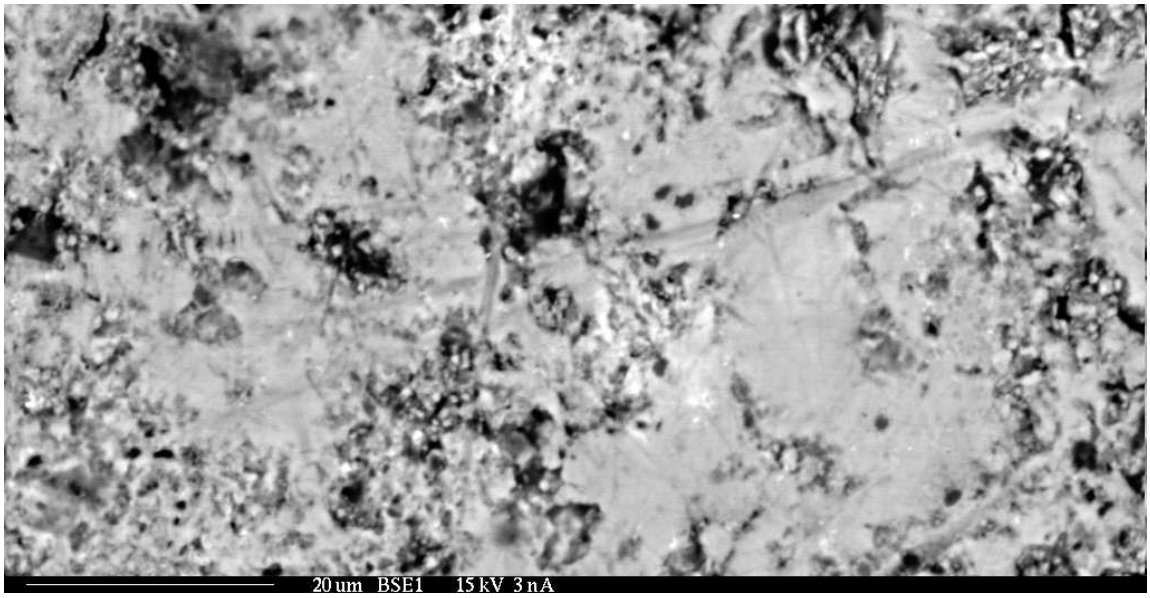

(a) Backscattered image at 1000X of 800°C sintered bentonite 24% waste metals

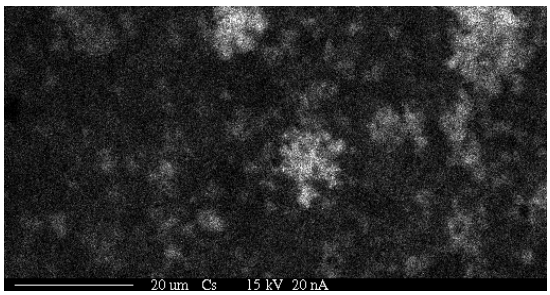

(b) Cs relative concentration

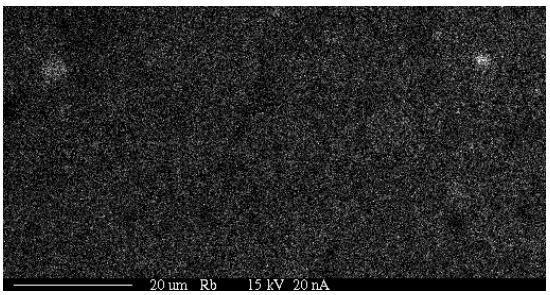

(c) Rb relative concentration

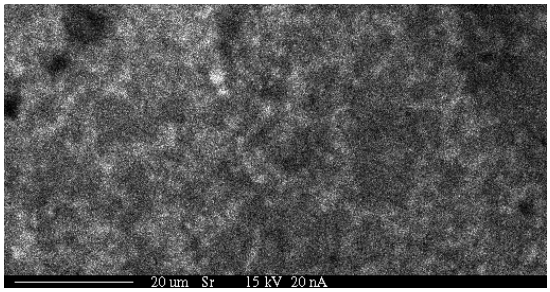

(d) Sr relative concentration

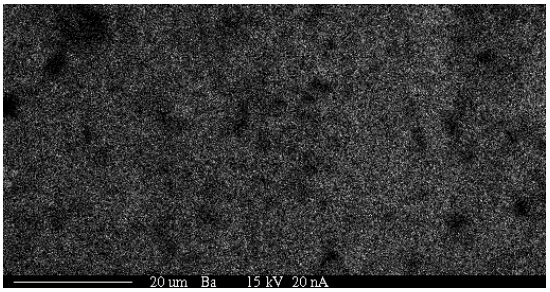

(e) Ba relative concentration

Fig. 5.18. BSE and WDS of 800°C sintered bentonite, 24 mass pct. waste ions. Backscattered image (top) and element maps where light areas refer to higher concentration (bottom).

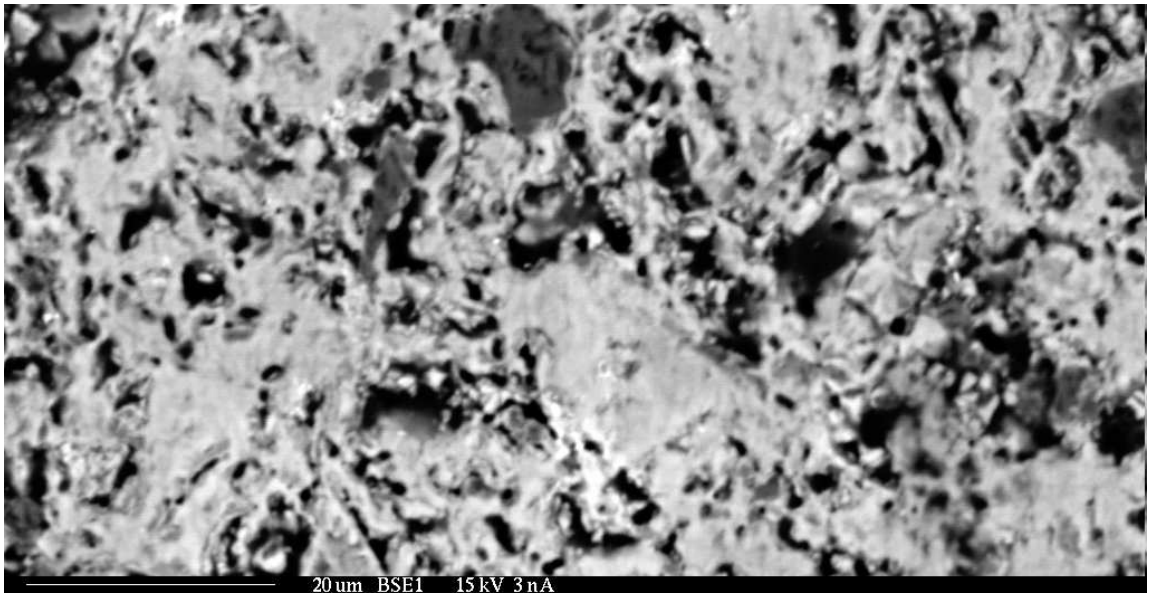

(a) Backscattered image at 1000X of 800°C sintered bentonite 32% waste metals

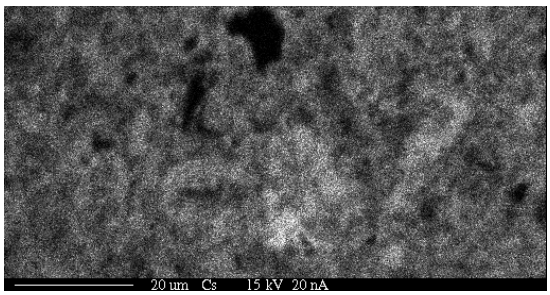

(b) Cs relative concentration

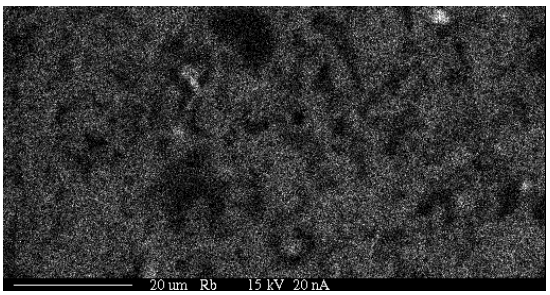

(c) Rb relative concentration

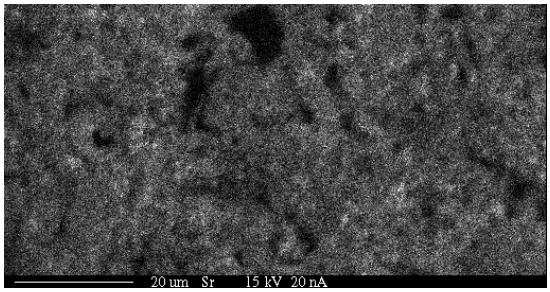

(d) Sr relative concentration

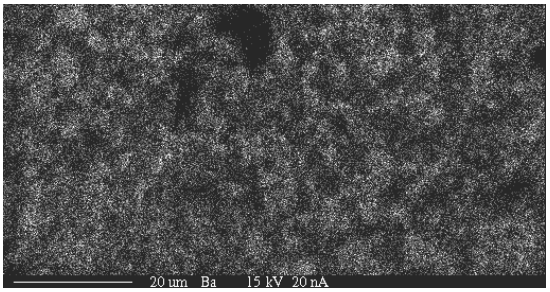

(e) Ba relative concentration

Fig. 5.19. BSE and WDS of 800°C sintered bentonite, 32 mass pct. waste ions. Backscattered image (top) and element maps where light areas refer to higher concentration (bottom).

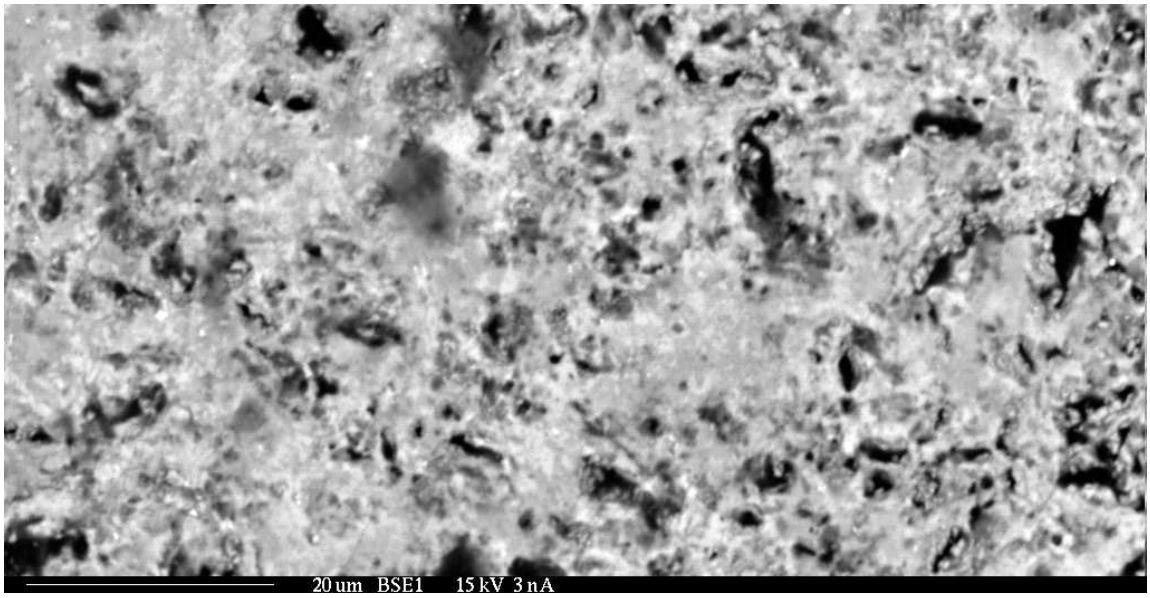

(a) Backscattered image at 1000X of 1000°C sintered bentonite 26% waste metals

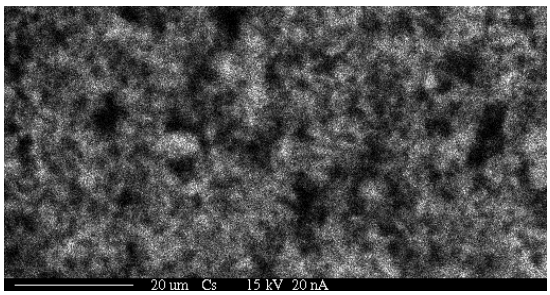

(b) Cs relative concentration

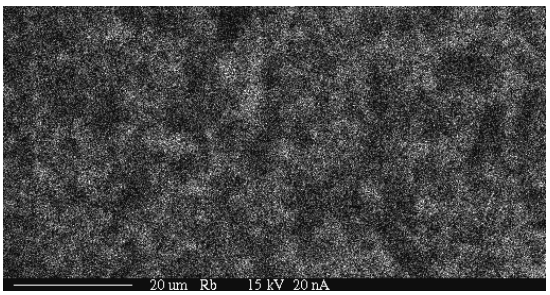

(c) Rb relative concentration

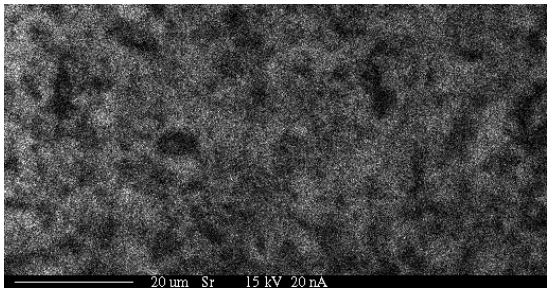

(d) Sr relative concentration

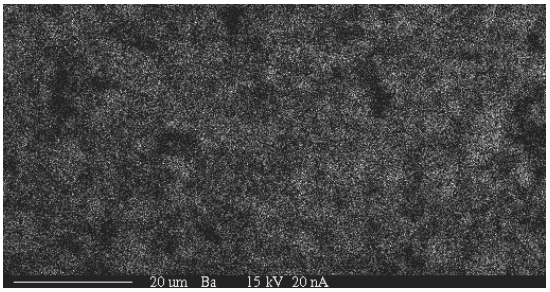

(e) Ba relative concentration

Fig. 5.20. BSE and WDS of 1000°C sintered bentonite, 26 mass pct. waste ions. Backscattered image (top) and element maps where light areas refer to higher concentration (bottom).

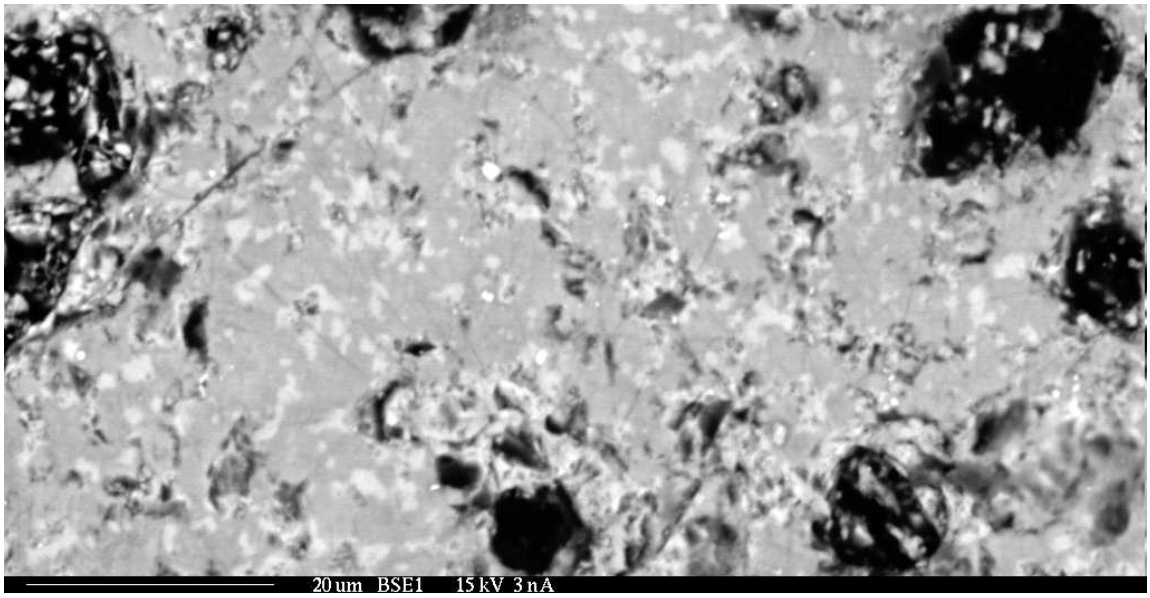

(a) Backscattered image at 1000X of 1000°C sintered bentonite 31% waste metals

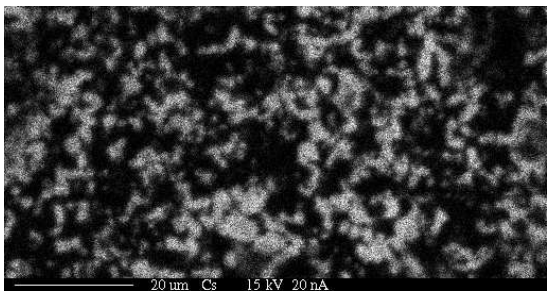

(b) Cs relative concentration

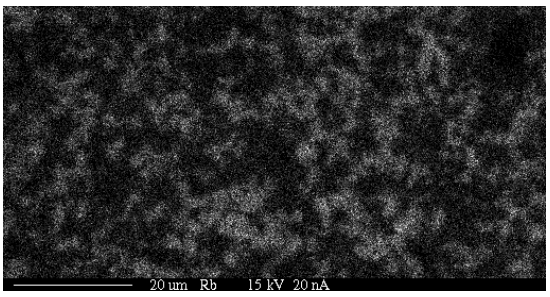

(c) Rb relative concentration

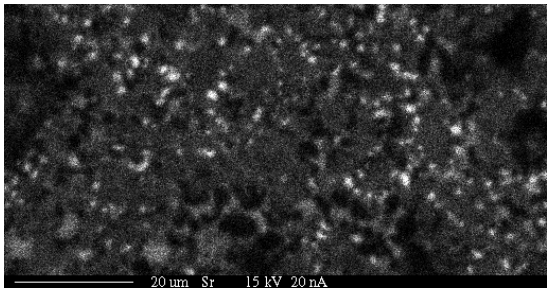

(d) Sr relative concentration

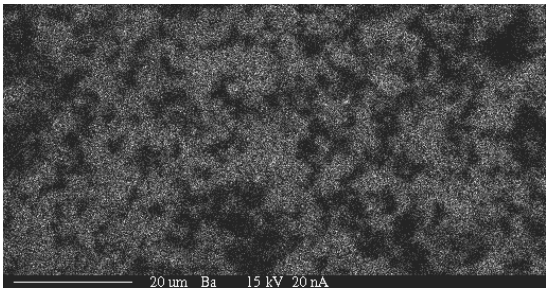

(e) Ba relative concentration

Fig. 5.21. BSE and WDS of 1000°C sintered bentonite, 31 mass pct. waste ions. Backscattered image (top) and element maps where light areas refer to higher concentration (bottom).

Sintering at 1200°C resulted in a very drastic development visible in the backscattered image. Crystals are visible throughout the sample. Two distinct types of crystals easily noticeable, light areas (representative of larger atomic mass) with crystals of indeterminant structure, and long rectangular grey crystals. Both crystals are embedded in a dark phase. The rectangular crystals are indicative of celsian, or barium feldspar [92] appear in small groups of micrometer to submicrometer size, as well as crystals over 10 μm long but less than 1μm wide. The light crystals tend to be larger with width to length ratios much closer to unity (Figure 5.23). This sample was re-analyzed with spectroscopy focused on quantification in specific regions, and added a wider spectrum of elements.

At 1200°C the appearance of crystals motivated a quantitative analysis. The three regions visible were samples for analysis. In addition to the cesium, strontium, rubidium and barium, the elements aluminum, calcium, silicon, iron, magnesium, and sodium were included in the analysis.

The grey lath crystal phase had slightly higher levels of barium than the rest of sample, the dark region is higher in strontium (Figure 5.24). The needles have the highest levels of aluminum, and lower levels of silicon and calcium than the surrounding dark phase (Figure 5.25).

Elemental maps show a progressive segregation of the cesium and rubidium from the strontium and barium. As the sintering temperature is increased the back scattered image transitions from coarse nondescript texture to one with three distinct regions. Very little difference is visible between the samples until 1000°C where the 26 mass percent sample appears similar to the lower sintering temperatures, but at 31 mass percent waste ions the elemental segregation and phase definition starts to appear. This trend continues as the sintering temperatures were increased.

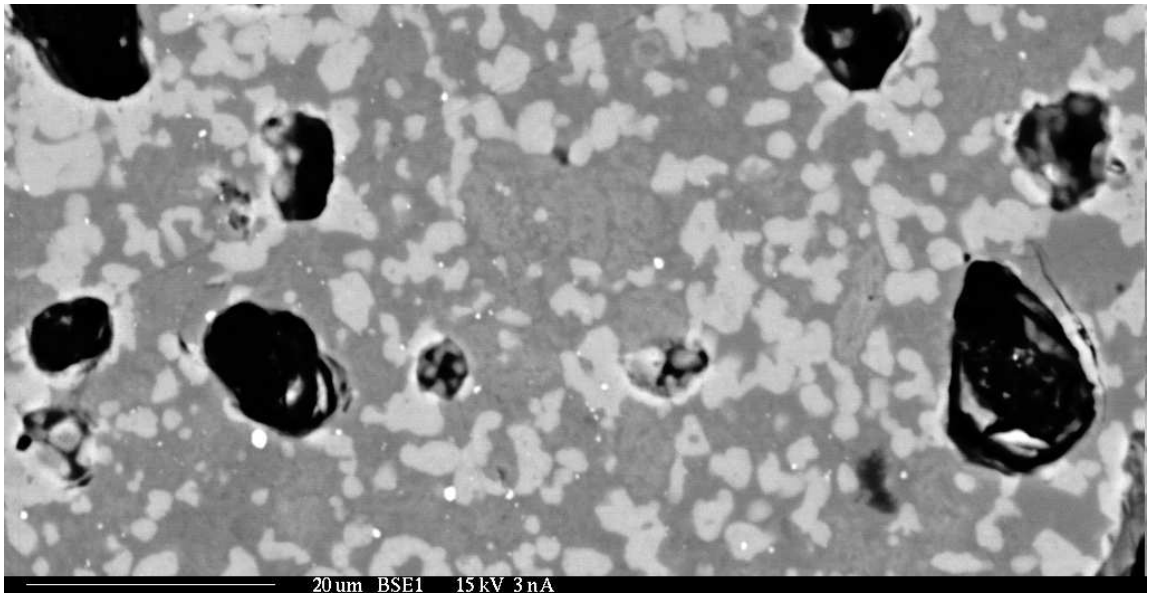

(a) Backscattered image at 1000X of 1100°C sintered bentonite 30% waste metals

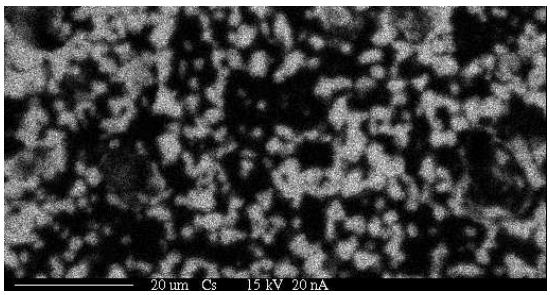

(b) Cs relative concentration

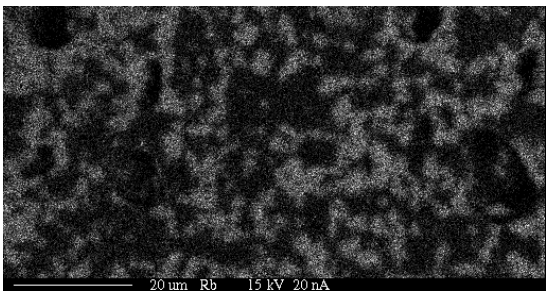

(c) Rb relative concentration

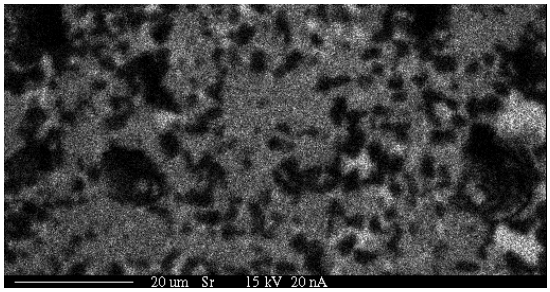

(d) Sr relative concentration

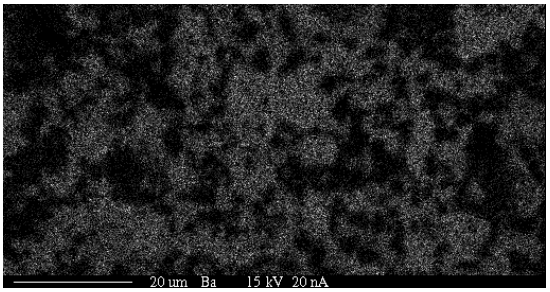

(e) Ba relative concentration

Fig. 5.22. BSE and WDS of 1100°C sintered bentonite, 30 mass pct. waste ions. Backscattered image (top) and element maps where light areas refer to higher concentration (bottom).

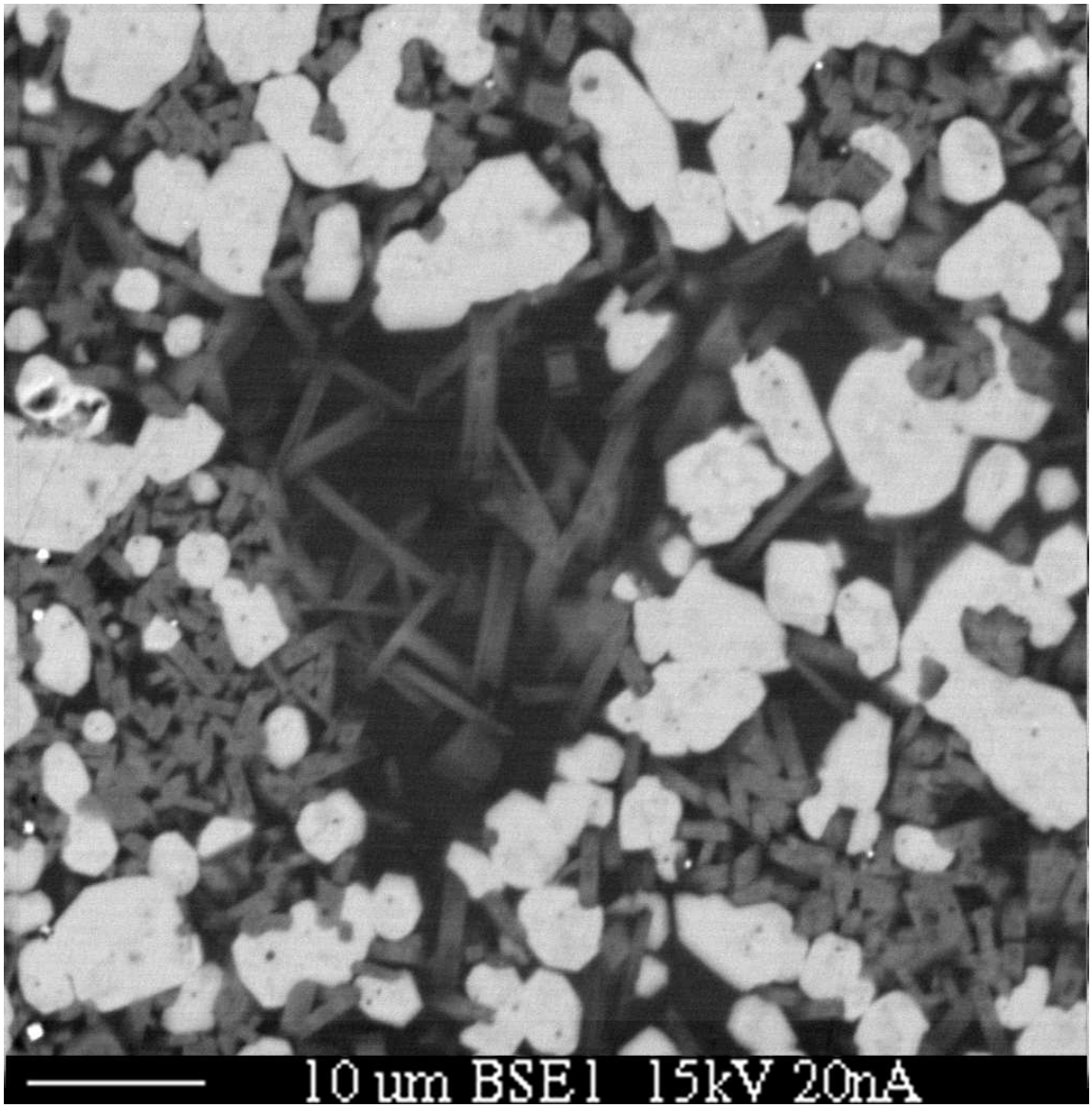

Fig. 5.23. BSE 1500X of 1200°C sintered 100% loaded bentonite. Needle shape crystals consistent with Barium/Strontium-alumino silicates celsian.

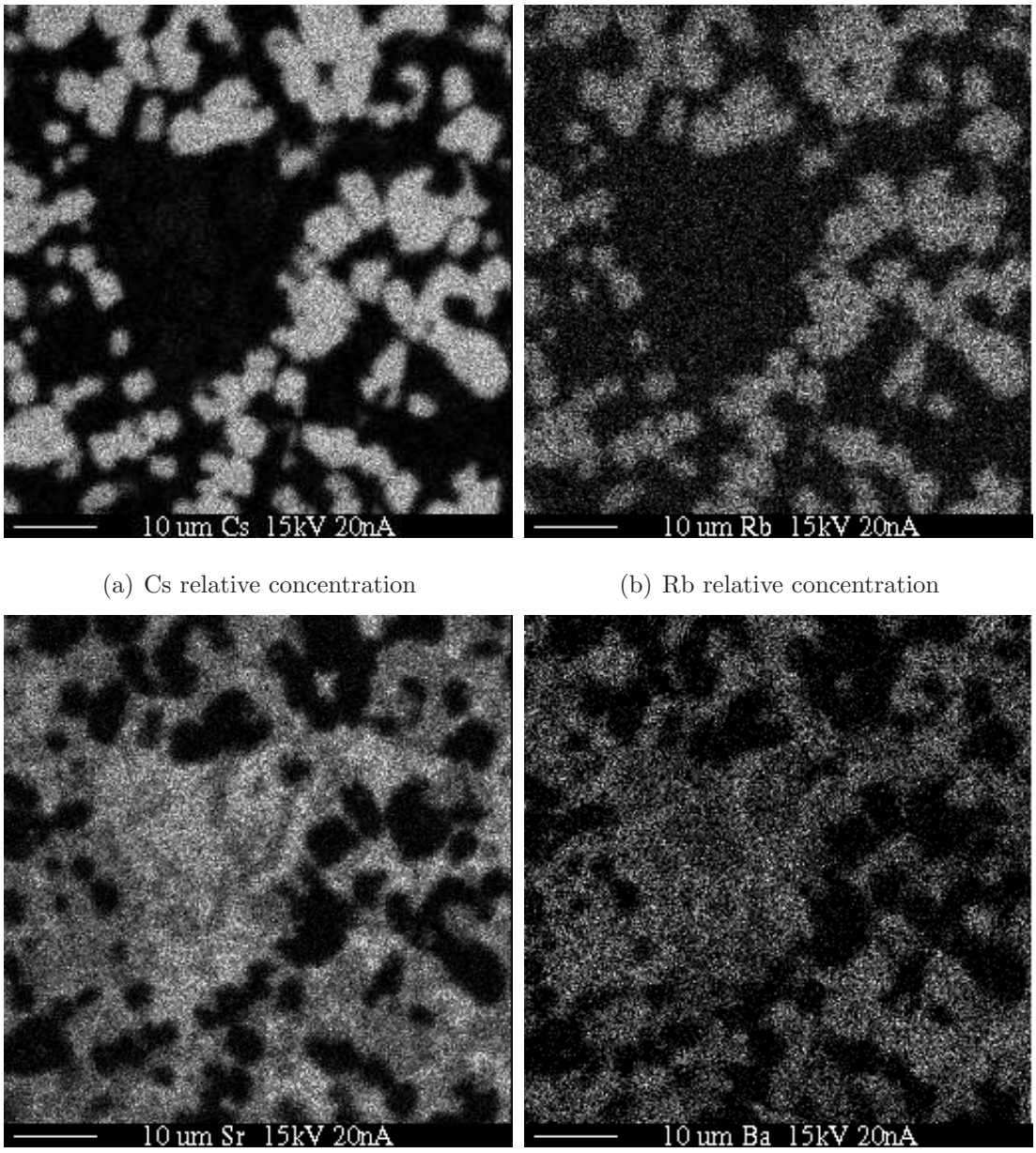

(a) Cs relative concentration

(b) Rb relative concentration

(c) Sr relative concentration

(d) Ba relative concentration

Fig. 5.24. BSE and WDS of 1200°C sintered bentonite, 30 mass pct. waste ions. Backscattered image (top) and element maps where light areas refer to high concentration (bottom).

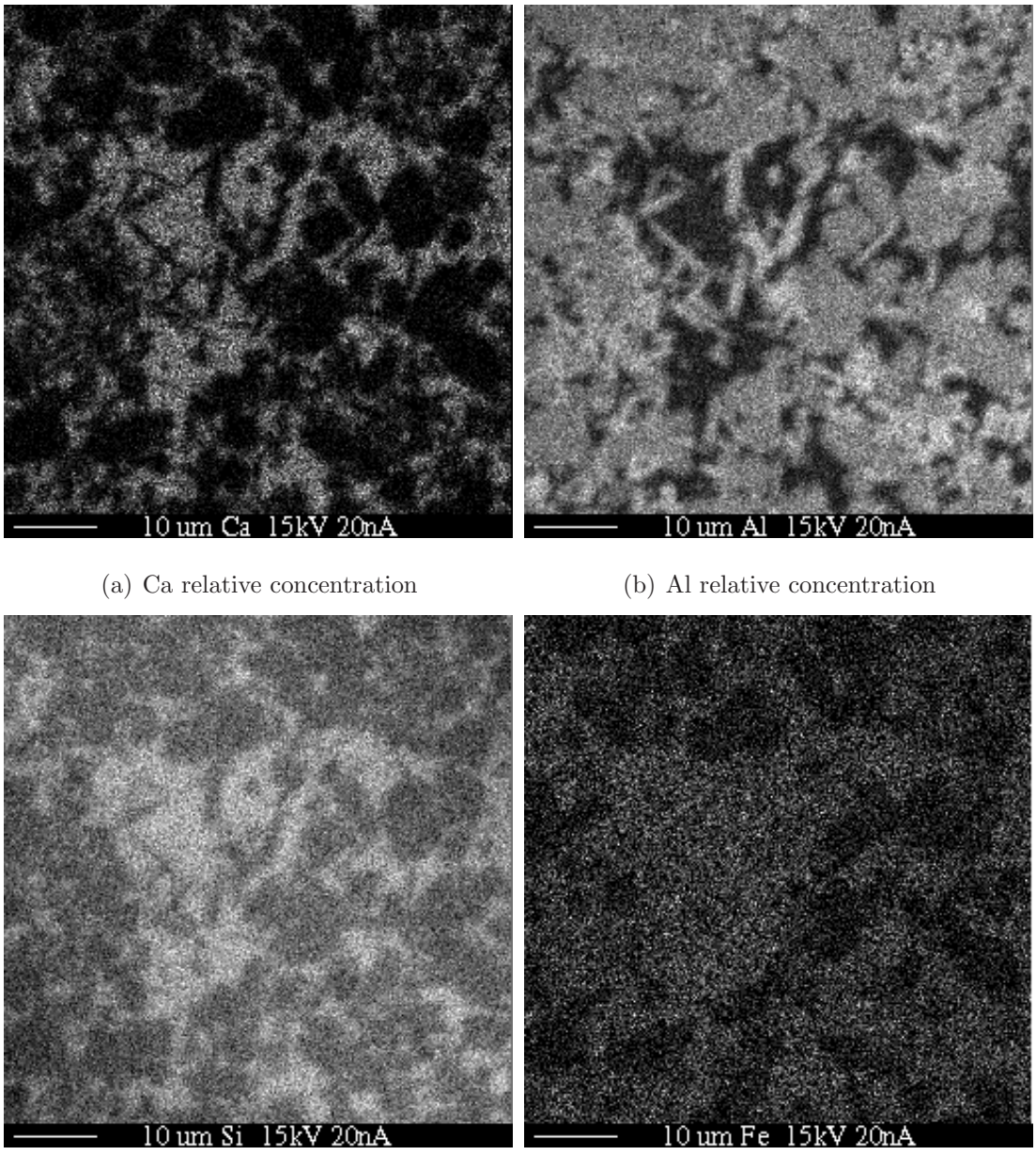

(a) Ca relative concentration

(b) Al relative concentration

(c) Si relative concentration

(d) Fe relative concentration

Fig. 5.25. BSE and WDS of 1200°C sintered bentonite, 30 mass pct. waste ions. Backscattered image (top) and element maps where light areas refer to high concentration (bottom).

The brightest areas have high cesium and rubidium concentrations, and low to undetectable levels of strontium and barium, low levels of iron, magnesium, and sodium, and moderate concentrations of aluminum and silicon. The dark regions hold barium, the highest levels of strontium, calcium, silicon, sodium, magnesium, and iron (Figures 5.24, 5.25). Points were selected for quantitative elemental analysis by x-ray counting (5.26).

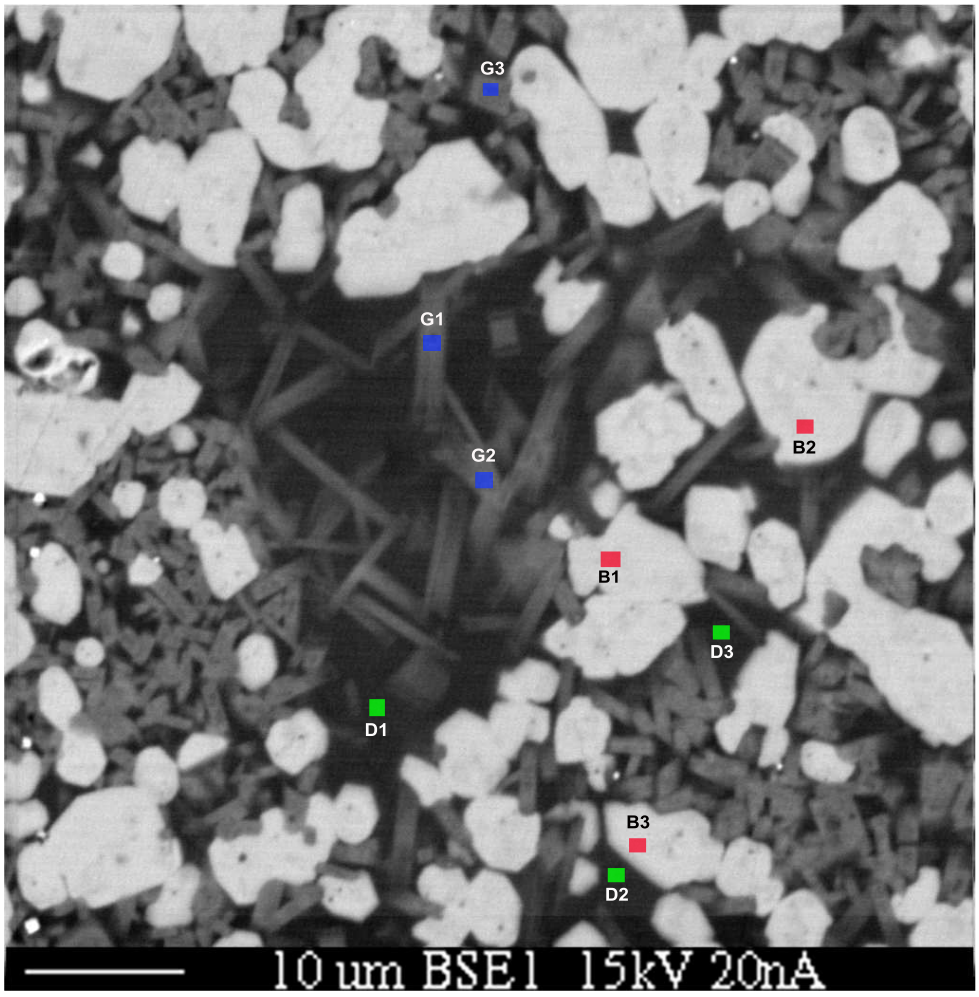

Fig. 5.26. Points selected for quantitative analysis in 1200°C sintered bentonite. ■ bright areas; ■ gray areas; ■ dark areas.

Table 5.3

Elemental concentrations of selected points in 1200°C sintered bentonite.

Location	Cs	Sr	Ba	Rb	Al	Ca	Si	Fe	Mg	Na	O	Total (atom %)
Dark 1	0.44	2.87	2.14	0.20	2.79	1.74	22.43	1.32	2.83	1.98	61.26	99.999
Dark 2	0.38	2.81	2.18	0.18	3.05	1.68	22.31	1.28	2.78	2.12	61.25	99.999
Dark 3	0.38	2.87	2.28	0.18	3.12	1.67	22.13	1.30	2.81	2.08	61.18	99.999
Bright 1	7.40	0.00	0.17	1.82	9.07	0.01	20.52	0.51	0.05	0.31	60.14	100.001
Bright 2	7.58	0.00	0.15	1.79	9.18	0.02	20.35	0.49	0.08	0.33	60.05	100
Bright 3	7.36	0.06	0.22	1.77	9.24	0.03	20.32	0.51	0.07	0.33	60.10	99.999
Grey 1	0.11	1.67	4.13	0.24	10.02	0.20	18.71	1.00	0.93	1.62	61.37	100.001
Grey 2	0.12	1.67	4.41	0.21	10.62	0.18	18.24	0.99	0.85	1.37	61.35	99.999
Grey 3	0.15	1.67	4.18	0.25	10.09	0.21	18.65	0.91	0.98	1.53	61.37	100

Detection limits and basis oxides in APPENDIX B.

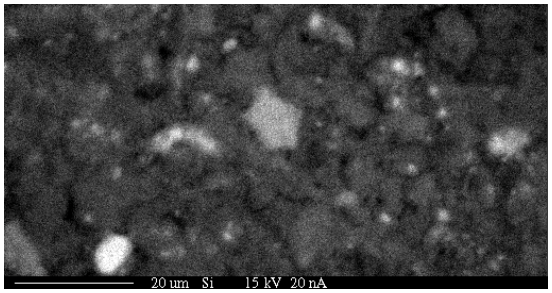

(a) Si concentration in 70% loaded bentonite 700°C

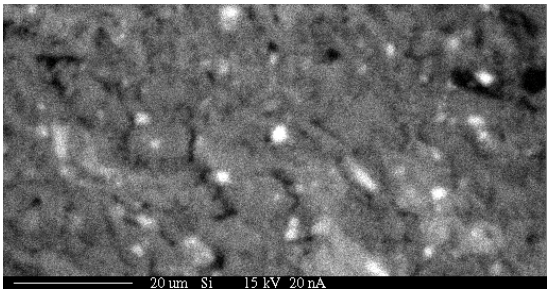

(b) Si concentration in 100% loaded bentonite 700°C

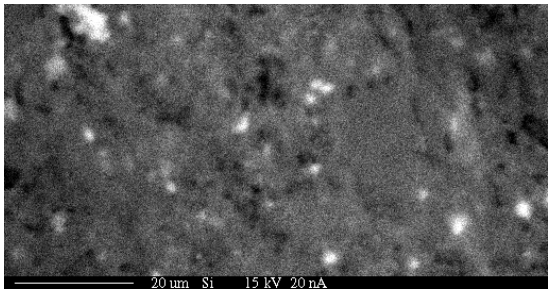

(c) Si concentration in 70% loaded bentonite 800°C

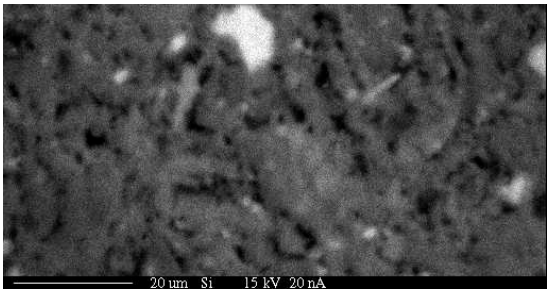

(d) Si concentration in 100% loaded bentonite 800°C

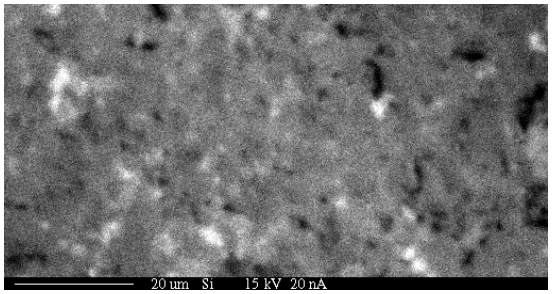

(e) Si concentration in 70% loaded bentonite 1000°C

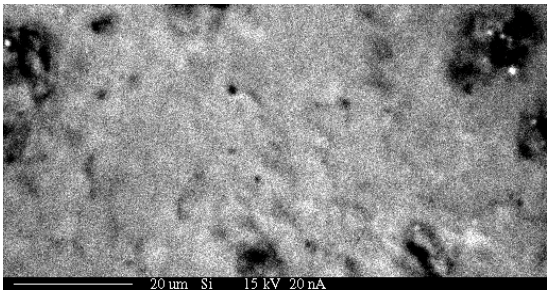

(f) Si concentration in 100% loaded bentonite 1000°C

Fig. 5.27. Silicon elemental maps, temperatures from 700-1000°C sinterings at 70% and 100% loadings. Where white refers to a local high concentration at 1000X.

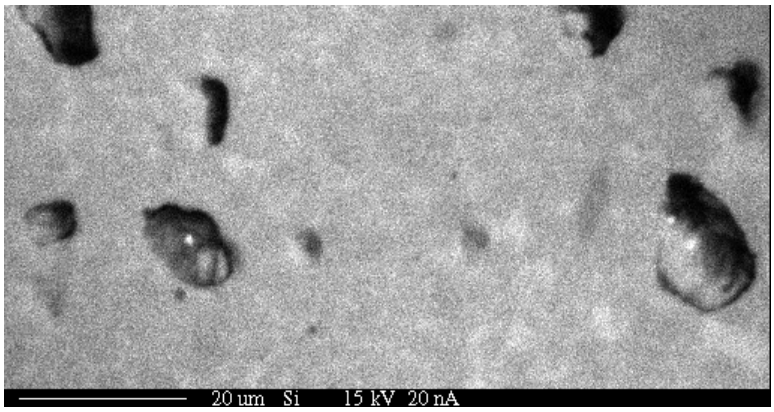

(a) Si concentration in 100% loaded bentonite 1100°C

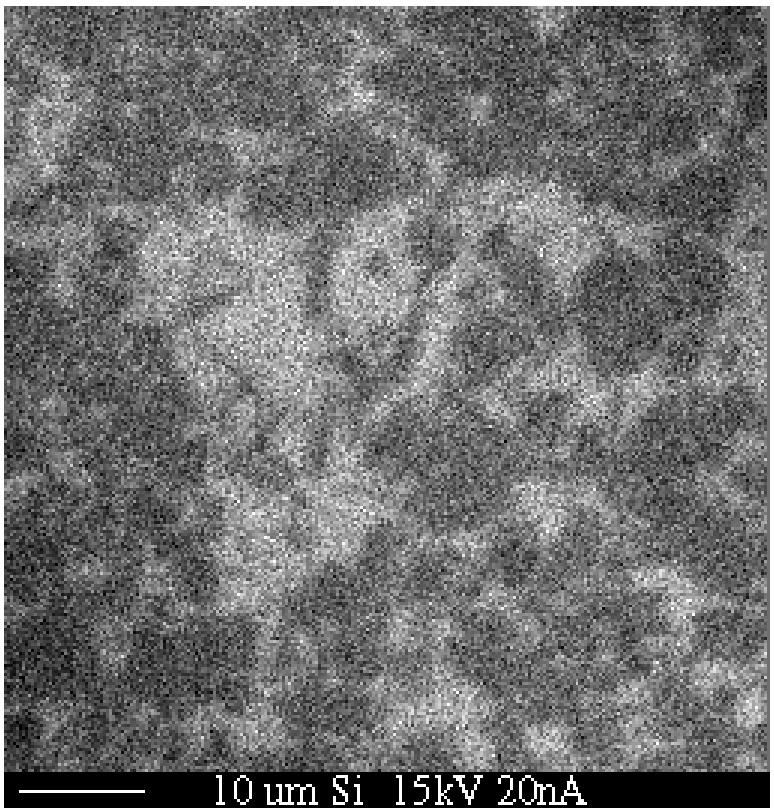

(b) Si concentration in 100% loaded bentonite 1200°C

Fig. 5.28. Silicon elemental maps of 1100 and 1200°C sinterings. Where white refers to a local high concentration at 1000X.

The results show that the needle shaped crystals are >4% barium, the highest barium concentration of all other areas. The bright areas are ~7.4% cesium and ~1.8% rudidium, both higher than the other areas. The dark area has the highest concentration of strontium and silicon, at ~2.85% and ~22.3% percent respectively as well as the highest levels of calcium, iron, magnesium, and sodium (Table 5.3). Silicon maps have been isolated to highlight the dissolution of quartz grains >1000°C (Figures 5.27,5.28)

5.6 Neutron Activation Analysis

Bentonite clay loaded with FPEX raffinate ions was analyzed with Neutron Activation Analysis (NAA). Bentonite loaded to 70% of the theoretical maximum and sintered at 700, 800, and 1000°C averaged 10.96 mass% cesium, 3.49 mass% strontium, 8.93 mass% barium, and 1.54 mass% rubidium. Bentonite clay loaded to 100 % of the theoretical mass had 13.70 mass% cesium, 4.37 mass% strontium, 11.66 mass% barium, and 2.06 mass% rubidium (Table 5.4). NAA details for each element in the bentonite sintered at 700, 800, and 1000°C at each theoretical mass concentration are in Appendix D.

Table 5.4
Mass% of element NAA all sinterings

	Average mass% across all sinterings			
Element	70% loaded	std dev	100% loaded	std dev
Cesium	10.96	0.18	13.70	0.22
Strontium	3.49	0.28	4.37	0.35
Barium	8.93	1.22	11.66	1.20
Rubidium	1.54	0.14	2.06	0.14

5.7 Toxicity Characteristic Leach Procedure

Sintered bentonite powders ≤ 150μm in size with ions of cesium, strontium, barium and rubidium were mixed with an acetic acid solution for 18 hours. The leachate was then analyzed by ICP-MS. There are numerous types of hazardous waste. One reason waste is classified as hazardous is if the barium concentration in its TCLP leachate is above 100 ppm.

Bentonite sintered at 700°C with 70 % and 100 % theoretical waste concentrations had 442 and 961 ppm barium concentrations in their leachate solutions respectively. Sintered at 800°C and loaded to 70% of the theoretical maximum passed at 34.3 ppm, but the 100% laoded bentonite failed at 172 ppm. Both loadings, 70% and 100%; passed when sintered at 1000°C with 18 and 63.1 ppm barium in the leachate respectively. 1100°C sintering resulted in very low leach rates in the 70% loaded bentonite, with the highest concentration for barium at 12.6 ppm; at the 100% loading strontium increases to 78 ppm which is just below the regulation limit. At 1200°C all element concentrations are below 10 ppm at both loadings. All ion leach rates went down as the sintering temperature was increased with the exception of strontium. Strontium leach rates were relatively high for the 100% loaded bentonite at all sintering temperatures except 1200°C Figure 5.29.

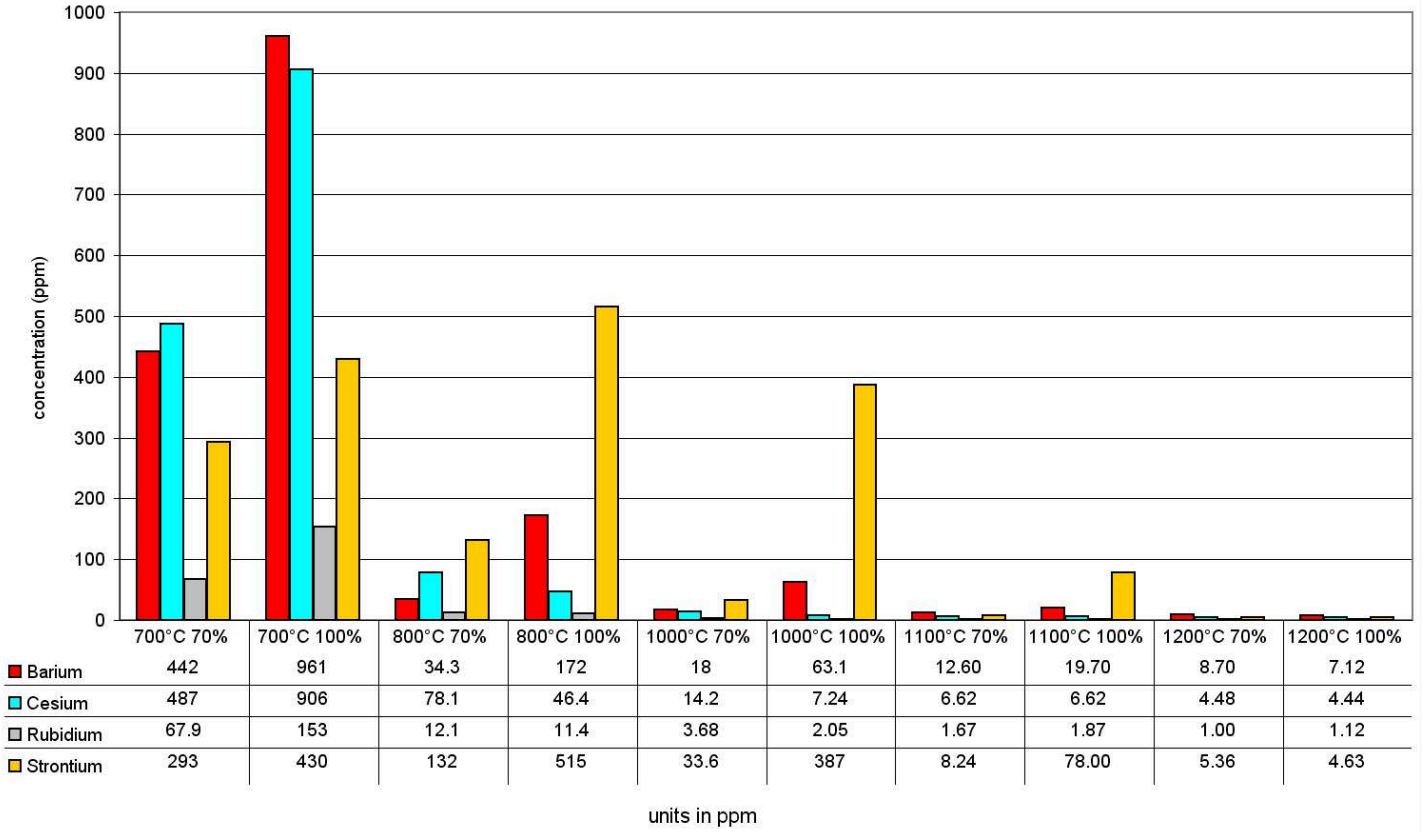

Fig. 5.29. TCLP results 700, 800, 1000, 1100 and 1200°C 70% and 100% loaded bentonite clay (ppm)

5.8 Heat Generation Model

Data collected in this study was input to the model, and compared to a borosilicate waste glass with cesium, strontium, and the lanthanides (Table 5.5). The glass was developed under the AFCI at Pacific Northwest National Laboratory [93].

Table 5.5

Glass composition

Cs Sr Lanthanide Glass (CSLN-7C)

	Measured	Target	Element %
Al2O3	18.07	17	
B2O3	10.5	10	
BaO	6.02	5.71	5.11%
CeO2	7.77	7.04	
Cs2O	5.45	5.98	5.36%
Eu2O3	0.4	0.41	
Gd2O3	0.48	0.46	
La2O3	3.58	3.59	
Nd2O3	11.34	11.86	
Pr2O3	3.26	3.28	
Rb2O	0.79	0.77	0.69%
SiO2	29.48	28	
Sm2O3	2.59	2.49	
SrO	2.09	1.98	1.77%
Y2O3	1.44	1.43	1.28%
Total	103.27	100	
Density (g/cm^3)	3.36		
T_g (°C)	719		

Our ceramic waste form center-line temperature was limited to a maximum 1053°C, based on the observed stability at 1200°C, with an additional safety factor (90%). Thermal conductivity has been shown to increase linearly with sintering temperature [82], this was used to extrapolate for the unknown thermal conductivities. An initial thermal conductivity was assumed, and input into the model. The model generated a center-line temperature and edge temperatures, the average of the two was used to extrapolate for the thermal conductivity. The new thermal conductivity was entered into the model to re-calculate the center-line and cladding temperatures. The center-line temperature for the borosilicate glass was limited to the glass transition temperature of 719°C.

Waste form diameter size was found comparable to the borosilicate glass(Table 5.6).

Table 5.6
Wasteform diameter for sintered bentonite and CSLN-7C glass

Waste form	radius (m)	Diameter (in)
70% bentonite	0.192	15.09
100% bentonite	0.169	13.31
CSLN-7C glass	0.164	12.9

burn-up=50 GWD/ton; 4.25 enrichment; 20 yr cooled

As the waste form radius is increased, the cladding surface and centerline temperatures will increase (Figure 5.30).

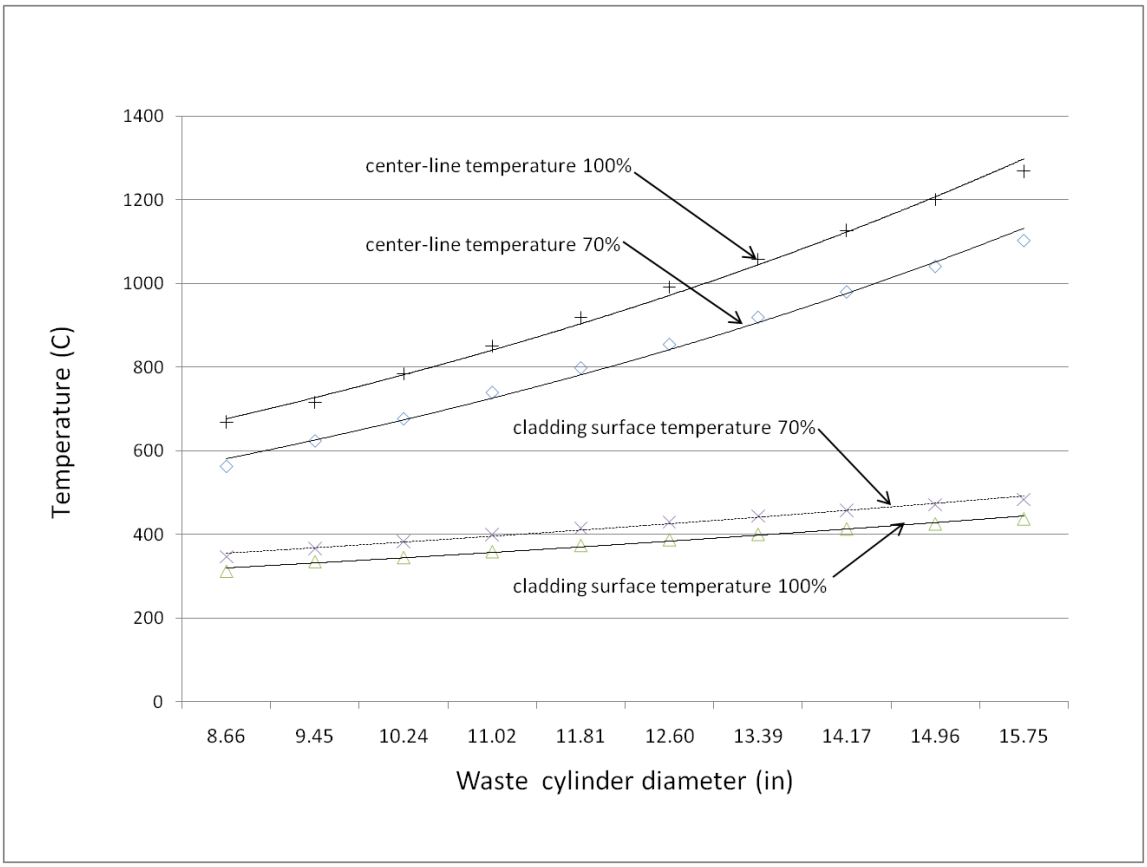

Fig. 5.30. Center-line temperature and cladding surface temperature as a function of waste form diameter. Where + refers to 100% loaded bentonite center-line temperature, ◊ 70% loaded bentonite center-line temperature, × 100% loaded bentonite cladding surface temperature, △ 70% loaded bentonite cladding surface temperature

6. CONCLUSIONS

Ions in a nitric acid solution were added to the bentonite clay. As the moisture is driven off the clay, the solution becomes increasingly concentrated with lower and lower pH. The effect of low pH on the cation exchange capacity is to lower it. Typical cation exchange values for bentonite are ~1 meq/g or lower [94]. Strontium (Sr^{2+}) cation exchange capacity as a function of pH onto a pillared aluminum montmorillonite was reported by Papachristodoulou *et al* [22] to be approximately 0.1 meq/g at a pH of 3.5, 0.64 meq/g at a pH 7.0 and 0.82 meq/g at pH 8.5. Delgado suggested the following Na^+-H^+ exchange reaction for sodium montmorillonite.

$$\text{Na-montmorillonite} + H_2O \leftrightharpoons \text{H-montmorillonite} + NaOH$$

He suggested the penetration of H^+ into the lattice were responsible for the decomposition of the montmorillonite, via release of exchangeable Al^{3+} and Mg^{2+} as ions [95]. Avena described the equilibrium between the hydrogen of the solution and the hydroxyl groups attached to the particle edges more generally as

$$SO^- + H^+ \rightleftharpoons SOH$$

and

$$SOH + H^+ \rightleftharpoons SOH_2{}^+$$

where the S represents any surface site [96]. In our case this may be occurring, but in our system the water is eventually completely driven off leaving all of the Cs, Ba, Sr, Rb, as well as the original Na, Ca, Fe, and Mg cations to precipitate onto the bentonite surfaces. In our bentonite, magnesium, iron, calcium, and sodium initially reside between the layers of silica and alumina sheets. These ions and the additional waste ions saturate the anion sites as well as precipitate on the bentonite surfaces.

6.1 Waste Form Consolidation

Porcelain is a ceramic usually produced by mixing kaolinite clay with quartz and feldspars. Approximate proportions are 50 wt% kaolin, 25 wt% fluxing agents, and 25 wt% quartz. Fluxing agents are typically potash feldspar ($K_2O{\cdot}Al_2O_3{\cdot}0.6SiO_2$), soda feldspar ($Na_2O{\cdot}Al_2O_3{\cdot}0.6SiO_2$), and lime feldspar ($CaO{\cdot}Al_2O_3{\cdot}0.2SiO_2$). The process of converting these raw materials to porcelain proceeds in an abbreviated form as follows: (1) Dehydroxylation breaks down the clay structure, converting kaoline to metakaoline. (2) α- to β-quartz inversion, a reversible transition from a trigonal to hexagonal crystal structure at 573°C. (3) Sanidine forms, which is a homogeneous mixure of alkali feldspars, at 700-1000°C. (4) Metakaolin transforms to a spinel-type structure and releases free amorphous silica at 950-1000°C. (5) Free silica forms a eutectic with the feldspar and alumina K_2O-Al_2O_3-SiO_2. The temperature depends on the type of feldspar, the concentration, and other components present. (6) As the temperature rises porosity is eliminated through viscous phase sintering. (7) The unstable spinel transforms to mullite at ~1000°C. (8) At ~1200°C the melt becomes saturated with silica quartz, and the quartz to cristobalite transformation begins. (9) Above 1200°C prismatic mullite crystals grow into the feldspar grains. (10) Cooling begins, the semi-solid nature of the glass phase prevents residual stresses into the glass transition temperature. (11) Cooling through the quartz inversion temperature at 573°C reduces quartz particle volume by 2% (this can crack the porcelain if not managed properly). (12) At 250 - 225°C, β to α-cristobalite inversion occurs, but less sudden than the quartz inversion, which makes this less of a fracture issue [97, 98]. Ohya and others found quartz grains cause cracking in porcelain due to a large thermal expansion differences between the crystalline quartz ($\alpha \approx 23 \times 10^{-6}K^{-1}$) and the glassy phase ($\alpha \approx 3 \times 10^{-6}K^{-1}$) in the temperature range 20- 750°C [99].

In our case we have a very similar composition, but the process feed has a different form. The total silica may be comparable, but the source in the raw feed for porcelain is quartz. Quartz dissolution does not occur until >1200°C. The porcelain feed is

~25% feldspar mineral, which has silica and alumina, but our system is comprised of bentonite saturated with up to 30 wt% alkali and alkaline earth metal ions. Thus the ions are consuming the alumina and silica to produce the feldspars and pollucite, omitting the alumina polymorphs that occur in porcelain. Despite these differences there are similarities in the crytalization process of porcelain with our system:

(1) At 550°C DSC shows an endotherm, and simultaneous mass loss, evident of dehydroxylation (Figure 5.6. 5.7) The hydroxyl groups attached to the alumina layers are driven off causing a collapse of the layered bentonite structure (600-800 °C), similar to what has been reported for pure bentonite [90], as well as bentonite saturated with cations [91]. The XRD scans show an amorphous hump which confirms the lack of crystal structure (Figures 5.13, 5.14). The montmorillonite becomes meta-montmorillonite after dehydroxylation, as reported by Malek [100]. Meta-montmorillonite is a porous amorphous material confirmed by the density at 700°C which is the lowest we recorded, over 50% for both 70% and 100% loadings (Figure 5.1). Balek reported that the cations move into the vacancies of the meta-montmorillonite that remain after dehydroxylation [91]. We see that the cations are easily leached from the structure that remains after sintering to 700°C, with leach rates over 900 ppm for cesium and barium at the 100% loading (Figure 5.29). The remaining water is lost at this step, the nitrate has been shown to be released at this stage as well [82].

(2) At 800°C the amorphous structure begins to crystallize, instead of the metakaolin in porcelain, we see the appearance of hexacelsian ($BaAl_2Si_2O_8$) and pollucite ($CsAlSiO_4$) in the XRD scans (Figures 5.13, 5.14). Hexacelsian is the first phase visible in the XRD at 800°C and 70% loading, pollucite also appears but in the 100% loaded sample also at 800°C. The leach rates determined by our simplified TCLP decrease for all elements tested, with the smallest change of 2.2 times less for strontium at 800°C than the 700°C sintering (Figure 5.29). We also see the Group I and Group II elements begin to segregate into distinct separate regions 800°C (Figure 5.19).

(3) 1000°C hexacelsian is no longer visible and has been replaced by monoclinic forms with variable strontium to barium ratios (Figures 5.14, 5.13). For the hexagonal to monoclinic transition to occur, Al-O and Si-O bonds must be broken to from a planar to three dimensional structure. Bansal reported the energy required, for hexagonal strontium to convert to monoclinic, as 527 kJ/mol [101]. In our DSC plots a peak is visible at ~900°C, which becomes endothermic due in part to this transformation, which continues downward as the ceramic eventually melts (Figures 5.6, 5.7). These celsian crystal structures that form exist in various ratios of barium to strontium. Our samples show a 50:50 Ba to Sr crystal phase at 1000°C at the 70% loading (bottom of Figure 5.13) as well as at 1200°C with a 100% loading (Figure 5.15). A separate 25:75 Ba to Sr ratio feldspar is detected at 1000°C and 100% loading (bottom of Figure 5.14). As the monoclinic feldspars grow, so does the pollucite phase. In the higher loading (100%) the pollucite XRD peaks double in intensisty from 800 to 1000°C sinterings (Figure 5.14). The crystals grow in separate regions as the separation of the alkali, and alkaline earths continues. The segeration is visible as separate phases growing in the backscattered image of the 100% loaded bentonite, as well as the concentration of elements in the elemental maps (Figure top 5.20). The leach rates with 1000°C sintering decreased to <100 ppm for all elements except strontium which is still high at 387 ppm.

(4) At 1100°C the backscattered image shows a uniform grey colored matrix with a dark phase within, and a larger white region throughout. The white is typical of high Z elements, such as cesium. The DSC has a steep downward slope at 1100°C indicative of energy consumption during melting. The grains of silica are no longer visible, and silica has become homogeneously distributed (Figure 5.28). The density has increased from 1.84 g/cm^3 at 1000°C to 2.18 g/cm^3, indicative of viscous sintering. The different structured phases embedded within the silica rich region indicate a eutectic has formed (Figure 5.22).

(5) 1200°C a high silica phase has formed and is filled with Sr- and Ba-feldspar crystals, and cesium has formed monoclinic crystals up to 10 μm wide (Figure 5.23). The ceramic is a light colored glassy structure, uniform in color and texture (Figure top right 5.1, and bottom right 5.3). Leach rates have dropped appreciably, the 700°C at the 100% loading leached >200 times more than in the 1200°C sinterings (Figure 5.29). The rubidium we can assume has done the same due to very similar chemistry, as well as rubidium's location in the elemental maps which overlap that of cesium (Figure 5.24, and Table 5.3). XRD plots are inconclusive with respect to rubidium, the low concentration 1.54–2.06 wt% (Table 5.4) coupled with overlapping peaks make confirmation difficult (Table 6.1). The bentonite is allowed to cool after sintering, I will forgo the steps and speak about cooling with respect to the phases present.

During sintering at ~800°C, crystallization begins with the appearance of a hexagonal barium alumino-silicate in the XRD (Figure 5.13). This compound has been found to be unstable [101]. Sorrell suggested perhaps the hexagonal celsian appears during rapid crystallization only to be consumed by the monoclinic feldspar [3]. Our XRD plots support this. The hexagonal celsian (barium alumino-silicate) is present at 800°C but not at 1000 or 1200°C (Figures 5.13, 5.14, and 5.15). The hexagonal celsian, or hexacelsian as it is known, has a transition from hexagonal to orthorhombic at ~300°C accompanied by a large volume change [102]. This property makes it undesirable in most applications where degradation is an issue to be avoided.

Bentonite sintered to ≤1000°C when cooled, contracts unevenly. It is evident in the discontinuous grains and rough cracked texture (Figure 5.3). By 1000°C the hexacelsian phase is no longer detectable by XRD and the monoclinic barium and strontium feldspars become prevalent (Figure 5.13, 5.14). The leach rates go down (Figure 5.29) as well as porosity (Table 5.2), and the bentonite becomes more dense (Table 5.1).

Table 6.1

Rubidium alumino-silicate and cesium alumino-silicate XRD overlap. Peak proximity in XRD scans of body centered cubic Cs and Rb alumino-silicates, truncated full data can be found in Figures A.3, A.10.

$CsAlSiO_4$		$RbAl(SiO_3)_2$	
2θ	intensity	2θ	intensity
15.915	6	15.898	2
18.395	2	18.392	3
24.415	44	24.435	29
26.13	100	26.166	100
29.29	4	29.327	3
30.729	44	30.797	33
32.136	1	33.562	5
33.455	4		
36.025	6	36.131	2
37.265	22	37.361	14
40.715	12	40.836	4
45.054	6	45.163	2
46.016	5	46.159	1
48.061	1	48.158	1
49.037	10	49.184	4
52.758	12	52.979	5
53.656	3	53.854	4

As the strontium and barium form crystals, so do cesium and rubidium. The cesium forms pollucite, a body centered cubic structure. In our samples it is first visible in the XRD plot at 800°C sintered bentonite with a 100% loading (center of Figure 5.14). The phase is prevalent in all samples sintered above 800°C, and develops strong XRD peaks by 1200°C (Figures 5.13, 5.14, 5.15). A minor high silica content cesium alumino-silicate ($CsAlSi_5O_{12}$) becomes visible in the 70% loaded bentonite at 1000°C (the ∘ in Figure 5.13). This phase is a base centered orthorhombic that has been reported to have anisotropic thermal expansion characteristics, with a higher thermal expansion below 500°C than above 500°C [103]. In high concentrations this could cause cracking during cooling. The bentonite sintered at 1000°C (Figure 5.3 center) has a mottled coloration as well as holes, and some with inclusions. This base centered monoclinic phase may have contributed to the rough texture by contracting at a different rate during cooling than the surrounding matrix. Also at 1000°C quartz has not yet dissolved, adding a phase with a volume change during cooling (α to β inversion).

The high silica cesium alumino silicate phase is not detected at 1200°C (Figure 5.15), neither is the hexagonal barium feldspar or quartz. With these gone the porosity reaches a minimum at 1200°C sinterings with 14.4% for the 70% loading and 4.7% for the 100%. The densities also increase to values above 2 g/cm^3 at sinterings over 1100°C (Table 5.1). As the minerals transform to phases with consistent thermal expansion behaviour, the bentonite ceramic becomes more dense and has lower porosity. The porosity is 33.6%, and 32.7% for 70% and 90% loadings at 1100°C, and 14.4% and 4.7% for 70% and 100% loadings at 1200°C (Table 5.2). This decrease in porosity (~57% for 70%) is greater than the decrease from 700°C to 1100°C (43% for the 70% loading). The decrease in porosity is due to viscous sintering.

During sintering a liquid phase forms, this liquid wets the grain surfaces and capillary forces quickly spread the liquid through the pores, eliminating porosity in the process. The solid's solubility in the liquid will determine the extent and effec-

tiveness of viscous phase sintering. If the solid is soluble the porosity is eliminated as the grains grow to minimize surface energy. The compact density increases as the viscous solid reacts to capillary action filling pores and cracks [104].

Bahat did a study [105] focused on the heterogeneous nucleation in alkaline earth feldspars. The study analyzed the effects different nucleating agents had on glass, primarily oxides. The systems were BaO-Al_2O_3-SiO_2, SrO-Al_2O_3-SiO_2 and CaO-Al_2O_3-SiO_2. Although working with glass, these observations have parallels with our case. Our nucleating oxides come from impurities in the bentonite, and although we do not begin with feldspars, they are created in our process. Bahat found barium would nucleate into feldspar crystals readily producing good quality glasses with a variety of oxide co-reactants. He noted strontium and calcium glass systems produced metastable fields, with hexagonal and orthorhombic structures, as well as stable triclinic orientations, but to a lesser extent. The barium nucleation product was limited to the metastable hexacelsian crystal phase. The hexacelsian nucleated from more oxide agents than any of the other crystals. These nucleating agents are used in small amounts typically less than 1%. When iron oxide was used as a nucleating agent the crystal growth was fast, forming a fine-grained ceramic. Bahat found the ratio of FeO/Fe_2O_3 did not affect nucleation rate.

Our samples have 4.85 wt% iron oxide (Fe_2O_3) according to the supplier. In our quantitative element analysis iron in the dark phase is at its highest concentration, at ~1.3% (Table 5.3). Alumina and silica as well as the alkaline earths metal ions are also in the dark phase. We observe the hexagonal barium structure before any other crystal phase, at the lower loading of 70% at 800°C (Figure 5.13). The presence of iron oxide may act as a nucleating agent accelerating the favored hexagonal barium feldspar as reported by Bahat [105].

What has occurred is the barium crystallized faster than the strontium; nucleated by the various impurities in the bentonite, the hexacelsian formed quickly. Due to the limited alumina, the strontium was not able to form crystals before the alumina

was consumed by the other reactants, and was left in the silica phase. Alumina is the limiting reactant during the formation of the alumino-silicates. If we assume a 1 kg basis, and all the alkali, and alkaline earth metals are to be converted to alumino-silicates 1.55 moles of alumina are required for bentonite with 25 wt% waste, and 1.98 moles for the 32 wt% waste loading. If the remainder of the material is dry and dehydroxylated bentonite (750.7 g for the 25 wt% waste, and 680.9 g for the 32 wt% waste) only 1.52 and 1.38 moles of alumina are available at 25 and 32 wt% loadings, respectively. There is a 0.03 mole deficiency for the 25 wt% waste loading, and 0.6 mole deficiency for the 32 wt% waste loading (calculations in Appendix C).

During the SEM analysis of the 1200°C sintered bentonite, the feldspar crystals appeared to be protruding from a depression. Upon closer inspection, the surface was found to be flat. The back-scattered image intensity is determined by the number of electrons that bounce off the target, larger nuclei deflect better than light nuclei. Silicon and aluminum are light elements compared to the alkali and alkaline earths. The result is the light elements appear dark, and the heavy ones appear bright. As the electron gun bombards the ceramic surface with electrons they penetrate until they hit an atom and are elastically scattered back to the detector. The electrons are deflecting off of the feldspar crystals after going through various amounts of silicon, the intensity of the signal is decreased as the silicon thickness increases, creating an illusion of a three dimensional surface.

The TCLP leachate had high concentrations of strontium up to 1100°C. The strontium unable to form crystals leached easily. The strontium was not completely immobilized until the temperature of the silica was high enough to melt, then viscous sintering could occur. Melting is visible in the silica element maps at 1100°C where silica becomes homogeneously distributed (Figure 5.28). The silica is no longer present as quartz crystals at temperatures >1000°C, but has melted and spread throughout the ceramic, visible as a disappearance of large areas absent of all elements except silicon (Figures 5.27, 5.28).

Optical images of sintered bentonite at temperatures <1100°C show pores and cracking (Figure 5.3). Two contributing factors to the porosity and cracking are differences in thermal expansion coefficients of the various phases, and if viscous phase sintering is occurring or not. In the XRD scans at lower temperatures hexacelsian is present, which has a an orthorhombic transition with a volume change at ~300°C [102]. Bansal reports that both the barium $BaAl_2Si_2O_8$ and strontium $SrAl_2Si_2O_8$ celsian go through a hexacelsian phase before transitioning to the monoclinic form. The transition for barium hexacelsian to the monoclinic is very slow, while the strontium analog occurs rapidly. Our sinterings were held for 12 hours, so this is not an issue. Bansal also stated the two form solid solutions across the entire composition range [106]. If there were enough alumina both barium and strontium could form crystals, and mix within the glass phase.

At 1000°C and 70% loading $CsAlSi_5O_{12}$ is observed in the XRD (Figure 5.14), this compound also displays anisotropic thermal expansion characteristics, at temperatures <500°C it exists as an orthorhombic rather than the body-centered cubic at higher temperatures [103]. As the sintered bentonite cools areas with high concentrations of these phases will separate from phases with lower thermal expansion coefficients. Other sources of porosity are incomplete consolidation of the green pucks, and pores that remain after dehydroxylation. Porosity is high before liquid phase sintering has developed, and before the high thermal expansion polymorths have transitioned to their stable counterparts. In the optical images of the 1000°C sintered bentonite at 26wt% and 31wt% waste (Figure 5.3), small crystal inclusions are visible inside the holes. These may be crystals that shrunk quickly relative to the surrounding matrix, or solid quartz crystals which have separated from the surrounding material. To limit porosity the sintering must be carried out until the silica melts, and the monoclinic forms are allowed to develop. The thermal conductivity is maximized at low porosity (Figure 5.4).

In our system sintering should be carried out to at least 1100°C. The leach testing shows strontium concentration in the leachate <100 ppm after sintering to 1100°C, but to lower the porosity substantially sintering to 1200°C is required, thus increasing thermal conductivity. The waste loadings should not be lower than 21 wt% waste, waste concentrations <21 wt% have a detrimental effect on the ceramic's material properties. Samples loaded with 15 wt% waste bloated at 1200°C, and loadings with 21 wt% waste and above had smooth textures and uniform coloration when sintered at >1100°C (Figure 5.1).

6.2 Engineering Considerations

The FPEX solution will require careful planning and engineering to ensure safety and reliable processing. Minimizing the number of steps will reduce sources of failure. In this study the liquid and clay solution was dried ignoring the off-gases, this will not be possible in a full scale operation. Each step will require careful accounting to keep track of all losses, as well as the neutralization of HNO_3, and capture of nitrogen oxides.

In our experiments an intermediate step produced a powder. From a nonproliferation and safety perspective this is serious matter. The dry powder may be an integral processing step, but the amount of powder available at any given time must be minimized as much as possible. This can be accomplished by continuous, rather than batch processing as well as low volumetric flow rates. This has the added advantage of reducing shielding requirements for downstream operations.

Engineering and design of a radioactive waste processing facility must consider each potential problem, such as the location of high pressure lines and plumbing, which will need to be routed with adequate separation from high risk areas. The choice of equipment will require careful cost analysis, due to contamination replacing parts is undesirable, although at times unavoidable.

If volitization is cannot be completely eliminated, an engineering remedy is necessary. In vitrification operations a cold cap on the melt reduces the gaseous losses. The cold cap is a layer of solid glass that is allowed to form on top of the glass melt surface. In a ceramic process, perhaps a similar technique is possible. The ceramic may be formed as a monolith, which could be continuously grown in a manner that keeps the heated region sealed, and only relatively cool ceramic is allowed to be exposed. Engineering such a system would be difficult due to the high volume of acidic off-gases which must be managed.

Temperatures greater than 1000°C are necessary to pass TCLP for this process, perhaps greater to improve porosity, and therefore thermal conductivity. Grinding and re-sintering could improve porosity substantially, but introducing an addition step that requires producing a powder is highly undesirable. A preferred method would be to reach the optimum density in one continuous step. The size of the final waste form will be determined by the centerline temperature, which will have to fall below the melting point of the waste form matrix. The melting point of each phase will need to be determined experimentally. With a minimum melting known, an engineering decision will be required to ensure a margin of safety. Typically, a temperature below the glass transition temperature is chosen for glass waste forms. In our simulations the size of the waste form drastically affects the center-line, and cladding surface temperatures. These considerations each have economic as well as logistic implications and require careful analysis.

Once the waste form is created the durability will need to be assessed. Radiation damage can manifest itself in Frenkel defects, where an interstitial is paired with a vacancy. These defects can either cluster and grow into defect loops, or combine and annihilate each other [107]. Pollucite has been analyzed after Cs-137 has decayed and displayed small volume increases [38], in our system we also have strontium to contend with in two separate phases. How this complex structure responds to radiation will require testing. Sickafus has shown radiation resistance of each material

will depend on ion charge and size, as well as ease of defect movement in the structure [108].

Further research is required to make a final assessment, but sintered bentonite may provide cost benefits over other waste forms. The process employs inexpensive raw materials, and has a relatively simple preparation procedure which does not require high pressures, or extreme temperatures. The sintered product is a ceramic solid capable of waste loadings up to 30 wt% alkali and alkaline earth metals, where the bulk of the waste is embedded within a crystaline matrix. As the crystalline structure developed, the leach rates improved. Strontium was not completly crystallized, but when the bentonite was sintered above 1100°C strontium leaching was also reduced significantly. The Cesium losses could not be exactly determined, but the cesium concentration across all sintering temperatures varied by less than 1 wt% with a maximum standard deviation of .22, or over 98 wt% of the cesium remains in the bentonite during sintering (D.2). Waste form sizes were modeled, and found comprable to vitrified waste glass, although holding more waste.

REFERENCES

[1] J. C. Zinc, DOE Rises to Nuclear Waste Challenges, Power Eng. 107 (5) (2003) 16.

[2] C. W. Forsberg, Rethinking high-level waste disposal: Separate disposal of high-heat radionuclides ^{90}Sr and ^{137}Cs, Nucl. Technol. 131 (2) (2000) 252 – 268.

[3] C. Sorrell, Solid state formation of barium, strontium and lead feldspars in clay-sulfate mixtures, Am. Mineral 47 (3-4) (1962) 291–298.

[4] V. Spitsyn, V. Gromov, A study of the systematic adsorption of radioactive strontium by montmorillonite and its fixation by roasting, At. Energ. 5 (4) (1959) 1341–1347.

[5] D. M. Strachan, W. W. Schulz, Glass and ceramic materials for the immobilization of megacurie-amounts of pure cesium-137, Tech. Rep. ARH-SA-246, Pac. Northwest Lab., Richland, WA (USA) 1976.

[6] D. Strachan, W. Schulz, Characterization of pollucite as a material for long-term storage of cesium-137, Am. Ceram. Soc. Bull. 58 (9) (1979) 865–869.

[7] E. Vance, B. Scheetz, M. Barnes, B. Bodnar, Studies of pollucite, The Scientific Basis for Nuclear Waste Management, Stephen V. Topp, (Ed.), Elsevier Science Publishing Co. Inc, Berlin Germany, 1982.

[8] N. Hess, F. Espinosa, S. Conradson, W. Weber, Beta radiation effects in ^{137}Cs-substituted pollucite, J. Nucl. Mater. 281 (1) (2000) 22 – 33.

[9] R. Ewing, F. von Hippel, Nuclear waste management in the United States–Starting over, Science 325 (5937) (2009) 151.

[10] Alternatives to direct SNF disposal: Advanced nuclear fuel cycles, in: R. G. Bennet (Ed.), 2003 NAE National Meeting Symposium in honor of Foreign Secretary Harold K. Forsen, 2003.

[11] R. Wigeland, T. Bauer, T. Fanning, E. Morris, Spent nuclear fuel separations and transmutation criteria for benefit to a geologic repository, Nucl. Technol. 154 (1) (2006) 95–106.

[12] G. Vandegrift, M. Regalbuto, S. Aase, A. Bakel, T. Battisti, D. Bowers, J. Byrnes, M. Clark, J. Emery, J. Falkenberg, et al., Designing and Demonstration of the UREX+ Process Using Spent Nuclear Fuel, in: Proceedings of the International Conference on Advances for Future Nuclear Fuel Cycles, Nîmes, France, 2004, pp. 21–24.

[13] M. Thompson, Demonstration of the UREX Solvent Extraction Process with Dresden Reactor Fuel Solution, Tech. rep., WSRC-TR-2002-00444, Savannah River Site, Aiken, SC (USA) 2002.

[14] C. L. Riddle, J. D. Baker, J. D. Law, C. A. McGrath, D. H. Meikrantz, B. J. Mincher, D. R. Peterman, T. A. Todd, Fission product extraction (FPEX): Development of a novel solvent for the simultaneous separation of strontium and cesium from acidic solutions, Solvent Extr. Ion Exch. 23 (3) (2005) 449–461.

[15] J. Law, R. Herbst, D. Peterman, R. Tillotson, T. Todd, Development of a cobalt dicarbollide/polyethylene glycol solvent extraction process for separation of cesium and strontium to support advanced aqueous reprocessing, Nucl. Technol. 147 (2) (2004) 284–290.

[16] T. A. Todd, T. A. Batcheller, J. D. Law, R. S. Herbst, Cesium and strontium separation technologies literature review, Tech. Rep. INEEL/EXT-04-01895, Idaho National Laboratory, Idaho Falls, ID (USA) 2004.

[17] M. Benedict, T. H. Pigford, H. W. Levi, Nuclear Chemical Engineering, Second Edition, McGraw-Hill Inc., New York NY, 1981.

[18] L. P. Hatch, Ultimate disposal of radioactive wastes, Tech. rep., BNL-1345, Brookhaven National Lab., Upton, NY (USA) 1953.

[19] S. G. Barney, Fixation of radioactive waste by hydrothermal reaction with clays, American Chemical Society, Washington, DC, 1976.

[20] P. Pusch, Use of bentonite for isolation of radioactive waste products, Clay Miner. 27 (1992) 353–361.

[21] U. Bartl, K. Czurda, Migration and retention phenomena of radionuclides in clay-barrier systems, Appl. Clay Sci. 6 (3) (1991) 195–214.

[22] C. Papachristodoulou, A new approach for enhancing Sr^{2+} retention by an Al-PILC in acidic solutions, Microporous Mesoporous Mater. 39 (1–2) (2000) 367–379.

[23] J. Kulp, Geologic Time Scale Isotopic age determinations on rocks of known stratigraphic age define an absolute time scale for earth history, Science 133 (3459) (1961) 1105–1114.

[24] I. MacLaren, J. Cirre, C. Ponton, Hydrothermal synthesis of pollucite ($CsAlSi_2O_6$) powders, J. Am. Ceram. Soc. 82 (11) (1999) 3242–3244.

[25] N. Miyagawa, N. Shinohara, M. Okumiya, Synthesis and fabrication of pollucite glass-ceramics by using arc melting technique, J. Ceram. Soc. Jpn. 107 (1248) (1999) 762–765.

[26] H. Fryda, G. Vetter, P. Boch, High-alumina cement/silica fume materials for caesium trapping, in: Third ECers. Proc. 3rd European Ceramic Society Conf., 3, 1993, pp. 213–218.

[27] M. J. Lambregts, S. M. Frank, Characterization of cesium containing glass-bonded ceramic waste forms, Microporous Mesoporous Mater. 64 (1-3) (2003) 1–9.

[28] J.-L. Rehspringer, J. Balencie, S. Vilminot, D. Burger, A. Boos, C. Estourns, Confining caesium in expanded natural perlite, J. Eur. Ceram. Soc. 27 (2-3) (2007) 619–622.

[29] E. Konovalov, O. Starkov, E. Glagovskii, M. Myshkovskii, A. Kuprin, L. Pelevin, L. Gudkov, A. Nardova, Immobilization of silica gel fixed cesium and strontium into mineral-like matrices in the SHS mode, Sov. Radiochem. 44 (4) (2002) 420–422.

[30] C. Pereira, A method for synthesizing pollucite from chabazite and cesium chloride, U.S. Patent 5875407, 1997, assigned to The United States of America.

[31] N. G. Vasil'eva, N. N. Anshits, O. M. Sharonova, M. V. Burdin, A. G. Anshits, Immobilization of cesium and strontium radionuclides in framework aluminosilicates with the use of porous glass-ceramic matrices based on coal fly ash cenospheres, Glass Phys. Chem. 31 (5) (2005) 637–647.

[32] H. Mimura, K. Akiba, M. Ozawa, Preparation of Ceramic Solid Forms Immobilizing Cesium and/or Strontium and Evaluation of their Physical and Chemical Properties, in: Proc. Int. Conf. Nuclear Energy for New Europe, 2002, pp. 9–12.

[33] V. I. Bogdanova, B. A. Fursenko, I. A. Belitskij, L. M. Predeina, G. I. Galaj, V. S. Pavlyuchenko, I. V. Drobot, Cesium and strontium immobilization using zeolite-containing rocks and high temperature treatment, Vopr. Materialoved. 3 (1997) 31–40.

[34] E. Zimmer, K. Scharf, S. O. Schmidt, A stable ceramic matrix for fixation of fission products, Waste Manage. 201 (1993) 320–325.

[35] K. Yanagisawa, M. Nishioka, N. Yamasaki, Immobilization of cesium into pollucite structure by hydrothermal hot-pressing, J. Nucl. Sci. Technol. 24 (1) (1987) 51–60.

[36] J. L. Anchell, J. C. White, M. R. Thompson, A. C. Hess, An ab initio periodic Hartree-Fock study of group IA cations in ANA-type zeolites, J. Phys. Chem. 98 (1616) (1994) 4463–4468.

[37] R. Barrer, L. Rees, Self-diffusion of alkali metal ions in analcite, Trans. Faraday Soc. 56 (1960) 709–721.

[38] J. A. Fortner, Determination of transmutation effects in crystalline waste forms, Tech. rep., EMSP-55382, Argonne National Lab., Argonne, IL (USA) (1999).

[39] L. P. Ogorodova, L. V. Melchakova, I. A. Kiseleva, I. A. Belitsky, Thermochemical study of natural pollucite, Thermochim. Acta 403 (2) (2003) 251–256.

[40] I. V. Chernyshova, V. M. Agoshov, M. Gambino, P. Gaune, J. P. Bros, Thermodynamic properties and barium feldspars of strontium, Science 175 (1991) 119–127.

[41] I. Yanase, S. Tamai, H. Kobayashi, Sintering of pollucite using amorphous powder and its low thermal expansion property, J. Ceram. Soc. Jpn. 111 (8) (2003) 533–536.

[42] A. Tool, Relation Between Inelastic Deformability and Thermal Expansion of Glass in its Annealing Range*, J. Am. Ceram. Soc. 29 (9) (1946) 240–253.

[43] G. Beall, Refractory glassceramics based on alkaline earth aluminosilicates, J. Eur. Ceram. Soc. 29 (7) (2009) 1211–1219.

[44] D. Bickford, A. Applewhite-Ramsey, C. Jantzen, K. Brown, Control of radioactive waste glass melters: I, Preliminary general limits at Savannah River, J. Am. Ceram. Soc. 73 (10) (1990) 2896–2902.

[45] J. H. Saling, A. W. Fentiman, Radioactive Waste Management, 2nd Edition, Taylor & Francis, New York NY, 2002.

[46] D. Wronkiewicz, J. Bates, S. Wolf, E. Buck, Ten-year results from unsaturated drip tests with UO_2 at 90C: Implications for the corrosion of spent nuclear fuel, J. Nucl. Mater. 238 (1) (1996) 78–95.

[47] H. Zimmermann, Investigations on swelling and fission gas behavior in uranium dioxide, J. Nucl. Mater. 75 (1) (1978) 154–161.

[48] I. Zacharie, S. Lansiart, P. Combette, M. Trotabas, M. Coster, M. Groos, Thermal treatment of uranium oxide irradiated in pressurized water reactor: Swelling and release of fission gases, J. Nucl. Mater. 255 (2-3) (1998) 85–91.

[49] J. Long, R. Ewing, Yucca Mountain: Earth-science issues at a geologic repository for high-level nuclear waste, Annu. Rev. Earth Planet. Sci. 32 (2004) 363–401.

[50] J. L. McElroy, W. J. Bjorklund, W. F. Bonner, Waste vitrification: A historical perspective, in: The Treatment and Handling of Radioactive Wastes, American Nuclear Society, Richland, Wash., 1982, pp. 171–177.

[51] D. F. Bickford, R. Schumacher, Vitrification of hazardous and radioactive wastes, Ceram. Eng. Sci. Proc. 16 (2) (1995) 1 – 10.

[52] R. Nakaoka, G. Veazey, D. Mullins, C. Smith, Vitrification system for the treatment of plutonium-bearing waste at Los Alamos National Laboratory, in: Conference: GLOBAL 2001, Paris (FR), 2001.

[53] G. Becker Jr, J. McKibben, S. Site, N. Reno, Vitrification of Rocky Flats Ash Followed by Encapsulation in the Defense Waste Processing Facility, Tech. rep., WSRC-MS-96-0196, Savannah River Site, Aiken SC (USA) (1997).

[54] H. Kamizono, Volatilization of cesium and ruthenium from high-level waste glass, in: High Level Radioactive Waste Management 1990, American Society of Civil Engineers, Las Vegas, NV, USA, 1990, pp. 1115 – 1118.

[55] N. Bibler, T. Fellinger, S. Marra, R. O'Driscoll, J. Ray, W. Boyce, Tc-99 and Cs-137 volatility from the DWPF production melter during vitrification of the first macrobatch of HLW sludge at the Savannah River site, in: Materials Research Society Symposium - Proceedings, Vol. 608, Boston, MA, USA, 2000, pp. 697 – 702.

[56] M. Plodinec, B. Kitchen, Establishing the Acceptability of Savannah River Site Waste Glass, Tech. rep., WSRC-RP-89-1409, Westinghouse Savanah River Co., Aiken, SC (USA) (1990).

[57] M. A. Schiffhauer, D. E. Carl, L. E. Rykken, Design of a High-level Waste Pretreatment Process for the Purpose of Vitrification, in: Proceedings Waste Management 1985, Tucson, AZ, USA, 1986, pp. 479 – 487.

[58] T. N. J. Sargent, T. J. Overcamp, D. F. Bickford, C. A. Cicero-Herman, Vitrification of cesium-laden organic ion-exchange resin in a stirred melter, Nucl. Technol. 123 (1) (1998) 60 – 66.

[59] M. K. Andrews, Glass formulation development and testing for the vitrification of cesium-loaded (CST), in: Proceedings of the Air & Waste Management Association's Annual Meeting & Exhibition, Toronto, Can, 1997.

[60] D. G. Bennett, J. J. W. Higgo, S. M. Wickman, Review of Waste Immobilization Matrices, Tech. Rep. 0126-1, Galson Sciences Limited, Oakham (UK) (2001).

[61] J. Hanna, L. Aldridge, E. Vance, Cs speciation in cements, in: Materials Research Society Symposium - Proceedings, Vol. 663, Sydney, Australia, 2001, pp. 89 – 96.

[62] R. Neilson Jr., P. Kalb, M. Fuhrmann, P. Colombo, Solidification of Ion Exchange Resin Wastes in Hydraulic Cement, in: ANS Topical Meeting on: The treatment and handling of radioactive wastes, Richland, WA, 1982, pp. 497–503.

[63] D. Perera, M. Blackford, E. Vance, J. Hanna, K. Finnie, C. Nicholson, Geopolymers for the immobilization of radioactive waste, in: Proceedings of the Materials Research Society Symposium, Vol. 824, Warrendale, Pa.; Materials Research Society; 1999, 2004, pp. 607–612.

[64] D. Perera, E. Vance, Z. Aly, J. Davis, C. Nicholson, Immobilization of Cs and Sr in geopolymers with Si/Al molar ratio of ≈2, Ceram. Trans. 176 (2005) 91–96.

[65] N. V. Elizondo, E. Ballesteros, B. I. Kharisov, Cleaning of liquid radioactive wastes using natural zeolites, Appl. Radiat. Isot. 52 (2000) 27–30.

[66] J. Yoo, T. Shinagawa, J. P. Wood, W. P. Linak, D. A. Santoianni, C. J. King, Y. Seo, J. O. L. Wendt, High-temperature sorption of cesium and strontium on dispersed kaolinite powders, Environ. Sci. Technol. 39 (2005) 5087–5094.

[67] G. N. Brown, J. R. Bontha, K. J. Carson, R. J. Elovich, J. R. DesChane, Comparison of Inorganic Ion Exchange Materials for Removing Cesium, Strontium, and Transuranic Elements from K-basin Water, Tech. Rep. 11746, Pacific Northwest National Laboratory, Richland, WA (USA) (1997).

[68] H. Mimura, T. Hirabayashi, M. Ozawa, Leachability and thermal properties of ceramic solid forms immobilizing cesium and/or strontium, in: Proceedings of the International Conference - Nuclear Energy for New Europe, Portoroz, Slovenia, 2003, pp. 615 – 622.

[69] K. Reeve, A. Ringwood, The SYNROC process for immobilizing high-level nuclear wastes, in: Proceedings of an International Conference on Radioactive Waste Management, Seattle, WA, USA, 1984, pp. 307 – 24.

[70] I. W. Donald, B. L. Metcalfe, R. N. J. Taylor, Review the immobilization of high level radioactive wastes using ceramics and glasses, J. Mater. Sci. 32 (1997) 5851–5887.

[71] M. Carter, E. Vance, H. Li, Hollandite-rich ceramic melts for the immobilization of Cs, in: Scientific Basis for Nuclear Waste Management XXVII: Proceedings of the Materials Research Society Symposium, Vol. 807, 2004, pp. 249–254.

[72] M. Carter, M. Stewart, E. Vance, B. Begg, S. Moricca, J. Tripp, HIPed Tailored Ceramic Waste Forms for the Immobilization of Cs, Sr and Tc, in: Proceedings Global 2007, INL/CON-07-12875, Idaho National Laboratory (INL), 2007.

[73] J. Tripp, V. Maio, Evaluation of the use of synroc to solidify the cesium and strontium separations product from advanced aqueous reprocessing of spent nuclear fuel, Tech. Rep. INL/EXT-06-01377, Idaho National Laboratory, Idaho Falls, ID (USA) (2006).

[74] C. Jantzen, Characterization and performance of Fluidized Bed Steam Reforming (FBSR) product as a final waste form, Ceram. Trans. 155 (2004) 319–329.

[75] M. Cowen, J. B. Mason, K. Ryan, D. Schmoker, Steam reforming technology for denitration and immobilization of DOE tank wastes, Ceram. Trans. 176 (2006) 99 – 110.

[76] C. M. Jantzen, J. M. Pareizs, T. H. Lorier, J. C. Marra, Durability testing of Fluidized Bed Steam Reforming (FBSR) products, Ceram. Trans. 176 (2006) 121 – 137.

[77] J. B. Mason, D. Bradbury, Process for the treatment of radioactive graphite U. S. Patent 6625248, 1997, assigned to Studsvik, Inc.

[78] G. E. Voelker, W. G. Steedman, R. R. Chandran, Steam reforming of low-level mixed waste, Tech. Rep. DOE/MC/32091-97/C0789, ThermoChem Inc. Santa Rosa, CA (USA) (1996).

[79] J. L. Tripp, T. G. Garn, R. D. Boardman, J. D. Law, Steam reforming solidification of cesium and strontium separations product from advanced aqueous processing of spent nuclear fuel, in: Proceedings Waste Management 2006, 2006.

[80] A. Herbst, Optimization of Hydraulic Cement Ad Mixture Waste Forms for Sodium-Bearing, High Aluminum, and High Zirconium Wastes, in: Proceedings of the 18th Annual US Department of Energy Low-Level Radioactive Waste Management Conference, 1997.

[81] Y. Bao, S. Kwan, D. Siemer, M. Grutzeck, Binders for radioactive waste forms made from pretreated calcined sodium bearing waste, J. Mater. Sci. 39 (2) (2004) 481 – 488.

[82] M. D. Kaminski, C. J. Mertz, M. Ferrandon, N. L. Dietz, G. Sandi, Physical properties of an alumino-silicate waste form for cesium and strontium, J. Nucl. Mater. 392 (3) (2009) 510–518.

[83] W. J. Parker, R. J. Jenkins, C. P. Butler, G. L. Abbott, Flash method of determining thermal diffusivity, heat capacity, and thermal conductivity, J. Appl. Phys. 32 (9) (1961) 1679–1684.

[84] R. N. Guillemette, Methods of soil analysis. part 5. mineralogical methods, in: A. L. Ulery, L. R. Drees (Eds.), Methods of Soil Analysis, Vol. 5, Soil Science Society of America, Inc, Madison, Wisconsin, USA, 2008, pp. 325–365.

[85] The EPA TCLP: Toxicity Characteristic Leaching Procedure and Characteristic Wastes (D-codes) (http://www.ehso.com/cssepa/TCLP.htm 2009).

[86] M. Kaminski, Engineering product storage under the advanced fuel cycle initiative. Part I: An iterative thermal transport modeling scheme for high-heat-generating radioactive storage forms, J. Nucl. Mater. 347 (1-2) (2005) 94–103.

[87] R. Coble, W. Kingery, Effect of porosity on physical properties of sintered alumina, J. Am. Ceram. Soc. 39 (11) (1956) 377–385.

[88] R. Grim, International Series in the Earth Sciences: Applied Clay Mineralogy, McGraw-Hill, New York, 1962, pp. 352–355.

[89] M. Onal, Y. Sarikaya, Thermal behavior of a bentonite, J. Therm. Anal. Calorim. 90 (1) (2007) 167–172.

[90] R. Grim, W. Bradley, Investigation of the effect of heat on the clay minerals illite and montmorillonite , J. Am. Ceram. Soc. 23 (8) (1940) 242–248.

[91] V. Balek, Z. Malek, S. Yariv, G. Matuschek, Characterization of montmorillonite saturated with various cations, J. Therm. Anal. Calorim. 56 (1) (1999) 67–76.

[92] B. Yoshiki, K. Matsumoto, High-temperature modification of barium feldspar, J. Am. Ceram. Soc 34 (9) (1951) 283–86.

[93] J. V. Crum, A. L. Billings, J. Lang, J. C. Marra, C. Rodriguez, J. V. Ryan, J. D. Vienna, Development of Glass Compositions to Immobilize Alkali, Alkaline Earth, Lanthanide and Transition Metal Fission Products from Nuclear Fuel Reprocessing, Tech. rep., SRNL-STI-2009-00355, Savannah River Site, Aiken, SC (USA) (2009).

[94] N. Hutson, M. Hoekstra, R. Yang, Control of microporosity of Al_2O_3-pillared clays: effect of pH, calcination temperature and clay cation exchange capacity, Microporous Mesoporous Mater. 28 (3) (1999) 447–459.

[95] A. Delgado, F. Gonzalez-caballero, J. M. Bruque, On the zeta potential and surface charge density of montmorillonite in aqueous electrolyte solutions, J. Colloid Interface Sci. 113 (1) (1986) 203–211.

[96] M. Avena, R. Cabrol, C. De Pauli, Study of some physicochemical properties of pillared montmorillonites; acid-base potentiometric titrations and electrophoretic measurements, Clays Clay Miner. 38 (4) (1990) 356–362.

[97] W. Carty, U. Senapati, Porcelain-raw materials, processing, phase evolution, and mechanical behavior, J. Am. Ceram. Soc. 81 (1) (1998) 3–20.

[98] Y. Iqbal, W. Lee, Microstructural evolution in triaxial porcelain, J. Am. Ceram. Soc. 83 (12) (2000) 3121–3127.

[99] Y. Ohya, Y. Takahashi, M. Murata, Z. Nakagawa, K. Hamano, Acoustic emission from a porcelain body during cooling, J. Am. Ceram. Soc. 82 (2) (1999) 445–448.

[100] Z. Malek, V. Balek, D. Garfinkel-Shweky, S. Yariv, The study of the dehydration and dehydroxylation of smectites by emanation thermal analysis, J. Therm. Anal. Calorim. 48 (1) (1997) 83–92.

[101] N. Bansal, C. H. Drummond, Kinetics of hexacelsian-to-celsian phase transformation in $SrAl_2Si_2O_8$, J. Am. Ceram. Soc. 76 (5) (1993) 1321–1324.

[102] L. Barbeeri, A. Corradi, C. Leonelli, T. Manfredini, M. Romagnoli, C. Siligardi, The microstructure and mechanical properties of sintered celsian and strontium-celsian glass-ceramics, Mater. Res. Bull. 30 (1) (1995) 27–41.

[103] M. Fisch, T. Armbruster, B. Kolesov, Temperature-dependent structural study of microporous $csalsi_5o_{12}$, J. Solid State Chem. 181 (3) (2008) 423–431.

[104] R. German, Liquid Phase Sintering, Plenum Pub Corp, New York, NY, 1985.

[105] D. Bahat, Heterogeneous nucleation of alkaline earth feldspars in glasses, J. Mater. Sci. 4 (10) (1969) 847–854.

[106] N. Bansal, Solid state synthesis and properties of monoclinic celsian, J. Mater. Sci. 33 (19) (1998) 4711–4715.

[107] K. Sickafus, L. Minervini, R. Grimes, J. Valdez, M. Ishimaru, F. Li, K. McClellan, T. Hartmann, Radiation tolerance of complex oxides, Science 289 (5480) (2000) 748–751.

[108] K. Sickafus, R. Grimes, J. Valdez, A. Cleave, M. Tang, M. Ishimaru, S. Corish, C. Stanek, B. Uberuaga, Radiation-induced amorphization resistance and radiation tolerance in structurally related oxides, Nat. Mater. 6 (3) (2007) 217–223.

APPENDIX A
XRD REFERENCE PDFS

Pattern : 00-019-0002 **Radiation =** 1.540600 **Quality :** Indexed

$(K,Ba,Na)(Si,Al)_4O_8$

Potassium Barium Aluminum Silicate
Orthoclase, Ba-rich
Also called: hyalophane

Lattice : Monoclinic
S.G. : C2/m (12)

a = 8.55200
b = 13.04000
c = 7.20000
a/b = 0.65583
c/b = 0.55215

beta = 115.70
Z = 4

Mol. weight = 279.44
Volume [CD] = 723.50
Dx = 2.565
Dm = 2.880

Sample source or locality: Specimen from Busovaca, Yugoslavia.
Analysis: Chemical analysis (wt.%): Si O2 49.54, Al2 O3 23.14, Fe2 O3 0.11, MgO 0.04, BaO 19.01, CaO 0.19, Na2 O 1.65, K2 O 6.37.
Optical data: A=1.544, B=1.547, Q=1.549, Sign=-, 2V=69°
Color: Colorless
Data collection flag: Ambient.

Univ. of Oxford, Dept. of Geology and Mineralogy, Oxford, England, UK., Private Communication (1967)

Radiation : CuKa
Lambda : 1.54180
SS/FOM : F30= 10(0.0490,64)

Filter : Beta
d-sp : Debye-Scherrer

2th	i	h	k	l
13.612	10	0	0	1
15.264	2	-1	1	1
19.322	16	0	2	1
21.136	8	-2	0	1
23.517	45	1	3	0
24.572	16	-1	3	1
25.208	8	-2	2	1
25.727	50	-1	1	2
26.914	90	2	2	0
27.507	100	0	0	2
29.757	70	1	3	1
30.699	40	0	4	1
32.292	20	-1	3	2
34.882	45	-2	4	1
35.598	6	3	1	0
37.121	8	-1	5	1
37.768	6	-3	3	1
38.610	10	-1	1	3
39.856	6	-3	3	2
40.416	6	-2	2	3
40.798	10	1	5	1
41.584	35	0	6	0
42.402	10	2	4	1
43.038	8	-4	0	2
43.694	10	3	1	1
45.306	10	-4	2	2
45.888	10	2	2	2
46.535	2	-3	3	3
47.202	8	-3	5	1
48.131	2	3	3	1
48.930	10	1	1	3
50.674	35	-2	0	4
51.533	8	-4	4	1
54.830	8	3	1	2
55.514	8	-1	7	2
56.366	10	0	8	0
57.995	6	-4	2	4
58.642	8	0	2	4
60.415	8	5	1	0
61.166	8	-4	6	1
61.799	25	2	8	0
63.834	2	0	8	2
64.478	8	2	4	3
65.444	8	-6	0	2
66.335	8	-5	5	1
67.473	8	1	3	4
68.825	2	-3	3	5
69.939	8	-1	9	2

Fig. A.1. Potassium barium aluminum silicate, orthoclase-barium rich

Pattern : 00-019-0003 **Radiation =** 1.540600 **Quality :** Blank

$(K,Ba)(Si,Al)_4O_8$

Potassium Barium Aluminum Silicate
Orthoclase, Ba-rich
Also called: hyalophane

Lattice : Monoclinic
S.G. : C2/m (12)

a = 8.61600
b = 13.05900
c = 7.19900
a/b = 0.65977
c/b = 0.55127

beta = 115.70
Z = 4

Mol. weight = 279.44
Volume [CD] = 729.88
Dx = 2.543

Optical data: B=1.557
General comments: (0.5 K Al Si3 O8) (0.43 Ba Al2 Si2 O8).
Additional pattern: Validated by calculated pattern.
Data collection flag: Ambient.

Univ. of Oxford, Dept. of Geology and Mineralogy, Oxford, England, UK., Private Communication (1967)

Radiation : CuKa
Lambda : 1.54180
SS/FOM : F30= 5(0.0670,89)

Filter : Beta
d-sp : Debye-Scherrer

2th	i	h	k	l
13.612	16	0	0	1
15.004	6	-1	1	1
19.322	16	0	2	1
21.035	10	-2	0	1
22.433	6	1	1	1
22.962	10	2	0	0
23.454	50	-1	3	0
24.572	20	-1	3	1
25.136	25	-2	2	1
25.727	60	-1	1	2
26.750	100	2	2	0
27.335	50	0	4	0
29.655	50	1	3	1
30.699	30	0	2	2
32.292	30	-1	3	2
34.743	50	-2	4	1
35.452	10	3	1	0
37.121	10	-1	5	1
37.604	6	-3	3	1
38.610	6	-1	1	3
39.673	2	-3	3	2
41.584	20	0	6	0
42.612	6	-4	0	2
43.473	6	-1	3	3
43.917	6	0	6	1
45.068	10	-4	2	2
45.692	6	2	2	2
50.674	30	-2	0	4
51.223	6	-4	4	1
54.759	6	-3	5	3
55.368	2	-1	7	2
56.103	2	3	5	1
57.756	2	-4	2	4
58.724	6	-5	3	1
60.198	6	-5	3	3
60.899	6	1	7	2
61.753	20	-2	8	0
62.823	2	-5	1	4
63.785	6	0	8	2
64.328	6	2	4	3
65.084	2	-2	0	5

Fig. A.2. Potassium barium aluminum silicate II, orthoclase-barium rich

Pattern : 00-038-0202 **Radiation =** 1.540600 **Quality :** Indexed

$Rb_2Al_2(SiO_3)_4$

Rubidium Aluminum Silicate

Lattice : Body-centered cubic **Mol. weight =** 529.23

S.G. : I (0) **Volume [CD] =** 2515.46

a = 13.60000 **Dx =** 0.349

General comments: High temperature form.
General comments: Pattern taken at 500 C.
Data collection flag: Non ambient temperature.

Kosorukov, A., Nadel, L., Russ. J. Inorg. Chem. (Engl. Transl.), volume 30, page 795 (1985)

Radiation : CoKa **Filter :** Not specified

Lambda : 1.79020 **d-sp :** Diffractometer

SS/FOM : F16= 17(0.0320,30)

2th	i	h	k	l
15.898	2	2	1	1
18.392	3	2	2	0
24.435	29	3	2	1
26.166	100	4	0	0
29.327	3	4	2	0
30.797	33	3	3	2
33.562	5	4	3	1
36.131	2	5	2	1
37.361	14	4	4	0
40.836	4	5	3	2
45.163	2	6	3	1
46.159	1	4	4	4
48.158	1	6	4	0
49.184	4	6	3	3
52.979	5	7	3	2
53.854	4	8	0	0

Fig. A.3. Rubidium aluminum silicate

Pattern : 00-038-1450 **Radiation =** 1.540600 **Quality :** High

$BaAl_2Si_2O_8$

Barium Aluminum Silicate
Celsian, syn

Lattice : Monoclinic
S.G. : C2/m (12)

a = 8.64110
b = 13.04700 **beta =** 115.07
c = 7.20310
a/b = 0.66231 **Z =** 4
c/b = 0.55209

Mol. weight = 375.46
Volume [CD] = 735.55
Dx = 3.390
Dm = 3.380

Sample preparation: The sample was prepared by Talmy, I., and Haught, D., of the Naval Surface Weapons Center, Silver Spring, Maryland, USA, by mixing stoichiometric quantities of Ba C2 O4, Si O2 gel and Al2 O3. Ten percent monoclinic Ba Al2 Si2 O8 was added as seed. The mixture was heated at 1250 C for 5 hours and at 1350 C for 5 hours.
Temperature of data collection: The mean temperature of data collection was 25.8 C.
Color: Colorless
Structure: Unit cell data was reported by Bruno et al. (1). Current work indicates all reflections are indexable on a cell with c-dimension, half of that given by Bruno (c=14.401, S.G.:=' I2/a').
Polymorphism: Other polymorphs reported are hexagonal (26-137) and monoclinic (10-352).
Optical data: A=1.5835, B=1.589, Q=1.594, Sign=+
Additional pattern: To replace 18-153 and 19-90.
Additional pattern: See ICSD 25836 (PDF 74-377).
Data collection flag: Ambient.

Wong-Ng, W., McMurdie, H., Paretzkin, B., Hubbard, C., Dragoo, A., NBS, Gaithersburg, MD, USA., ICDD Grant-in-Aid (1986)

CAS Number: 1302-50-7

Radiation : CuKa1
Lambda : 1.54060
SS/FOM : F30= 94(0.0070,46)

Filter : Monochromator crystal
d-sp : Diffractometer
Internal standard : Si FP

2th	i	h	k	l
13.563	64	0	2	0
15.097	24	-1	1	1
19.231	34	0	2	1
22.160	9	1	1	1
22.702	29	2	0	0
23.386	35	-1	3	0
24.536	28	-1	3	1
25.025	48	-2	2	1
25.645	74	-1	1	2
26.544	100	-2	2	0
27.160	51	-2	0	2
27.319	39	0	4	0
29.507	58	1	3	1
30.626	30	0	4	1
32.243	41	-1	3	2
34.168	25	2	2	1
34.370	43	-3	1	2
34.665	64	-2	4	1
35.049	14	-3	1	0
35.824	3	-2	4	0
37.050	11	-1	5	1
37.439	6	-3	3	1
38.563	19	-1	1	3
39.665	13	-3	3	2
39.902	10	1	3	2
40.314	10	-3	3	0
40.645	14	1	5	1
41.499	23	0	6	0
41.936	13	2	4	1
42.179	9	-4	0	1
42.581	11	-4	0	2
42.748	16	-1	5	2
42.984	18	3	1	1
43.460	9	-1	3	3
43.853	11	0	6	1
44.526	8	-4	2	1
44.926	16	-4	2	2
45.226	9	2	2	2
46.392	16	4	0	0
46.938	7	-3	5	1
47.492	10	-4	0	3
48.434	7	1	1	3
48.857	9	-3	5	2
49.059	8	1	5	2
49.358	4	-3	5	0
50.382	20	0	4	3
50.655	20	-2	0	4
50.986	11	-4	4	1
52.070	1	-1	5	3
52.690	3	-2	2	4
53.512	3	-5	1	2
53.911	4	3	1	2
54.702	7	-3	5	3
55.464	5	-1	7	2
55.654	12	3	5	1
56.384	8	0	8	0
56.397	8	2	0	3
57.921	10	-4	2	4
58.274	13	0	8	1
58.494	6	-2	4	4
59.417	1	-5	1	0
60.138	11	0	6	3
60.667	9	-4	6	1
60.818	12	-2	8	1
61.552	11	-2	8	0
62.830	7	-5	1	4
63.046	6	-5	3	0

Fig. A.4. Barium aluminum silicate, celsian

Pattern : 00-038-1453 **Radiation =** 1.540600 **Quality :** High

$Ba_{0.25}Sr_{0.75}Al_2Si_2O_8$

Barium Strontium Aluminum Silicate

Lattice : Monoclinic
S.G. : C2/m (12)

a = 8.45020
b = 12.99210
c = 7.15140
a/b = 0.65041
c/b = 0.55044

beta = 115.23
Z = 4

Mol. weight = 338.18
Volume [CD] = 710.22
Dx = 3.163

Sample preparation: The sample was prepared by I. Talmy and D. Haught of the Naval Surface Weapons Center, Silver Spring, Maryland, USA, by mixing stoichiometric quantities of Ba C2 O4, Sr C2 O4, fused-Si O2, and Al2 O3. The mixture was heated at 1350 C for 2 hours. The Sr C2 O4 and Ba C2 O4 were coprecipitated from the mixture of Sr (N O3)2 and Ba (N O3)2 with (N H4)2 C2 O4.
Color: Colorless
Temperature of data collection: The mean temperature of data collection was 25.8 C.
Structure: The initial cell parameters were obtained based on those of the end-members Sr Al2 Si2 O8 and Ba Al2 Si2 O8.
Data collection flag: Ambient.

Wong-Ng, W., McMurdie, H., Paretzkin, B., Hubbard, C., Dragoo, A., NBS (USA)., ICDD Grant-in-Aid (1986)

Radiation : CuKa1
Lambda : 1.54060
SS/FOM : F30= 94(0.0063,51)

Filter : Monochromator crystal
d-sp : Diffractometer
Internal standard : Si FP

2th	i	h	k	l
13.619	41	0	2	0
15.253	16	-1	1	1
19.339	26	0	2	1
21.353	6	-2	0	1
23.260	23	2	0	0
23.591	44	-1	3	0
24.702	25	-1	3	1
25.415	31	-2	2	1
25.825	70	-1	1	2
27.048	100	-2	2	0
27.545	79	0	0	2
29.827	48	1	3	1
30.781	29	0	4	1
32.445	39	-1	3	2
34.760	24	2	2	1
35.033	67	-2	4	1
35.875	7	-3	1	0
36.505	1	-1	5	0
37.249	10	-1	5	1
38.095	11	-3	3	1
38.849	9	-1	1	3
40.241	11	-3	3	2
40.706	9	-2	2	3
40.965	13	1	5	1
41.684	17	0	6	0
42.536	8	2	4	1
42.985	7	-1	5	2
43.258	7	-4	0	1
43.738	9	-1	3	3
43.919	14	3	1	1
44.062	15	0	6	1
45.540	8	-4	2	1
45.801	12	-4	2	2
45.942	13	2	2	2
46.918	5	-3	3	3
47.304	8	-2	6	1
47.559	12	4	0	0
48.381	10	3	3	1
49.005	6	1	1	3
49.399	8	-3	5	2
49.495	8	1	5	2
50.116	1	-3	5	0
50.646	8	-2	6	2
50.813	13	0	4	3
51.060	18	-2	0	4
51.962	7	-4	4	1
52.408	1	-1	5	3
53.089	1	-2	2	4
54.821	3	-5	1	2
54.971	4	3	1	2
55.216	6	-3	5	3
55.762	3	-1	7	2
56.503	5	3	5	1
56.635	9	0	8	0
56.903	5	0	0	4
57.524	1	-5	1	3
58.660	9	-5	3	2
58.776	11	0	2	4
58.916	10	-2	4	4
59.146	3	2	2	3
60.544	2	0	6	3
61.270	10	-5	3	3
61.588	6	-4	6	1
62.046	11	-2	8	0
63.847	4	-5	1	4

Fig. A.5. Barium (0.25) strontium (0.75) aluminum silicate

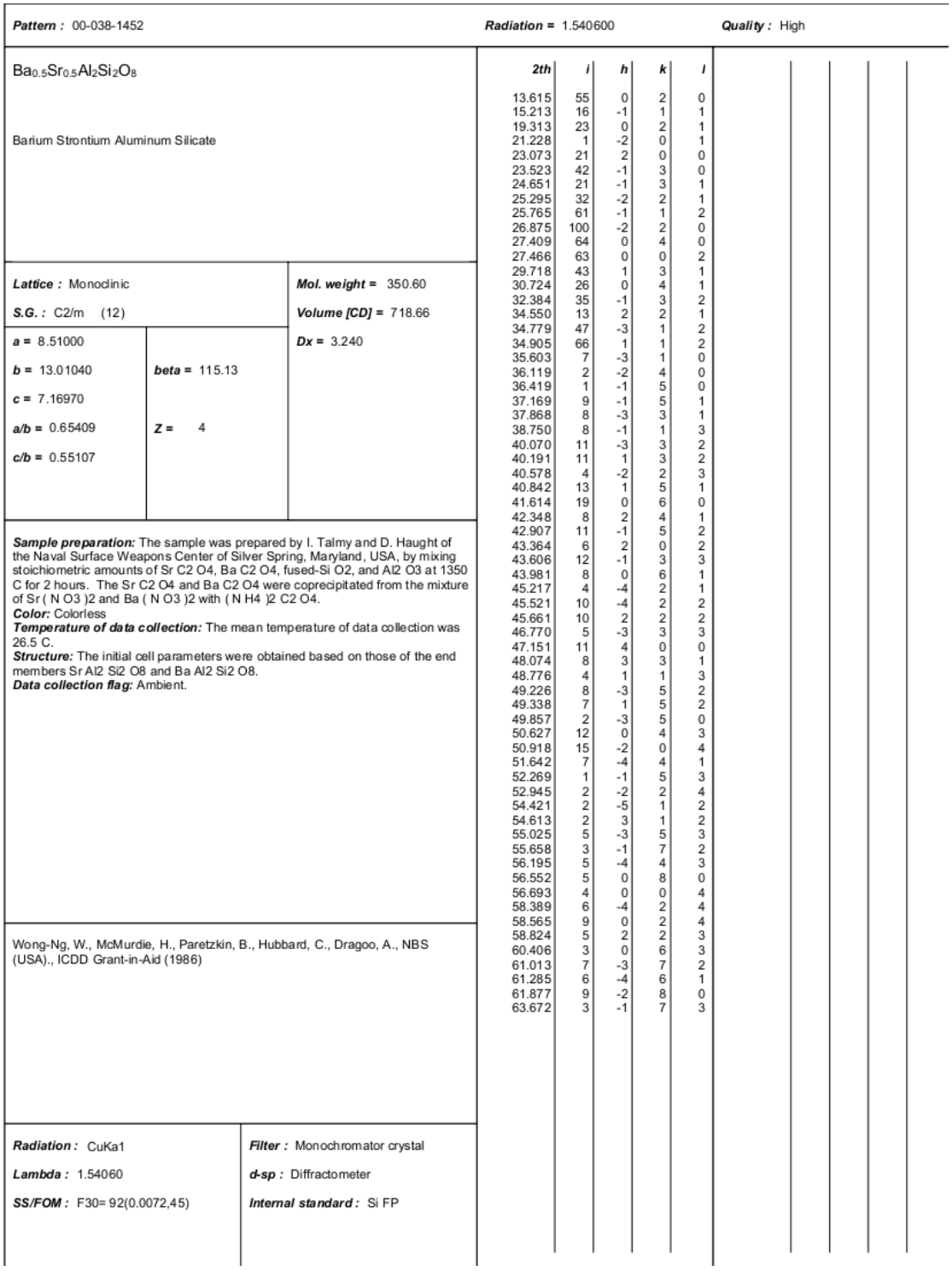

Pattern : 00-038-1452 **Radiation =** 1.540600 **Quality :** High

$Ba_{0.5}Sr_{0.5}Al_2Si_2O_8$

Barium Strontium Aluminum Silicate

Lattice : Monoclinic
S.G. : C2/m (12)

a = 8.51000
b = 13.01040
c = 7.16970
a/b = 0.65409
c/b = 0.55107

beta = 115.13
Z = 4

Mol. weight = 350.60
Volume [CD] = 718.66
Dx = 3.240

Sample preparation: The sample was prepared by I. Talmy and D. Haught of the Naval Surface Weapons Center of Silver Spring, Maryland, USA, by mixing stoichiometric amounts of Sr C2 O4, Ba C2 O4, fused-Si O2, and Al2 O3 at 1350 C for 2 hours. The Sr C2 O4 and Ba C2 O4 were coprecipitated from the mixture of Sr (N O3)2 and Ba (N O3)2 with (N H4)2 C2 O4.
Color: Colorless
Temperature of data collection: The mean temperature of data collection was 26.5 C.
Structure: The initial cell parameters were obtained based on those of the end members Sr Al2 Si2 O8 and Ba Al2 Si2 O8.
Data collection flag: Ambient.

Wong-Ng, W., McMurdie, H., Paretzkin, B., Hubbard, C., Dragoo, A., NBS (USA)., ICDD Grant-in-Aid (1986)

Radiation : CuKa1
Lambda : 1.54060
SS/FOM : F30= 92(0.0072,45)

Filter : Monochromator crystal
d-sp : Diffractometer
Internal standard : Si FP

2th	i	h	k	l
13.615	55	0	2	0
15.213	16	-1	1	1
19.313	23	0	2	1
21.228	1	-2	0	1
23.073	21	2	0	0
23.523	42	-1	3	0
24.651	21	-1	3	1
25.295	32	-2	2	1
25.765	61	-1	1	2
26.875	100	-2	2	0
27.409	64	0	4	0
27.466	63	0	0	2
29.718	43	1	3	1
30.724	26	0	4	1
32.384	35	-1	3	2
34.550	13	2	2	1
34.779	47	-3	1	2
34.905	66	1	1	2
35.603	7	-3	1	0
36.119	2	-2	4	0
36.419	1	-1	5	0
37.169	9	-1	5	1
37.868	8	-3	3	1
38.750	8	-1	1	3
40.070	11	-3	3	2
40.191	11	1	3	2
40.578	4	-2	2	3
40.842	13	1	5	1
41.614	19	0	6	0
42.348	8	2	4	1
42.907	11	-1	5	2
43.364	6	2	0	2
43.606	12	-1	3	3
43.981	8	0	6	1
45.217	4	-4	2	1
45.521	10	-4	2	2
45.661	10	2	2	2
46.770	5	-3	3	3
47.151	11	4	0	0
48.074	8	3	3	1
48.776	4	1	1	3
49.226	8	-3	5	2
49.338	7	1	5	2
49.857	2	-3	5	0
50.627	12	0	4	3
50.918	15	-2	0	4
51.642	7	-4	4	1
52.269	1	-1	5	3
52.945	2	-2	2	4
54.421	2	-5	1	2
54.613	2	3	1	2
55.025	5	-3	5	3
55.658	3	-1	7	2
56.195	5	-4	4	3
56.552	5	0	8	0
56.693	4	0	0	4
58.389	6	-4	2	4
58.565	9	0	2	4
58.824	5	2	2	3
60.406	3	0	6	3
61.013	7	-3	7	2
61.285	6	-4	6	1
61.877	9	-2	8	0
63.672	3	-1	7	3

Fig. A.6. Barium (0.50) strontium (0.50) aluminum silicate

Pattern : 00-038-1451 **Radiation =** 1.540600 **Quality :** High

$Ba_{0.75}Sr_{0.25}Al_2Si_2O_8$

Barium Strontium Aluminum Silicate

Lattice : Monoclinic
S.G. : C2/m (12)

a = 8.58020
b = 13.03140
c = 7.18920
a/b = 0.65843
c/b = 0.55168

beta = 115.15
Z = 4

Mol. weight = 363.03
Volume [CD] = 727.62
Dx = 3.314

Sample preparation: The sample was prepared by Talmy, I., Haught, D., Naval Surface Weapons Center, Silver Spring, Maryland, USA, by mixing stoichiometric amounts of Ba C2 O4, Sr C2 O4, fused-Si O2, and Al2 O3 at 1500 C for 2 hours. The Sr C2 O4 and Ba C2 O4 were coprecipitated from the mixture of Sr (N O3)2 and Ba (N O3)2 with (N H4)2 C2 O4.
Color: Colorless
Temperature of data collection: The mean temperature of data collection was 25.0 C.
Structure: Initial cell parameters of the solid solution were deduced based on those of the end-members Sr Al2 Si2 O8 and Ba Al2 Si2 O8.
Data collection flag: Ambient.

Wong-Ng, W., McMurdie, H., Paretzkin, B., Hubbard, C., Dragoo, A., NBS (USA)., ICDD Grant-in-Aid (1986)

Radiation : CuKa1
Lambda : 1.54060
SS/FOM : F30= 88(0.0076,45)

Filter : Monochromator crystal
d-sp : Diffractometer
Internal standard : Si FP

2th	i	h	k	l
13.582	57	0	2	0
15.155	21	-1	1	1
19.262	30	0	2	1
22.281	6	1	1	1
22.879	23	2	0	0
23.454	40	-1	3	0
24.585	21	-1	3	1
25.148	40	-2	2	1
25.700	62	-1	1	2
26.700	100	-2	2	0
27.253	44	-2	0	2
27.360	49	0	4	0
29.599	67	1	3	1
30.662	30	0	4	1
32.290	45	-1	3	2
34.386	17	2	2	1
34.552	47	-3	1	2
34.747	64	-2	4	1
35.322	11	-3	1	0
35.960	4	-2	4	0
36.348	2	-1	5	0
37.101	14	-1	5	1
37.622	10	-3	3	1
38.646	12	-1	1	3
39.842	11	-3	3	2
40.060	13	1	3	2
40.517	9	-3	3	0
40.746	14	1	5	1
41.538	22	0	6	0
42.149	12	2	4	1
42.521	9	-4	0	1
42.830	11	-1	5	2
43.280	14	3	1	1
43.522	9	-1	3	3
43.918	10	0	6	1
44.857	8	-4	2	1
45.181	14	-4	2	2
45.448	11	2	2	2
46.595	11	-3	3	3
46.733	13	4	0	0
47.012	5	-2	6	1
47.764	10	3	3	1
48.605	6	1	1	3
49.031	8	-3	5	2
49.180	9	1	5	2
49.596	4	-3	5	0
50.394	16	-2	6	2
50.500	18	0	4	3
50.763	20	-2	0	4
51.306	8	-4	4	1
52.153	1	-1	5	3
52.802	3	-2	2	4
53.944	2	-5	1	2
54.266	3	3	1	2
54.863	7	-3	5	3
55.549	5	-1	7	2
55.908	8	-4	4	3
56.440	7	0	8	0
56.588	4	-3	3	4
58.112	8	-4	2	4
58.420	11	0	2	4
58.595	8	-2	4	4
59.917	3	-5	1	0
60.242	5	0	6	3
60.501	9	-5	3	3
60.939	10	1	7	2
61.698	12	-2	8	0
63.100	5	-5	1	4
63.580	7	1	1	4

Fig. A.7. Barium (0.75) strontium (0.25) aluminum silicate

Pattern : 00-041-0569 **Radiation =** 1.540600 **Quality :** Calculated

$Cs_4Al_4Si_{20}O_{48}$

Cesium Aluminum Silicate
Also called: Aluminosilicate, (Cs)

Lattice : Base-centered orthorhombic
S.G. : Ama2 (40)

a = 16.77600
b = 13.82800
c = 5.02100
a/b = 1.21319
c/b = 0.36310

Mol. weight = 1969.23
Volume [CD] = 1164.76
Dx = 2.807

Data collection flag: Ambient.

von Ballmoos, R., Higgins, J., Collection of Simulated XRD Powder Patterns For Zeolites, volume 10, page 366S (1990)

Radiation : CuKa
Lambda : 1.54180
SS/FOM : F30=336(0.0029,31)

Filter : Not specified
d-sp : Calculated spacings

2th	i	h	k	l	2th	i	h	k	l
10.542	1	2	0	0	56.392	1	10	2	0
12.790	2	0	2	0	56.612	3	3	6	2
16.607	1	2	2	0	57.091	1	5	7	1
18.785	2	0	1	1	57.191	1	8	0	2
19.525	4	1	1	1	57.851	8	3	1	3
20.414	1	3	2	0	58.140	3	8	5	1
21.163	1	4	0	0	58.330	5	10	1	1
21.593	50	2	1	1	58.869	3	8	2	2
24.661	100	3	1	1	58.919	1	1	3	3
24.810	52	4	2	0	59.559	1	8	6	0
25.750	21	0	4	0	59.759	3	2	3	3
26.229	18	0	3	1					
26.299	23	1	4	0					
26.769	39	1	3	1					
27.898	5	2	4	0					
28.337	7	2	3	1					
28.447	3	4	1	1					
29.566	10	5	2	0					
30.376	8	3	4	0					
30.785	14	3	3	1					
31.984	5	6	0	0					
32.724	19	5	1	1					
33.573	4	4	4	0					
33.943	7	4	3	1					
34.582	5	6	2	0					
35.741	10	0	0	2					
37.080	9	0	5	1					
37.320	6	5	4	0					
37.350	7	6	1	1					
*37.360	4	2	0	2					
37.480	4	1	5	1					
37.660	4	5	3	1					
38.109	13	0	2	2					
38.499	3	1	2	2					
38.659	7	2	5	1					
39.058	1	0	6	0					
39.438	1	1	6	0					
39.648	2	2	2	2					
39.778	1	7	2	0					
40.557	2	3	5	1					
41.506	5	3	2	2					
*41.506	5	6	4	0					
41.816	7	6	3	1					
41.906	6	4	0	2					
42.265	3	7	1	1					
42.385	7	3	6	0					
43.095	1	4	5	1					
*43.105	9	8	0	0					
43.994	2	4	2	2					
44.573	1	0	4	2					
44.843	5	4	6	0					
44.913	2	1	4	2					
45.932	5	2	4	2					
46.052	1	7	4	0					
46.182	2	5	5	1					
46.332	2	7	3	1					
47.041	4	5	2	2					
47.401	1	8	1	1					
47.591	6	3	4	2					
47.850	5	5	6	0					
48.710	6	6	0	2					
49.549	8	0	7	1					
49.768	2	6	5	1					
49.839	7	4	4	2					
49.869	1	1	7	1					
50.578	3	6	2	2					
50.808	1	2	7	1					
51.157	5	8	3	1					
52.346	3	3	7	1					
52.626	2	5	4	2					
52.766	3	9	1	1					
53.765	4	7	5	1					
53.965	1	0	6	2					
54.134	3	2	8	0					
54.264	1	1	6	2					
54.454	2	4	7	1					
54.534	2	7	2	2					
55.903	1	6	4	2					
56.003	1	9	4	0					
56.252	2	9	3	1					

Fig. A.8. Cesium aluminum silicate, silicon rich

Pattern : 01-088-1048 **Radiation =** 1.540600 **Quality :** Calculated

$Ba(Al_2Si_2O_8)$

Barium Aluminum Silicate

Lattice : Hexagonal
S.G. : P-3 (147)

a = 5.29645
c = 7.78874

Z = 1

Mol. weight = 375.46
Volume [CD] = 189.22
Dx = 3.295
I/Icor = 2.74

ICSD collection code: 085363
Temperature factor: ATF
Remarks from ICSD/CSD: REM TEM 298.
Remarks from ICSD/CSD: REM RVP.
Remarks from ICSD/CSD: REM K Sample prepared by conversion of the fully Ba-exchange
Remarks from ICSD/CSD: REM zeolite LTA..
Data collection flag: Ambient.

Kremenovic, A., Norby, P., Dimitrijevic, R., Dondur, V., Solid State Ionics, volume 101, page 611 (1997)
Calculated from ICSD using POWD-12++

Radiation : CuKa1
Lambda : 1.54060
SS/FOM : F30=1000(0.0001,30)

Filter : Not specified
d-sp : Calculated spacings

2th	i	h	k	l
11.352	376	0	0	1
19.336	17	1	0	0
22.477	999	1	0	1
22.816	24	0	0	2
30.078	654	0	1	2
33.821	343	1	1	0
34.519	26	0	0	3
35.784	45	1	1	-1
39.251	66	2	0	0
39.867	116	0	1	3
40.991	196	2	0	1
41.190	65	1	1	-2
45.883	36	0	2	2
46.607	46	0	0	4
49.101	129	1	1	-3
50.905	18	1	0	4
52.759	2	2	1	0
53.250	6	0	2	3
54.154	88	1	2	1
58.203	91	2	1	-2
58.816	66	1	1	-4
59.273	3	0	0	5
60.505	40	3	0	0
61.784	5	3	0	1
62.523	15	0	2	4
62.964	39	1	0	5
64.589	25	1	2	-3
65.537	2	3	0	2
70.018	1	1	1	-5
71.147	27	2	2	0
71.561	19	0	3	3
72.328	3	2	2	-1
72.797	3	0	0	6
73.012	9	2	1	-4
73.422	35	0	2	5
74.530	1	1	3	0
75.690	18	1	3	-1
76.151	10	0	1	6
79.136	22	3	1	-2
79.667	15	0	3	4
81.542	6	2	2	-3
82.729	7	1	1	-6
83.333	19	2	1	-5
84.403	1	4	0	0
84.798	7	3	1	-3
85.529	6	0	4	1
85.978	6	2	0	6
87.624	2	0	0	7
88.896	3	4	0	2
89.418	10	2	2	-4

Fig. A.9. Barium aluminum silicate

Pattern : 00-047-0471 **Radiation =** 1.540600 **Quality :** High

$CsAlSiO_4$

Cesium Aluminum Silicate
Also called: Pollucite

Lattice : Body-centered cubic
S.G. : Ia-3d (230)

a = 13.64710
Z = 24

Mol. weight = 251.97
Volume [CD] = 2541.68
Dx = 3.951

Sample preparation: Recrystallized from Cs-LTA precursor at 1350 C for 3 hours.
General comments: High-temperature phase.
Unit cell: Reference reports: a=13.6595(4).
General comments: Cell parameter generated by least squares refinement.
Data collection flag: Ambient.

Dimitrijevic, R., Dondur, V., Petranovic, N., J. Solid State Chem., volume 95, page 335 (1991)

Radiation : CuKa
Lambda : 1.54180
SS/FOM : F30= 32(0.0250,37)

Filter : Monochromator crystal
d-sp : Diffractometer
Internal standard : Si

2th	i	h	k	l
15.915	6	2	1	1
18.395	2	2	2	0
24.415	44	3	2	1
26.130	100	4	0	0
29.290	4	4	2	0
30.729	44	3	3	2
32.136	1	4	2	2
33.455	4	4	3	1
36.025	6	5	2	1
37.265	22	4	4	0
40.715	12	6	1	1
41.834	1	6	2	0
45.054	6	6	3	1
46.016	5	4	4	4
48.061	1	6	4	0
49.037	10	6	3	3
49.976	1	6	4	2
52.758	12	6	5	1
53.656	3	8	0	0
54.600	1	7	4	1
55.554	1	8	2	0
56.336	1	6	5	3
58.135	1	8	3	1
59.833	3	7	5	2
60.634	3	8	4	0
63.084	2	9	2	1
64.759	1	8	5	1
66.319	2	9	3	2
67.138	1	8	4	4
69.460	3	10	1	1

Fig. A.10. Cesium aluminum silicate, pollucite

Pattern : 01-088-2487 **Radiation =** 1.540600 **Quality :** Calculated

SiO_2

Silicon Oxide
Quartz low

Lattice : Hexagonal
S.G. : P3221 (154)

a = 4.93000
c = 5.38500

Z = 3

Mol. weight = 60.08
Volume [CD] = 113.35
Dx = 2.641
I/Icor = 3.00

ICSD collection code: 041672
ICSD space group comment: ICSD SG: P3221S IT is: 154 SG short form: P3221
Remarks from ICSD/CSD: REM THE.
Remarks from ICSD/CSD: REM M PDF 46-1045.
Remarks from ICSD/CSD: REM M Calculated with pseudo-potential total-energy method.
Remarks from ICSD/CSD: REM M Experimental cell: 4.916, 5.4054.
Test from ICSD: No R value given.
Test from ICSD: At least one TF missing.
Remarks from ICSD/CSD: REM PRE Mentioned.
Data collection flag: Non ambient pressure.

Tse, J.S., Klug, D.D., Allan, D.C., Phys. Rev. B: Condens. Matter, volume 51, page 16392 (1995)
Calculated from ICSD using POWD-12++

Radiation : CuKa1
Lambda : 1.54060
SS/FOM : F28=1000(0.0001,29)

Filter : Not specified
d-sp : Calculated spacings

2th	i	h	k	l
20.788	212	1	0	0
26.623	999	0	1	1
36.419	74	1	1	0
39.538	72	1	0	2
40.202	31	1	1	-1
42.303	49	2	0	0
45.680	27	2	0	1
50.134	104	1	1	-2
50.826	4	0	0	3
54.838	33	0	2	2
55.488	14	0	1	3
57.024	2	1	2	0
59.777	77	2	1	-1
64.127	14	1	1	-3
65.538	3	3	0	0
67.630	44	1	2	2
68.089	40	0	3	1
68.206	57	2	0	3
73.733	17	1	0	4
75.500	21	3	0	2
77.363	10	2	2	0
79.865	22	1	2	-3
81.160	21	1	3	0
81.379	25	1	1	-4
83.526	11	3	1	-1
85.135	2	2	0	4
86.842	1	2	2	-2
87.377	2	3	0	3

Fig. A.11. Quartz

APPENDIX B

QUANTITATIVE WDS DETECTION LIMITS & BASIS OXIDES

Table B.1

Quantitative WDS detection limits. Analysis is limited to specific selected locations in 1200°C sintered bentonite, assumed basic oxides.

	Na	Rb	Mg	Al	Si	Ca	Sr	Fe	Cs	Ba
Detection limits										
Dark 1	0.0125	0.0203	0.0084	0.0089	0.0248	0.015	0.0874	0.0394	0.1318	0.1378
Dark 2	0.0123	0.0203	0.0084	0.0089	0.0207	0.015	0.0846	0.0393	0.1282	0.1477
Dark 3	0.0123	0.0204	0.0084	0.0089	0.0257	0.0146	0.0867	0.04	0.129	0.1359
Bright 1	0.0132	0.023	0.0098	0.0108	0.0272	0.0156	0.0894	0.0421	0.2113	0.1325
Bright 2	0.013	0.0226	0.0098	0.0106	0.0276	0.0154	0	0.0415	0.1936	0.1293
Bright 3	0.0137	0.0225	0.0099	0.0107	0.0291	0.0152	0.0843	0.0418	0.1999	0.125
Grey 1	0.0125	0.021	0.0087	0.0104	0.0247	0.0147	0.0829	0.0406	0.1311	0.1518
Grey 2	0.0126	0.0204	0.0088	0.0105	0.0246	0.0145	0.0813	0.0424	0.12	0.1499
Grey 3	0.0124	0.0202	0.0087	0.0105	0.0228	0.0142	0.0862	0.0413	0.1216	0.1439
Basis Oxides	Na_2O	Rb_2O	MgO	Al_2O_3	SiO_2	CaO	SrO	FeO	Cs_2O	BaO

APPENDIX C
STOICHIOMETRY CALCULATIONS

	STOICHIOMETRY														
MASS															
AVERAGES-- across all sinterings		70% loaded			100% loaded										
	Cesium	10.9605			Cesium	13.703		pollucite	CsAlSiO4	feldspar	Ba or Sr Al2Si2O8				
	Strontium	3.49362			Strontium	4.373		for each mole Cs or Rb 1 mole Al and 1 mole Si							
	Barium	8.93453			Barium	11.658		for each mole Sr or Ba 2 moles Al and 2 moles Si							
	Rubidium	1.54017			Rubidium	2.056									
waste mass %	total	24.9288			total	31.7913									
clay mass %	left=clay	75.0712			left=clay	68.209									
							moles we need to make feldspars/pollucite								
1000 gram basis			70% laoded		100% loaded		70%		100%						
	grams	MW	moles		moles		Al2O3	SiO2	Al2O3	SiO2					
Cs	137.03	132.906	0.82468		1.0310333		0.41234004	0.82468	0.51552	1.031033328					
Sr	43.73	87.62	0.39872		0.499087		0.3987245	0.79745	0.49909	0.998173933					
Ba	116.58	137.327	0.6506		0.8489226		0.65060282	1.30121	0.84892	1.697845289					
Rb	20.56	85.4678	0.1802		0.2405584		0.09010249	0.1802	0.12028	0.240558433					
						total	1.55176985	3.10354	1.98381	3.967610983					
Bentonite Composition		%	MW	70% loading leaves 75.07g of clay	moles 70%	100% loading 68.09g of clay	moles 100%		at our 70% and 100% loading we are lacking alumina						
	SiO2	0.6956	60.0843	750.7	8.6909046	680.9	7.8828253		this is not counting losses to Mg, Ca, Na, K etc.						
	Al2O3	0.2069	101.961		1.5233214		1.38168315								
	MgO	0.027	40.3044		0.5028955		0.4561363		excess silica in all			100% loaded		70%	
	Fe2O3	0.0485	159.69		0.2279977		0.20679848			%		0.30352		0.01833	
	CaO	0.013	56.077		0.1740304		0.15784903			moles lack		0.60212		0.02845	
	Na2O	0.0243	61.9789		0.2943261		0.26695972								
	K2O	0.003	94.2		0.0239076		0.02168471								

Fig. C.1. Stoichiometry calculations, alumina deficiencies

APPENDIX D

NEUTRON ACTIVATION DETAILS

Table D.1

NAA strontium concentration in 100% & 70% loaded bentonite. Irradiated at 10 X 10^{13} neutrons/s·cm^2 for 60 sec, counted for 300 sec.

Specific Activity of Sr-87					
Sintering Temp. °C	mass (g)	Wt. Mean	Standard Dev.	Strontium mass %	Std. Dev.
100% Theoretical Loading					
700	0.1002	2.72E+01	1.55E+00	4.115	3.28E-01
800	0.1001	2.95E+01	1.68E+00	4.466	3.56E-01
1000	0.1004	3.00E+01	1.70E+00	4.539	3.62E-01
70% Theoretical Loading					
700	0.1000	2.31E+01	1.31E+00	3.497	2.79E-01
800	0.1002	2.29E+01	1.30E+00	3.464	2.76E-01
1000	0.1002	2.32E+01	1.32E+00	3.520	2.81E-01

Table D.2

NAA Cesium concentration in 100% & 70% loaded bentonite. Irradiated at 10 X 10^{13} neutrons/s·cm^2 for 3600 sec, counted for 1200 sec.

		Specific Activity of Cs-134			
Sintering Temp. °C	mass (g)	Wt. Mean	Standard Dev.	Cesium mass %	Std. Dev.
		100% Theoretical Loading			
700	0.5	1.78E+01	2.08E-01	13.915	2.2E-01
800	0.5003	1.76E+01	2.06E+00	13.774	2.2E-01
1000	0.5003	1.72E+01	1.99E+00	13.422	2.1E-01
		70% Theoretical Loading			
700	0.5004	1.40E+01	1.82E-01	10.933	1.9E-01
800	0.5003	1.40E+01	1.68E+00	10.933	1.8E-01
1000	0.5003	1.39E+01	1.68E+00	10.847	1.8E-01

Table D.3

NAA rubidium concentration in 100% & 70% loaded bentonite. Irradiated at 10 X 10^{13} neutrons/s·cm^2 for 3600 sec, counted for 1200 sec.

		Specific Activity of Rb-86			
Sintering Temp. °C	mass (g)	Wt. Mean	Standard Dev.	Rubidium mass %	Std. Dev.
		100% Theoretical Loading			
700	0.5	2.16E-01	1.43E-02	2.001	1.3E-01
800	0.5003	2.43E-01	1.45E-02	2.251	1.4E-01
1000	0.5003	2.07E-01	1.50E-02	1.918	1.4E-01
		70% Theoretical Loading			
700	0.5004	1.89E-01	1.60E-02	1.751	1.5E-01
800	0.5003	1.50E-01	1.38E-02	1.387	1.3E-01
1000	0.5003	1.60E-01	1.66E-02	1.482	1.5E-01

Table D.4

NAA barium concentration in 100% & 70% loaded bentonite. Irradiated at 10 X 10^{13} neutrons/s·cm^2 for 3600 sec, counted for 1200 sec.

		Specific Activity of Ba-131			
Sintering Temp. °C	mass (g)	Wt. Mean	Standard Dev.	Barium mass %	Std. Dev.
		100% Theoretical Loading			
700	0.5	1.52E-01	1.07E-02	12.155	8.7E-01
800	0.5003	1.46E-01	1.79E-02	11.675	1.4E+01
1000	0.5003	1.40E-01	1.51E-02	11.195	1.2E+01
		70% Theoretical Loading			
700	0.5004	1.12E-01	1.65E-02	8.980	1.3E+00
800	0.5003	1.00E-01	1.50E-02	7.996	1.2E+00
1000	0.5003	1.23E-01	1.39E-02	9.828	1.1E+00

VITA

Luis Humberto Ortega

Contact Information:

Dept. of Nuclear Engineering c/o Dr. Sean M. McDeavitt

Texas A&M University

College Station, TX 77843-3133

Education:

Texas A&M University College Station, Texas

Ph.D., Materials Science & Engineering, December 2009

Purdue University West Lafayette, Indiana

M.S., Nuclear Engineering, December 2006

New Mexico State University Las Cruces, New Mexico

B.S., Chemical Engineering, May 2000